Where were the mountains and how big were they?

Andrew S. Merdith^{1,*}, Nicky M. Wright², Simon Williams³, Stephen J. Hunter⁴, Jonathon Leonard², Morgan L. Blades¹, Fred Bowyer⁴, Krisana⁴, Khushboo Gurung⁴, Zhen Xu⁴, Derrick Hasterok¹, Alan Collins¹, Benjamin J.W. Mills⁴

¹School of Physics, Chemistry and Earth Science, Adelaide University, Australia

Peer review status:

This is a non-peer-reviewed preprint submitted to EarthArXiv $\,$

²School of Geosciences, University of Sydney, Sydney, Australia

³IMAS, University of Tasmania, Hobart, Australia

⁴School of Earth and Environment, University of Leeds, UK

^{*}Corresponding author (Andrew.merdith@adelaide.edu.au)

Where were the mountains and how big were they?

Andrew S. Merdith¹, Nicky M. Wright², Simon Williams³, Stephen J. Hunter⁴, Jonathon Leonard², Morgan L. Blades¹, Fred Bowyer⁴, Krisana⁴, Khushboo Gurung⁴, Zhen Xu⁴, Derrick Hasterok¹, Alan Collins¹, Benjamin J.W. Mills⁴

Abstract

Constraining past topography and the shape of Earth's surface is the next frontier in palaeogeography and full-plate tectonic modelling. Mountains are highly dynamic on geological time scales, growing in response to tectonic processes such as subduction and continent collision, and eroding as they are exposed to precipitation and time. Mountain ranges regulate atmospheric circulation and enforce a first order control on dissolved river loads and the transport of sediments to sedimentary basins. Because of this, mountains and the changing elevation of Earth's surface are essential to understanding how the wider Earth system has evolved through time. Here we present a computational full-Earth, forward model of palaeotopography and palaeobathymetry from 1 Ga to present-day. We use an existing fullplate tectonic model, which traces the evolution of tectonic plate boundaries, to automatically isolate specific tectonic environments that are associated with mountain building, such as continental arcs, continental collisions, rifts and large igneous provinces. Our model separates Earth's continental surface into a set of equally spaced nodes, so that each node can record its own unique topographic evolution, independent of the nodes around it. Once these regions have been identified, we simulate their growth, and decay, over the last 1 Ga, using parameters and limits derived from the present-day expression of topography on Earth. Our model produces a set of maps at 1° resolution and every Ma from 970 to 0 Ma. Despite the differences between our work and other existing Phanerozoic palaeotopographic models, our predicted Earth surface has a similar hypsometry to what we observe at present-day. Our model can provide a quantitative basis for palaeoclimate or landscape evolution modelling over the last 1 Ga.

1. Introduction

Change in Earth's surface through geologic time is fundamental to understanding drivers in planetary change and the interaction between Earth's spheres (Walker et al., 1981). Palaeogeography, as the physical expression of land and water over the Earth's surface in Earth's past, encompasses both the spatial configuration of continents and oceans, and the distributions of physical surface features on land, and sea (Markwick and Valdes, 2004; Torsvik and Cocks, 2016; Scotese, 2021).

¹School of Physics, Chemistry and Earth Science, Adelaide University, Australia

²School of Geosciences, University of Sydney, Sydney, Australia

³IMAS, University of Tasmania, Hobart, Australia

⁴School of Earth and Environment, University of Leeds, UK

To a first order, the configuration of Earth's surface is dependent on plate tectonics—the slow motion of Earth's lithosphere over long ($>10^6$ a) timescales. However, more precise expressions are dependent on a myriad of both regional and global variables spanning a range of both spatial and temporal scales. Orogenesis, which regulates atmospheric circulation, precipitation and creates environmental niches (see recent overview in Fluteau et al., 2023), is driven by the balance between uplift and erosion (England and Molnar, 1990). Erosion, driven by relief and runoff (Willett, 1999), leads to the formation of sedimentary basins, river deltas and coastal environments. Ocean basins, which exert a first order influence on sea level, ocean circulation and atmospheric temperature are determined by the palaeogeographic distribution of continental crust and age of oceanic crust (Rahmstorf, 2002; Sijp et al., 2014). The geological record preserves many traces of these ancient environments that can be, and have been, used to reconstruct palaeogeography (Blakey, 2008; Vérard et al., 2015; Torsvik and Cocks, 2016; Cao et al., 2017; Merdith et al., 2017, 2021; Scotese, 2021). In turn, these reconstructed palaeogeographic maps can be further used to model past climate (Goddéris et al., 2014; Valdes et al., 2021) or landscape evolution (Barnhart et al., 2020; Salles et al., 2020) to understand how and why Earth's surface has changed through time.

There are, however, some key limitations with inverting the geological record to reconstruct past environments and elevations. The most significant of which is that the further back in time one travels, the fewer rocks are preserved (e.g. Domeier and Torsvik, 2017; Vérard, 2019b). This is problematic for many reasons, principally, because as fewer (or no) rocks are available, it becomes increasingly difficult to ground truth or test hypotheses, making it hard to properly untangle the scale and impact of significant events in Earth history. These issues are exacerbated further because many key questions and phenomena are thought to be global, not regional, in scale. For example, understanding the oxygenation of Earth's oceans in the Mesoproterozoic currently relies on rocks predominantly collected from North China and Australia (Planavsky et al., 2011). Similarly, the distribution of landmasses around the Snowball Earth events are dependent on high quality palaeomagnetic data, but there are only a handful of robust poles for the entire Neoproterozoic (Evans et al., 2021). Consequently, understanding past environmental change is typically done by extrapolating from a small number of underlaying data from limited locations.

Here we present a novel open-source method that reconstructs global-scale palaeogeography by leveraging information built into a full-plate tectonic model to trace mountain and ocean building regions through time. Using present-day topography as a guide, we attribute each tectonic region with an elevation profile to simulate how palaeotopography may have changed through time. Our approach models the topography of any point as the integration of all events that have influenced that location since the beginning of the reconstruction. We use each previous timestep as a boundary condition for the current timestep, meaning that our model is deterministic, and both grows and erodes orogens through time. Our approach is rapid to run (~30 minutes) and reproducible, allowing the model to be rerun with different parameters to test and generate different hypotheses and palaeogeographic histories. For the purpose of understanding the surface evolution of Earth through deep time and the relationship between

gross tectonic changes and the atmosphere and hydrosphere, we aim to produce our model at a target resolution of $\sim 1^{\circ}$ spatially and $\sim 1-10$ Ma temporally.

1.1 Background

While there is a general, informal language in the community around the different styles of 'palaeogeographic' models, we outline below the specific definitions we use in this contribution. We broadly follow previous work (Markwick and Valdes, 2004; Vérard et al., 2015; Torsvik and Cocks, 2016; Cao et al., 2017; Merdith et al., 2017; Domeier and Torsvik, 2017; Scotese, 2021; Seton et al., 2023) and note that most models could easily be described by multiple definitions, with many of the distinctions being semantic and differing across models, research groups, and as the community develops new ideas over time. They are not intended to be prescriptive of different models, but as our work blends and discusses different approaches we want to provide clear working definitions. Figure 1 provides an overview of the discussed model types below.

1.1.1 Palaeocontinental reconstructions

The starting point, and most basic, of all reconstructions is a palaeocontinental reconstruction, which is simply the restoration of modern-day continents to some position in the past (e.g. Fig. 1) (Scotese and McKerrow, 1990). This style of reconstruction is what is often referred casually to as a palaeogeographic reconstruction, however, for this study we prefer the phrase palaeocontinental because their purpose is to understand the ancient position (either absolute or relative) of continent(s). The preservation of magnetic reversals in ocean crust can be used to constrain the location of the continents for post-Pangea ages (Fig. 1a), however for earlier times we rely chiefly on palaeomagnetic data (Fig. 1b). The quality and abundance of available data can be highly variable depending on what time and where in the world one is looking for information (e.g. Evans et al., 2021; Seton et al., 2023).

Palaeocontinental reconstructions can be either global or regional. Global models must use palaeomagnetic data of individual continents to produce continuous motion paths because it is the only method to quantify absolute motion for times earlier than the Jurassic (Besse and Courtillot, 2002; Torsvik et al., 2008, 2012; Li et al., 2008; Wu et al., 2020; Vaes et al., 2023). Alternatively, regional models can be made at discrete timesteps or by not restoring the absolute position of a continent, and often describe the paleotectonic evolution of a region. In the first of these cases, regional models are often strongly based around the ages of preserved geological observations, summarising key stages in the tectonic development of a region (e.g. orogenesis, terrane collision, rifting etc. Fig. 1c). In the second of these cases, the data are often used to show the motion of continents relative to a fixed position, often to help discriminate against specific end-member scenarios. For example, during the Neoproterozoic when the supercontinent Rodinia existed, Laurentia is often depicted as fixed in its present-day position and other continents are reconstructed to the margins of Laurentia based on geological data (e.g. Moores, 1991).

1.1.2 Full-plate reconstructions

Full-plate reconstructions merge and/or extend regional or palaeotectonic palaeocontinental reconstructions into a single reconstruction. Here the palaeotectonic information is turned from implicit suggestion of tectonic regime (e.g. continental arcs) to explicit model of a tectonic boundary (e.g. subduction zone) by mapping plate boundaries onto the palaeocontinental reconstruction using programmes such as GPlates (www.gplates.org) (Gurnis et al., 2012; Müller et al., 2018) (Fig. 1d). These models are the current state-of-theart in terms of understanding Earth's plate tectonic evolution (for example, see reviews in Merdith et al., 2021; Seton et al., 2023). They use palaeomagnetic data, where available, to constrain absolute position, but the relative motions (especially for the pre-Jurassic) are geologically derived, constrained by the lithological, structural, metamorphic, geochemical and geochronological evidence of plate-interactions. Importantly, because full-plate models must adhere to basic constraints offered by plate tectonic theory, the models interpolate between known regions of the geological record (e.g. inferring a continuous subduction zone) and extrapolate both the known and highly confident regions into the unknown (e.g. extending a subduction zone away from a continental margin into an ocean basin, Fig. 1e). These extrapolated plate boundaries are built to constrain the relative kinematic motion suggested by the underlying palaeocontinental model.

The interpolated and extrapolated plate boundaries then form the interconnected network of tectonic plates that cover the Earth's surface. As the whole globe is modelled, a full kinematic history of the planet, including of extinct ocean basins is provided. In these extinct ocean basins, the kinematic motions are built to ensure (as much as possible) that subduction zones maintain convergence, and mid-ocean ridges maintain divergence, thus ensuring the model remains consistent with plate tectonic theory. The exact orientation and distribution of plate boundaries, especially within extinct ocean basins, is an iterative, and qualitative process producing a non-unique solution. Finally, there are different hypotheses that propose to constrain palaeolongitude through time (Torsvik et al., 2010; e.g. Mitchell et al., 2012; Müller et al., 2022) and each different method and model uses different assumptions that give different estimates of past continental palaeolongitudes.

1.1.3 Palaeogeographic reconstructions

We define a palaeogeographic reconstruction as a type of reconstruction distinct from both palaeocontinental and a full-plate reconstructions, in that they map past environments onto continental surfaces (Vérard, 2019a; e.g. Poblete et al., 2021; Scotese, 2021). In the simplest manner, this happens by mapping the sea level onto a palaeocontinental reconstruction, depicting how the area of flooded continents change through time (Ziegler et al., 1979; Scotese, 2001, 2021; Golonka, 2007; Blakey, 2008; Vérard et al., 2015; Torsvik and Cocks, 2016; Cao et al., 2017; Marcilly et al., 2022b). This is typically done using geological fossil and/or sedimentary facies data to constrain the position of past shorelines (Fig. 1f). More sophisticated models can offer further palaeoenvironment differentiation beyond 'land' and

'sea', using additional geological data to trace environments such as shallow marine, coastal plains, continental shelf, deserts, forests or mountains (Fig. 1g).

At its most complex, a paleogeographic model is a complete digital model of paleotopography and paleobathymetry. Existing approaches to reconstructing palaeotopography are based predominantly on available data able to constrain past elevation at specific times, and the scale of the desired aim (e.g. global or regional, recent geological history or deeper time). Recent studies have summarised, and demonstrated a number of these approaches, including lithological indicators, palaeoaltimetry, geochemical proxies and methods to estimate uplift and erosion, to produce regional palaeoelevation maps (Rowley and Currie, 2006; Boschman, 2021; Liu et al., 2024). An important distinction in their creation is presented in Marwick and Valdes (2004) who discuss the tension between map precision and extent. Typically, because of the heterogenous nature of geological data (in both a spatial and temporal sense) as the extent (spatial coverage) of the desired map increases, the precision (how accurately the map represents a specific time) often decreases. Consequently, a map is often presented as a time slice, that incorporates data from a time range (for example, summarising all available data from an epoch). As noted by Marwick and Valdes (2004), the resulting maps most likely do not offer a 'true' representation of what the Earth was ever like because (in many cases) the maps are made by integrating available data over a time range that might vary between 1 and 10 million years (consider, for example, sea level change just over the last 20 ka). Instead, they offer a summary from a small discrete period of time, often with different regions being supported by underlying data of slightly different ages.

1.2 Current models

Irrespective of the data used and the methodology employed, all palaeotopographic models require at least two things: some collation of the quantitative and/or qualitative data on past topography in space and time, and some methodology on how the 'gaps' between the data in the study can be filled. Models, which can either be global or regional, tend to follow similar approaches to both problems, though with caveats to the style and amount of data used, and as to how well the processes used to fill the 'gaps' are documented. Much of our discussion here focusses on global models, as that is what our primary aim for this study is.

1.2.1 Global models

The most well-known models are very large in scope, covering the entire globe, typically for time periods as long as the Phanerozoic. Two models in particular that are widely disseminated both in and outside of academic literature (such as through outreach, public science events or industry) are the PALEOMAP model(s) by Christopher Scotese (2021) and Deep Time Maps by Ron Blakey (2008). In both cases authors have amassed and synthesised large amounts of qualitative and quantitative data into a geological interpretation, building a descriptive model of the Earth's surface elevation through time. Scotese (2021) primarily used lithological and palaeontological databases to determine changing elevation through time. In his model(s) different lithofacies, preserved rock types or structural data can be mapped to key tectonic

environments, of which an estimate of topography can be established at present-day (Ziegler et al., 1985). For example, large alluvial and floodplain complexes along with swamps, lagoons and channel sands are indicative of subaerial, but low-lying land (0–200 m above sea level). Comparably, high-pressure and high-temperature metamorphic rocks are mapped to highly elevated areas indicative of continental collision (4000–7000 m above sea level). We note that the compiled work of Scotese dates back decades (e.g.) (Scotese and McKerrow, 1990; Scotese et al., 1999; Scotese, 2001, 2004; Scotese and Wright, 2018), for brevity we refer to his most recent model published in 2021 (Scotese, 2021, SCO21) that synthesises many of his advancements and methodologies into a single publication.

The deep time maps of Blakey (2008) followed a similar approach to the works of Scotese, with some minor differences. Firstly, in scope, despite being a global model Blakey (2008) focussed more specifically on Gondwana, Pangea and Gondwana derived terranes rather than other areas of the world, such as the pre-Pangea Arctic region, or post Pangea breakup. Secondly, Blakey (2008) used several key pre-existing reference models to inform the basis of his work, this is in contrast to Scotese who used databases of lithological indicators. Presumably, similarly to the Scotese PALEOMAP models, areas of tectonic convergence and continental collisions are depicted as mountainous, while passive margins depict the process of continental rifting and breakup. Finally, to our knowledge, there is no explicit rotation file or set of reconstruction files (that could be looked at in *GPlates* for example), rather the construction of these maps was done by organising the continents, blocks and terranes on a rectangular globe, and then overlaying different tectonic elements from key references to determine locations of key tectonic features such as mountain ranges, passive margins and rift shoulders.

The developments of new plate reconstruction tools, such as GPlates (Müller et al., 2018) and pyGPlates (Mather et al., 2024), and of large databases such as the Paleobiology Database (PBDB), have been instrumental in the development of new, alternative models to PALEOMAP and Deep Time Maps. Torsvik and Cocks (2016) (see also analysis and discussion in Marcilly et al. (2021, 2022b)) have produced an integrated palaeogeographic model over Phanerozoic time that is tightly linked to their plate reconstruction (though without plate boundaries). Their model focusses more strongly on the changing flooded continental areas and sea level, rather than mountainous topography. Here, they chiefly use palaeontological and lithofacies data to constrain past shorelines and the area of continental crust that is inundated by ocean water. Similarly, Cao et al. (2017), using pyGPlates, also used the PBDB to better constrain the coastlines in the palaeogeographies of Golonka et al. (2006) since the late Devonian. The results of Cao et al. (2017) are similar to Torsvik and Cocks (2016) in that they chiefly map shoreline (as an estimate of continental flooding) through time, but they also include a subdivision on land of mountainous and ice-covered regions, permitting some estimate of topography through time (e.g. in the Meso-Cenozoic climate simulation ensemble in Leonard et al. (2025)).

Finally, the work of Christan Vérard takes a slightly different approach, where quantitative relationships between elevations and tectonic features are defined for the present-day and for

certain well-constrained regions back in time (Vérard et al., 2015). This model, called PANALEISIS, assumes uniformatarianistic principles (which we also do in this work), and applies these quantitative relationships to earlier times to produce palaeotopographic maps. Unfortunately, this model is proprietary and consequently not publicly available. An extension of this work has been published for the time period from 888 to 444 Ma, encompassing the breakup of Rodinia and amalgamation of Gondwana (Vérard, 2021), though it does not contain elevations or estimates of flooded continent areas.

The greatest hinderance with many (but not all) of these global models pertains to their reproducibility. This is principally because their development preceded the recent push to 'open access' science and scientific methods (it is noteworthy in particular that the PALEOMAP models have been slowly changing to reflect this) and many, including the models of Blakey (2008) and Vérard et al. (2015) are either designed for, or owned by industry and thus not (currently) available for wider use by the scientific community. Either way, the majority of publications only variably supply, or explain, the underlaying data, model files or the decisionmaking processes used in the model construction. For example, there is no rotation file or set of polygons provided for users in the model of Blakey (2008), and the underlaying data that was used in Scotese (2021) is also not included in the publication. This makes it both difficult for others to reproduce the work, but also difficult to understand what decisions were made and why they were made, especially in regions and times with little data. It is assumed (perhaps wrongly?) that in data-poor times and regions the model is simply interpolated between the more well constrained areas, however, except for the PANELESIS model of Vérard (2015), there is not explicit documentation of how these gaps are dealt with. The practical impact of this is that, for users, there is a disconnect between the underlying data (i.e. the geological record) and the final 'product' (i.e. the resulting model), and while these models are widely used there remain fundamental questions pertaining to uncertainty and confidence in the resultant palaeogeographic maps.

Despite this drawback, the strength of these models like PALEOMAP and PANELESIS are that they offer global coverage at many epochs of the Phanerozoic. As many interesting questions stem from having a global palaeogeographic model, they are incredibly useful for further understanding how different surface systems have changed through time. For example, expert derived global palaeogeographies are used in both oceanic circulation modelling (Pohl et al., 2022) and climate modelling (Goddéris et al., 2014; Valdes et al., 2021; Marcilly et al., 2022a). They are also used to drive carbon cycle modelling, (Goddéris et al., 2012), studies of deeptime biodiversity (Cermeño et al., 2022), biogeochemical modelling (Mills et al., 2021) and landscape evolution modelling (Salles et al., 2023).

1.2.2 Our approach

In this contribution our approach is to produce a holistic, deterministic palaeogeography (including topography and bathymetry) that is based on estimating orogenic growth forwards in time using a full-plate reconstruction model. Our approach builds both a bathymetric and topographic layer that are then summed to produce a deterministic palaeogeography. As full-

plate models are internally both spatially and temporally consistent and continuous, our aim is to produce a model that uses previous timesteps as an input to determine the topography of the current timestep.

Our primary motivation for making these palaeogeographic maps is to then use them as a basis for palaeoclimate and landscape evolution modelling to assess how Earth's surface conditions have changed over the last 1 Ga. We are principally interested in using these maps as boundary conditions to drive palaeoclimate models, which tend to have a spatial resolution between 2-6° (200–600 km) and, as the movement of Earth's tectonic plates is around 50 km per Ma, a temporal uncertainty of approximately 10 Ma. Despite this, our workflow can generate maps at higher temporal or spatial resolution at the cost of computational time, thus here we opt for maps at 1° resolution and every 1 Ma. This degree of resolution also broadly corresponds to how we treat time sensitive data that constrains maximal flooding surfaces and palaeoshorelines (see section 2.5 and the discussion in Marwick and Valdes (2004). For example, in the Phanerozoic, we rely principally on the PBDB, with fossil data binned according to their geological ages and then used at each million-year timestep across the duration of the age. The Maastrichtian, from 72.2 to 66 Ma, will have six output maps that all use the same PBDB data, that is any fossil with a depositional age between 72 and 66 Ma, to constrain maximum flooding. For the Neoproterozoic we use a detrital zircon database (Puetz et al., 2024), but follow a similar approach, where the uncertainty in zircon deposition age of interpreted marine sedimentary rocks is used to constrain flooded continental regions at all times within that uncertainty window (i.e. a dispositional uncertainty of 34 Ma would mean that the zircon data are used for all 34 maps). In this manner, the temporal resolution of the final maps will essentially be the duration of the geological age in which they were constructed for in the Phanerozoic, and for the Neoproterozoic, it will be the 50 Ma mean range in zircon (depositional) age, though this is highly variable (~47 Ma std) (Puetz et al., 2024).

The method we present here is unable and not designed to recreate or replicate the level of detail that is observed in the present-day topography. Instead, we are primarily interested in where mountains once existed on Earth, and whether they were very high (> 4km) somewhat high (1–4 km) or low (< 1 km). Similarly, we are interested in where deep ocean basins and shallow seas, such as flooded continental regions, were. Among many shortcomings, our analysis is unable to properly recreate or represent many erosional features such as valleys and peaks and is also unable to resolve the bathymetric changes that come from sedimentary deposition in ocean basins. Despite this, our approach is parameterised, meaning that a user can produce alternative interpretations of the palaeogeography by altering input conditions, allowing for the user to test different assumptions about topography, and generate maps that represent different scenarios. While we showcase our method against an already published plate reconstruction, it can (in theory) be applied to alternative models.

2 Methods

We use a full-plate tectonic motion model with evolving plate boundaries and plate polygons that runs from 1000 to 0 Ma (Merdith et al. 2021, hereafter MER21). Our method is designed

to work with this type of plate model because they contain prior information about both the location, duration and nature of plate boundaries and continental crust that help regulate where some different topographic environments occur. The description of our approach is broken into five sections. We describe the framework that we have implemented to estimate change in topography through time (2.1), then we describe how we build palaeotopography (2.2) and palaeobathymetry (2.3) and combine them into a single palaeogeographic grid (2.4), we finish by describing how we approach flooded continental regions, forming our final palaeogeography (2.5). Our supplementary material includes a full equations file and the code to reproduce our results.

2.1 Building blocks

As the primary building block for our model, we use a series of 'nodes' that encompass the continental extent and trace these through time—an approach broadly similar to recent approaches used to reconstruct ancient seafloor (Merdith et al., 2019; Karlsen et al., 2020; Williams et al., 2021). We use an equal-area mesh within the continent-ocean boundary (COB) polygons to generate a suite of nodes, where each node (n) has an unique identifier, as well as the attributes of a present-day latitude and longitude, plate-ID, and valid time (start and end) determined from the polygon it is contained in, allowing us to reconstruct each node to any time in the last 1 Ga (Supplementary Equation 1 (SEq. 1)), as well as determine if this node is active (based on its valid time). While there are uncertainties about the exact fit between continents, especially in pre-Pangaea times, using the COB polygons results in nearly all nodes with an end time of 0 Ma; the nodes that are not valid at 0 Ma arise from past changes in the continental extent (and hence, COB polygon) due to scenarios such as major continental continental collisions, or due to changes required for masking purposes.

2.2 Palaeotopography

We estimate changes in palaeotopography arising from four types of tectonic processes:

- 1) Continental arcs—the subduction of oceanic crust under continental crust produces long, high mountain chains (e.g. Andes, Indonesia) (Fig. 2a) (Section 2.2.1).
- 2) Continental collisions—collision of two continents, resulting in plateaus and mountain ranges (e.g., Himalayas) (Fig. 2b) (Section 2.2.2).
- 3) Rift environments—continental rifting, which results in a long valley or depression that eventually submerges, parallel to the rift axis. (e.g. East Africa) (Fig. 2c) (Section 2.2.3).
- 4) LIPs—Emplacement of large igneous provinces (LIPs), which produces low to medium topographic relief in a dome around the centre of the LIP (Fig. 2d) (Section 2.2.4).

We extract a suite of variables (Table 1) at our nodes to identify the regions associated with each of our four categories for changing palaeotopography. After isolating a tectonic category, the nodes within the region are given a growth and decay factor attribute to stimulate their topographic evolution (Section 2.2.5). The extracted variables used to isolate tectonic

environments from the plate tectonic reconstruction (i.e., MER21) relate to the changing nature of subduction zones (SZ1, 2), plate motion velocity (VEL1–3) and continental polygons within the plate model (representing estimates of where continental lithosphere once was; POLY1–5). We additionally include a LIP database (Park et al., 2021) to trace where LIPs are known to have emplaced on Earth's continental lithosphere (LIP1). While we originally extracted >12 variables from the plate tectonic model to isolate environments, we ended up finding that these nine variables were sufficient to identify the four environments in our analysis.

Table 2 summarises our default threshold parameter choices, and below we describe how we isolate different environments using the extracted variables in Table 1, and Figure 3 shows a flowchart of this part of our method.

2.2.1 Continental arcs

Continental arcs form on the boundaries of continental lithosphere from the subduction of oceanic lithosphere and represent a convergent plate boundary. We identify continental arc environments based on the distance of a node to the closest downgoing subduction zone (SZ1), where an arc environment is assigned if a node is within 450 km (based on results from Zahirovic et al., 2022) (Fig. 4). This distance is scaled by the duration of time that has passed since that node has last seen an orogenic event (Hasterok et al., 2022), representing that weaker crust is more easily deformed and typically represents areas where terranes accrete over time (e.g. Central Asia, western USA) (Equations 4, 5).

2.2.2 Continental collisions

Continental collisions arise when two pieces of continental crust on separate plates collide and the intervening ocean basin is consumed by subduction, resulting in lithospheric thickening and the formation of a large plateau and high topography. Due to the processes involved in continental-continental collisions, we rely on a six-criterion approach to determine regions of continental collision, where all criterion need to be satisfied for a continental-collision to be detected. We note that the combination of the six criterion helps prevent incorrectly identifying areas of continental collision, as much as they isolate correct areas. The criteria are:

- i. Continental collisions occur immediately after the cessation of a continental arc
- ii. Overriding continental polygon is of sufficient size to support extensive thickening
- iii. Distance from node to nearest polygon (other than its containing polygon)
- iv. Area of nearest polygon (other than its containing polygon) to node
- v. Changing distance from the polygon containing the node to nearest polygon
- vi. Convergence direction from the node to the nearest node on nearest polygon

The first criterion is that continental collisions must occur directly after the cessation of a continental arc, but the two environments are mutually exclusive. Once two continents collide through subduction of the intervening ocean basin, relative convergent plate motion either stops and the continents are sutured (without generating a high plateau), or convergent motion

continues but there is no longer a delineated subduction zone plate boundary. In the plate tectonic model, this is represented by an active subduction zone becoming inactive. As such, we use the distance of a node to the closest subduction zone (SZ1) over the previous 10 to 1 Ma of a timestep in question (Equation 5, Figs. 5a, b). We use a distance threshold of 2800 km based on the horizontal distance perpendicular to strike of the Himalayan plateau from the India-Asia suture.

The second criterion is an area test, where we ensure that the overriding plate polygon is large enough to support extensive thickening. Evidence from the geological record suggests only a handful of collisions have produced large-elevated regions like the Tibetan Plateau (REF). As such, we determine if the area of the COB polygon the node is within (POLY1) is above the threshold of $4 \cdot 10^7$ km² (Equation 6). This threshold is the approximate size of present-day Australia and was chosen as we found it gave a reasonable result for predicting the present-day continental collision zones (Figure. 5c, d).

Criterion three assesses the distance from node to nearest polygon (POLY3) test (Equation 7; Figs. 5e, f). It requires the POLY3 distance at the previous 10 to 1 Ma timesteps to be decreasing, while at the current timestep the POLY3 distance to be larger than the distance 1 Ma earlier. This change in distance reflects a polygon continent getting closer to the node-polygon over time merging with the node polygon, thus at the current time the new nearest polygon is much further away. To prevent locating just adjacent polygons that have no relative motion (e.g., Madagascar and Africa) We also include a hard test to protect against edge effects, where we check that the previous timestep the nearest polygon was within 2000 km of the node.

The fourth criterion ensures that the size of the 'nearest' (i.e. colliding, downgoing) polygon is sufficient to cause significant underplating, where the area of the nearest polygon (POLY2) at the previous timestep needs to be larger than a threshold (Equation 8; Figs. 5g, h). This is to ensure the colliding continental crust is of sufficient size that when subducted, the overriding plate results in plateauing and forms a large Himalayan-style mountain range, rather than the deformation, partial subduction, and accretion to the continental margin that tends to occur with small blocks. We consider modern-day India to be a reasonable example of such a continent, thus set the threshold to $7 \cdot 10^6 \text{ km}^2$.

Fifthly, we analyse the distance from the polygon containing the node to nearest polygon (POLY5). Here we want to ensure that the nearest polygon to our node polygon (i.e. the polygon that contains the node) is close at the timestep prior to the analysis time (the main reason for this criterion is that it helps with protecting the model against false positives). Equation 9 shows this relationship, as does Figs. 5i, j, and we select 500 km as our default value.

Our sixth criterion assesses the motion of the node relative to its nearest polygon, to ensure any potential convergence is occurring 'head on' rather than at an oblique angle. To do so, we calculate the azimuth of the node from its nearest polygon (VEL2), and the azimuth of the velocity vector of the node itself (i.e., the polygon which a node is contained within) (VEL1),

and find when the difference between these two values $< 30^{\circ}$ (Equation 10 and 11 and Figs. 5 k, 1) (VEL3).

We determine nodes to be within a 'continental collisional' environment if they satisfy all the above criteria (Equation 12). Fig. 5m shows the intersection at 50 Ma (which is when the polygons in our model between India and Eurasia merge).

2.2.3 Rift environments

Our approach for identifying rift environments is based around finding regions where our polygons have split, representing continental breakup. Here we identify regions where nodes are now much closer to the edge of the polygon (i.e. closer to 'new' ocean basins) than the previous time step, to isolate the regions of the polygons that are now facing the incipient 'ocean' basin. Conceptually, this reflects the rupturing of continental lithosphere and exposure of continental interiors to incipient ocean basins.

We find how the distances to polygon boundary (here representing the synthetic ocean-continent boundary in the model) changes through time to determine rift environments. To do this we take the difference between the current time step and the time-step one in the future (i.e. t-1) and put in place a limit for how far inboard from the incipient ocean the rift should have extended to determine whether a node could be in a rift environment (Equation 13). We set this limit to 400 km, thus isolating regions that are now much closer to an ocean basin than previously (Fig. 6). Importantly, this approach only isolates what has changed in the past 1 Ma and traces, what could be considered, as the cessation of rifting that marks the transition to seafloor spreading (i.e. the identified area in Fig. 6b is the last timestep of 'rifting' before seafloor spreading takes over). Later in our method, when we come to estimate our changes in rift elevation our model will look forward in time to find any of these regions to model topographic change in a rift environment.

2.2.4 LIPs

LIPs can cause minor topographic relief due to the buoyancy of hot material uplifting the lithosphere, and due to the thickening of the lithosphere resulting from the emplacement of lava. In our model, we only consider continental LIPS and their doming effect of the dynamic uplift driven by plume buoyancy. We do not consider oceanic plateaus or oceanic LIPS, or the added elevation that emplaced lavas might contribute to continental topography. We use a set of continental LIP polygons from Park et al. (2021) and reconstruct them to their time of emplacement using the plate model. Where a node is contained within a LIP polygon we infer some uplift would have occurred (Equation 14). Saunders et al. (2007) analyse five of the major Phanerozoic LIPs, and suggested that the earliest evidence of uplift (where available) occurred less than 2.5 Ma before emplacement. In our model we initiate this uplift from the age of the LIP emplacement, as recorded in the database of Park et al. (2021) and keep it active for 10 Ma (i.e. if a LIP emplaced at 100 Ma, uplift only occurs until 90 Ma) (Fig 7).

2.2.5 Building global topography

We incorporate our identified tectonic settings into an initial global palaeotopography reconstruction using a two-step process, starting from our oldest time (i.e., 1 Ga) and moving forward to present day in 1 Ma timesteps (Figure 8).

First pass

On the first iteration we reconstruct each node to its palaeo-latitude and -longitude, and determine if the node is either in a 'continental collisions' or 'rifts' setting (i.e. Equations 12, 13, see Sections 2.2.2, 2.2.3) as a Boolean mask (i.e., 1 for True, 0 for False). We assess the continental collision and rift settings on our first iteration, as they are both ongoing events without a clear plate boundary that marks their duration (unlike, for example, a continental arc).

Second pass

During the second pass we reconstruct our nodes forward through time and incorporate time-dependent and evolving palaeo-elevation estimates based on the node's tectonic setting attributes, combined with user-configurable parameters including representations for 'growth' and 'erosion' (see Table 2 for our preferred values). We prescribe the palaeo-elevations for the initial 30 Myr (i.e., between 1000 and 970 Ma; Fig. 9) as the model's starting condition, akin to a 'spin-up', as our calculated elevations do not evolve in height during this time. Within this spin-up, we set regions attributed as continental arcs as 700 m, else all other regions are assigned 150 m (there are no LIPs during this time). We manually incorporate the Laurentian portions of the Grenville Orogen, a known Rodinia-forming orogeny, using the outline from (Pehrsson et al., 2016; Hasterok et al., 2022) (Equation 15, Fig. 9) and prescribed it an elevation of 2000 m. Other similar aged ('Grenvillian') orogens also exist, but we limit our starting condition to the orogen that forms along the eastern and southern margins of Laurentia that represents the formation of the core of the reconstructed Rodinia in Merdith et al. (2021). We note that applying our workflow to plate tectonic reconstructions extending into the Mesoproterozoic (e.g. Cao et al., 2024) may render this step unnecessary.

Following our spin-up (i.e., at 970 Ma), we incrementally iterate in 1 Myr timesteps to present-day. The palaeo-elevation from the prior timestep forms the initial basis for each new timestep (Equation 16). We isolate nodes associated with each tectonic setting (continental collisions, rifts, continental arcs, continental LIPs) from the previous-determined node attributes. For rifts and continental collisions, we additionally explore the node attributes in the prior and following 40 Ma to decide between the two options—whether the node is within a continental collision or a rift environment (Figure 10, Equations 17 and 18 respectively). Palaeo-elevations at the time-step in question are subsequently determined in one of three ways: for tectonic settings causing an increase in elevation, an exponential multiplier is applied to our tectonic settings, and all other regions are given a multiplier of '1'. The multiplier reflects the increase of topography per Myr for a node within a given active tectonic setting given its prior topography and has different parameters (Equation 19):

$$n_{ctopo} = n_{ctopo} + \left(topo_{\min grow} + \frac{topo_k}{e^{node}_{ctopo} \times topo_{\lambda}}\right)$$
 (19)

Where $topo_{\min grow}$ is the horizontal asymptote (Table 2), reflecting the minimum amount of growth we might expect from any topographic process, while $topo_k$ and $topo_{\lambda}$ are scaling and decay parameters in the exponential equation for each tectonic setting, reflecting the y-intercept, and strength of the decay curve respectively (Figure 11). In the model, we perform these growth calculations sequentially, in the order 'arc', 'continental collision' and then 'LIP', with the n_{ctopo} being updated after each one (i.e. the current topography in the LIP calculation includes the calculated growth for both arc and continental collision environments).

In contrast to continental collisions, modelling topographic change in the pre-determined rift regions is more complicated. We assume a stylised conceptual model of rift topography, where nodes that are determined to be within a 'rift-zone' decrease in elevation (representing subsidence) at a linear rate until the ocean basin forms. To do this we first calculate how many timesteps (in Ma) from our model time until the rift 'ends' with ocean basin formation (i.e. $node_{time\ until\ rift\ flag}$, for each node, how many Ma until Equation 18 is satisfied?). For these nodes we then compute the average decrease in topography from the model-time to when an ocean basin forms, assuming a $min_{rift\ topo}$ of -200 m (i.e., submerged), like so:

$$n_{\Delta rift\ topo}(t) = \frac{n_{ctopo} - min_{rift\ topo}}{node_{time\ until\ rift\ flag}} \tag{20}$$

Which is then subtracted from the active nodes:

$$n_{ctopo} = n_{ctopo} - n_{\Delta rift \ topo}(t) \tag{21}$$

Figure 12 shows Equations 20 and 21 applied to nodes between 200 and 160 Ma during the opening of the Atlantic.

Finally, at the end of the timestep after calculating topographic change in continental arc, continental collision, LIP emplacement and rift regions, we begin our implementation of erosion (Fig. 13a). Firstly, using the current calculated topography (i.e. after the detected changes described above) we determine the local relief ($n_{local\ relief}$) of each node. We do this by firstly calculating the median height ($n_{median\ topo}$) of each node using the 21 nearest nodes (Figure 13b). We then subtract the median height of each node from the calculated node height (n_{ctopo}) and take the absolute value (Fig. 13c) to determine local relief (Equation 22). We then use local relief to estimate erosion, following Montgomery and Brandon (2002) (Equation 23).

$$n_{local \, relief} = \left| n_{ctono} - n_{median \, tono} \right| \tag{22}$$

$$n_{erosion} = \varepsilon_{min} + \varepsilon_k \times \arctan\left(\left(\varepsilon_{offset} - n_{local\ relief}\right) \times \varepsilon_{\lambda}\right)$$
 (23)

In Montgomery and Brandon's (2002) empirically derived curve, they have a vertical asymptote at 1500 m local relief that corresponds with incredibly high erosion rates (10 mm/a or ~10 km/Ma). Our implementation of this equation has a few changes detailed below, principally because our model is a much coarser resolution than the data used in Montgomery and Brandon (2002). We found that when we implemented their equation, there were a number of artefacts introduced in the model that occurred from calculating erosion over a million-year duration rather than yearly, and also because occasionally our model would calculate an extremely high local relief (>3 km, occurred occasionally when new polygons and nodes were turned on in the model), which would suggest an erosion amount in excess of 10⁶ km, crashing the model.

We firstly use an arctan function to introduce a second horizontal asymptote to protect against erroneously high relief. Secondly, we reduce the erosivity by a factor of \sim 15 (i.e. at 1500 m erosive power is 0.6 mm/a, corresponding to 600 m/Ma of erosion. If we were to upscale the curve of Montgomery and Brandon (2002) to a Ma timeframe directly, that would imply 10 km of erosion per 1500 m of local relief. Finally, because we have a second horizontal asymptote, we have our vertical asymptote occurring at 2000 m local relief (ε_{offset}). We found when we implemented it at 1500 m that many topographic features would vanish very quickly, likely due to the coarser temporal resolution (e.g. a feature at 1500 m would have \sim 600 m erosion in one timestep). By using 2000 m as our asymptote, it means that the rate of erosion drops off at the same point as the Montgomery and Brandon (2002) curve, despite our longer timeframe. We do not redistribute the eroded material in our analysis. Table 2 details the values for the different equation parameters.

This gives an amount in metres that the modelled elevation decays by, which we subtract as the final last calculation at each timestep to get the final topography of the nodes at the timestep like such (Equation 24):

$$n_{ctopo} = n_{ctopo} - n_{\varepsilon} \tag{24}$$

We then set the topography for that time to the calculated current topography (Equation 25):

$$n_{topo}(t) = n_{ctopo} (25)$$

And progress to the next timestep until t = 0, where upon finishing that timestep the model run completes.

2.2.6 Palaeotopographic grids

Once our model run is complete, we are left with a distribution of nodes over the Earth's surface representing our modelled elevation estimates (e.g. Fig. 14a). To make a set of regular grids we use *blockmedian* and *sphinterpolate* (spherical interpolation) in *pyGMT* (Uieda et al., 2021) to first create an 'xyz' (latitude, longitude, elevation) table of representative values (*blockmedian*

function) before interpolating them onto the regular latitude-longitude grid using *sphinterpolate* at a 0.1° resolution. Finally, we use *grdfilter* to smooth and resample the modelled topographic data onto a 1° grid, using a Gaussian function with 1° width (Fig. 14b). At this point, our grids are now ready for some post-processing steps: merging with our palaeobathymetry (Section 2.3) to make a palaeogeographic model (Section 2.4).

2.3 Palaeobathymetry

For palaeobathymetry we follow the established method (Müller et al., 2008) of estimating palaeo-basement depth of ocean basins based on the oceanic crustal age using a plate cooling model (e.g., Stein and Stein, 1992; e.g. Crosby and McKenzie, 2009). Synthetic oceanic crustal age grids based on the evolution of mid-oceanic ridges and the MER21 plate tectonic model were created at a 0.1° resolution via the method of Williams et al. (2021), and subsequently resampled to a 1° using a Gaussian filter through the *(py)GMT* function *grdfilter* (Uieda et al., 2021). We rely on the GDH1 oceanic age-depth relationship (GDH1, Stein and Stein, 1992). As much of our time of interest relies on oceanic crust that is synthetically reconstructed, we do not explicitly include key bathymetric features including trenches, LIPs, plateaus, seamounts, and seafloor sediments. Figure 15 shows the calculated palaeobathymetry at set time slices over the last 1 Ga.

2.4 Palaeogeography and smoothing parameters

At this stage of our workflow, we have two separate sets of grids spanning the last 1 Ga. The first set is of our modelled palaeotopography, and the second is of our modelled palaeobathymetry. Our modelled palaeotopographic maps require some smoothing in order to blend the terrestrial and marine elevations, as in many cases along coastal regions there are large topographic 'steps' between adjacent cells (> 1 km), and our model does not fully consider coastal and continental shelf environments. Figure 16 is a flowchart summarising this final phase of our workflow.

To incorporate such regions, we firstly use ETOPO to extract the topographic values corresponding to continental shelf and coastal regions. We define coastal regions as regions between -200 and +150 m elevation along the modern day shoreline and that are up to 400 km landwards of the -200 m contour. We select -200 m to reflect the transition from continental slope to shelf and 150 m as this is our 'starting' elevation of our model (thus preventing the topography from forming a 'bowl' around continental interior, inhibiting drainage networks). Using these extracted values, we create a hypsometric curve using their elevation-distance distribution (Fig. 17–18) that represents a realistic elevation profile along coastal regions. We then extract the same corresponding regions from our modelled topography (-150–200 m, and up to 400 km inland, e.g. Fig. 19) and map the corresponding depths and elevations from our hypsometric curve onto the gridcells. This creates our 'final' smoothed palaeotopographic maps (e.g. Fig. 20.) that we sum with the modelled palaeobathymetry at each timestep together to produce a 'global' palaeogeographic grid (Fig. 21).

2.5 Continental flooding regions

The final post-processing step is done separately to the forward model of topography and bathymetry and smoothing. We draw a distinction here in our method where until this point our model has been deterministic and driven by quantitative relationships between different tectonic environments, but now is constrained by sparse data and has some degree of subjectivity. In particular, the determined topography at this point is likely to be more useful for a range of applications, such as modelling dynamic topography or erosion, where robust comparisons need to be drawn to the geological record. Similarly, geodynamic motivations such as the isostatic load and gravitational potential energy of mountain ranges or plate driving forces are also unlikely to be interested in the precise locations of palaeoshorelines.

In this section we describe how we apply a series of predetermined masks onto the grids that represent the extent of flooded continental crust, and hence is some reflection of relative sea level change. To do this we use two existing datasets that provide some idea about the aerial extent of oceans encroachment onto land. For the Phanerozoic we use the Palaeobiology Database (PBDB, https://paleobiodb.org/), and for the Neoproterozoic we use a database of detrital zircons that have been filtered to include depositional ages (Puetz et al., 2024).

2.5.1 PBDB

In our analysis we use data available within the PBDB to further constrain sea-level high stands at each geological stage in the Phanerozoic. Similar to the approach of Cao et al. (2017), we used data (downloaded on Y date) with age constraints, present-day coordinates, and depositional environment, and further classify fossil data into broader 'marine' or 'terrestrial' environments based on Cao et al.'s (2017) criterion, resulting in ~1,400,000 unique fossil entries (Fig. 22). Using *pyGPlates* (www.pygplates.com) and the MER21 tectonic model, fossil locations were reconstructed to their deposition palaeo-location, and the data at each stage level (taking only fossils that had a depositional age that fell within that stage) saved to a shapefile. We performed this on every stage from Messinian back to the Cambrian. For the Cambrian, due to issues with the chronostratigraphy, we exported data at a series level instead. We also grouped the Piacenzian and Zanclean into a single mask for the Pliocene. These shapefiles were then imported into *GPlates*, and for each stage a set of polygons were (hand/mouse) drawn around the fossils, that connected their distributions with the open ocean (files representing this step of the process are in the supplementary material).

There are a number of limitations and caveats in this approach. Firstly, there is a temporal and spatial sampling bias, due to the preservation of suitable rocks through the Phanerozoic (Fig. 22). Secondly, while many fossil locations are found around either coastal areas (i.e. polygon edges) or river channels, a number of fossils are found in clusters further inland and consequently it is not always clear how these inland seas connected to the open ocean. In these cases, there is a degree of subjectivity in the decisions that we made, but in general we ensured that our polygons were constrained by the available data and were drawn as directly as possible to the nearest open ocean. Finally, some reconstructed fossils were not used as part of the

polygon drawing exercise, if they were isolated a long way from any other fossil or the edge of the continental crust.

2.5.2 Detrital zircon database

For the Neoproterozoic we use a recently compiled detrital zircon database (Puetz et al., 2024) that also contain depositional ages (~2000 entries) alongside data from the 'Sedimentary Geochemistry and Palaeoenvironments' Project (SGP) (28,000 entries) to constrain a maximum flooding surface. (Fig. 23). We similarly reconstruct data to their paleo-location at their time of deposition and use the resulting distribution to draw polygons representing flooding surfaces. Due the sparser spatio-temporal resolution of the data, the resulting polygons typically cover 20–30 Ma (i.e. this is the temporal resolution). We maintain some similar assumptions and limitations for this analysis as we did with the use of fossil data in the Phanerozoic. Our principal assumption is that the detrital zircons were being deposited in some basin that was connected to the open ocean, thus give some indication of eustatic sea level. We acknowledge that in the database we use some of the zircon data are undoubtably from fluvial or lacustrine settings and will not represent a marine environment, and future work could greatly improve this aspect of our model. As with the Phanerozoic fossil data, some data points are omitted if the zircon is isolated and in a continental interior. Secondly, we assume that the given age of deposition in the database of a zircon is an indicator of when the area was flooded.

2.5.3 Flooding the maps

Our final step once the polygons are constructed is to integrate them with our palaeogeographic maps. We do this using *pyGPlates*, where we read in both the modelled palaeogeographic netCDFs and the shapefiles containing the polygons. We perform a simple raster-cell in polygon check (i.e. the intersection between the two files, at each timestep), and for those cells that are within a mapped marine transgression we can then manually set their elevation. For this step, we opt to set all cells to -20 m (i.e. a shallow marine basin). This final step is done separately to the generated topographic maps, meaning that it can be quickly and easily reproduced using, for example, alternative flooding models. Or at much finer temporal resolution if one wanted to map changing sea level over (for example) 10^5-10^6 yr, thus allowing end users to reasonably easily generate alternative flooding histories at specific time steps over the last 1 Ga. The workflow to do this, including the unaltered maps, are included in the supplementary material, an example of the implemented changes is shown in Fig. 24.

3 Results and discussion

3.1. Present-day evaluation

In order to present an evaluation of our model we compare our results against present-day topography (ETOPO; Amante and Eakins, 2009). To do this, we provide our results ('modelled palaeotopography', Fig. 24b) at present-day in four different resolutions (Fig. 25, column 2); at a fine (0.1°, Fig. 25a), intermediate (1°, Fig. 25b) and coarse (2.5°, Fig. 25c) grid cell

resolution. We also show the present-day result where the topography is binned into 500 m bins (Fig. 25d). We then perform the same routine on the ETOPO data. To do this, we firstly use the same set of present-day nodes as in our modelling approach, and extract the mean ETOPO elevation of the node using all points within a 0.01° radius of the node (Fig. 25, column 1). We then grid the ETOPO-at-node data into the same 0.1°, 1°, 2.5° and binned to nearest 500 m, 1° rasters. We assess our model performance based on its difference with ETOPO ('residual topography'), shown both spatially (Fig 25, column 3) and as histograms (Fig 25, column 4).

There are several differences between our model prediction and present-day topography other than not fully representing flooded continental lithosphere at present-day (e.g. Sundaland, Zealandia). Our model overestimates are elevation, such as the Andean margin and North American Cordillera and along eastern Asia (e.g. Fig. 25d), and underestimates many cratonic interiors, in particular the Yilgarn craton in Australia and the North and South China cratons. We also underestimate much of the topography of central and southern Africa, and overestimate the sedimentary basins of northern Eurasia (e.g. West Siberian Basin). At higher resolutions (e.g. Fig. 25a, b) our model also shows smaller mismatches in continental interiors that are away from active tectonic environments (e.g. South America, eastern Europe). Due to the high degree of interdependency in topography-driven tectonic processes in our implemented workflow, it is difficult to assign specific causes for these regional mismatches. Additionally, as our model is a forward model (i.e. each timestep is explicitly dependent on the timestep before it), any changes to the implemented erosion and growth curves may have implications for global topography that are difficult to forecast. Below we discuss three processes that our model doesn't consider that could help bring further alignment between our model and presentday observation.

Our model does not explicitly include dynamic topography. Dynamic topography is a known contributor of elevation changes on the order of ~100s of m (Flament et al., 2013) due to changing density distributions in the mantle associated with mantle convection (Gurnis, 1990; Liu et al., 2008; Conrad and Husson, 2009; Flament et al., 2013). In areas where there is a negative mantle density anomaly, topography is lowered, and where there is a positive mantle density anomaly, topography is raised. Our model considers only an incomplete estimate of dynamic topography as through our inclusion of LIP-related topographic change (driven by the thermal expansion of the lithosphere in response to a plume). Importantly, we do not consider LIPs emplaced in oceanic lithosphere (e.g. Kerr, 2014), or more general upwellings like those that might occur underneath a supercontinent (Li and Zhong, 2009).

The erosion calculation we have implemented is non-dimensional and does not redistribute sediment that is eroded. The implications of this are that while we 'eroding' high relief regions, we are underestimating topography and bathymetry in non-mountainous regions where those eroded sediments may be deposited. This is likely particularly problematic in intracratonic regions and along passive margins. Furthermore, because we have no ongoing transport of sediments or fluvial network, continental interiors are much more 'flat' than what is otherwise suggested (their elevation is simply a function since last tectonic activity, rather than dynamic processes associated with erosion and transport of sediments) (Fox, 2019).

Finally, our model assumes that erosion is not controlled by climate, rather simply by relief. This is also demonstrably false, as, generally, highly weatherable and erodible regions exist around the equator and in the temperate belts, and less weatherable and erodible regions at high latitudes and in arid regions (Panagos et al., 2017). We initially attempted to scale our erosion calculation by latitude, however opted not to do this because we want to use these maps as input for landscape evolution models that use palaeoclimate data alongside a topography to determine erosion (e.g. GOSPL, Salles et al., 2020).

3.2 Evaluation through the Phanerozoic

We opt to compare our modelled results to those of Scotese and Wright (2018, hereafter PALEOMAP), whose palaeoDEMs (Digital Elevation Models) are widely used by palaeoclimate, palaeoceanography and landscape evolution community. Figures 26 and 27 shows our results at 50 Ma increments from 0 to 550 Ma, and Figure 28 summarises the hypsometry of our model and PALEOMAP. We focus our discussion predominantly on elevated regions, not flooded continental areas, as, in our model at least, this is a post-processing step and we envision that the community may prefer to use their own flooded continental polygons.

There are some differences between our modelled topography and PALEOMAP through the Phanerozoic. In the Palaeozoic, our model has a much higher eastern Gondwana, principally along the East African Orogen between India and Africa, and into Antarctica, as well as through the South America Gondwana-forming orogens (the Brasiliano orogens) between Amazonia and Africa. These elevated regions linger much longer in our model, persisting as an elevated regions (>4 km) until the Devonian. Likewise, many of the smaller orogenic belts that formed with Gondwana amalgamation (e.g. Damara Belt between Congo and Kalahari, Pharusian belt between West Africa Craton and Sahara) tend to linger at higher elevations in our model than in PALEOMAP through the early Palaeozoic. This is likely for two reasons, firstly our underlaying plate model has a final formation of Gondwana in the Cambrian (while PALEOMAP has it is in the Ediacaran), meaning many of our mountain ranges are slightly younger (and therefore have elevated regions until later). This timing is strongly supported by geological data (Collins and Pisarevsky, 2005; Fritz et al., 2013; Schmitt et al., 2018). Secondly, our erosion curve has an inflexion point at ~2000 m elevation, meaning that once things erode to this elevation their erosion rate slows considerably, thus maintain some considerable elevation on 10–100 Ma timescales after they form. The latest Ediacaran to Cambrian elevation of the East African Orogen (in particular) is likely to be underestimated in our model, based on estimates of the elevation from the metamorphic record (Collins et al., 2022) and from the detrital record of its erosion (Zhu et al., 2022). Our model, relative to PALEOMAP, also depicts lower elevation in some areas of northern Africa, principally parts of the West African Craton and the Sahara Metacraton. This is likely because in our underlying plate model both these areas have no interior plate margins so our model doesn't consider them as tectonically active.

As our model progresses into the late Palaeozoic (Devonian onwards) there are two main differences compared to PALEOMAP. Firstly, our modelled Gondwana orogens remain as elevated regions, while in PALEOMAP by the Devonian only the northern East African Orogen (around Arabia) and the Brasiliano orogens remain elevated. In PALEOMAP, the central and southern East African Orogen (Kenya, Madagascar), and the Lufillian-Zambezi belts are mostly eroded by this time (down to <500 m elevation). Similarly, most of Antarctica in PALEOMAP is reasonably flat. For our model, the long-lived Terra-Australis subduction zone outboard of Gondwana (from South America through to Australia) results in the establishment of a reasonably highly elevated continental arc across this margin. In some places, where the subduction is offshore, we have relatively low and flat topography, but in some cases such as north-west Amazonia, we maintain a reasonably high (>2 km) topography throughout the Devonian and Carboniferous. Finally, many of the small terranes that presently make up the Central Asian Orogenic Belt and Kazakhstan-Mongolia are much more elevated in our model than in PALEOMAP, because of their ongoing association with subduction zones in the underlaying plate model.

The topography arising from the amalgamation of Pangea is reasonably similar in both models, with some minor differences. In our model the Variscan mountain range is more discontinuous, and less linear than in PALEOMAP (e.g. Fig. 27a). Similarly to the Gondwana forming orogenies, the Pangea-forming orogenies in our model persist at a high elevation for longer than what is in PALEOMAP, maintaining elevations of greater than 1500 m for 100 Ma. During the late Palaeozoic and into the Mesozoic, our model has a more established and high elevation Andean margin along South America compared to PALEOMAP. Comparably, in our model Antarctica has no real topography during most of the late Palaeozoic and Mesozoic, with the Gondwana sutures having eroded down to < 500 m by this time. Only in the Jurassic and Cretaceous does eastern Antarctica develop a continental-arc associated mountain range. In comparison, PALEOMAP during the Mesozoic has an elevated plateau over much of Antarctica (>1500 m elevation).

For much of the Mesozoic our model depicts a more highly elevated Baltica-Siberia than PALEOMAP. In our model this elevation is driven by the topographic effect of the emplacement of two LIPs: the Doha and Siberian Traps. This associated elevation change is not reflected in the PALEOMAP model, and in our model persists until the Cretaceous. For the Cenozoic, much of the PALEOMAP topography is reminiscent of the present-day ETOPO (except for the Himalaya).

To better summarise some of these gross changes, we calculated the hypsometry of both our model and the PALEOMAP model over the Phanerozoic. We limit our hypsometry to just the terrestrial realm (land above 0.001 m), as PALEOMAP only contains simple bathymetry. We also calculate the present-day terrestrial hypsometry from ETOPO (Fig. 28) and plot it as a reference, though we note that modern hypsometry isn't prescriptive of past elevation. While there are some gross differences between both models, their trend and distribution are reasonably consistent, to a first order, with what we observe at present-day (Fig. 28c). Our model, in general, slightly underestimates topography relative to the present-day during the

Cenozoic at all elevations, though this may be a function of the presence of the Himalaya at present-day. Comparably, PALEOMAP also underestimates highly elevated regions during the Cenozoic, but has a reasonable match for elevations <1000 m. In the Mesozoic, both our model and PALEOMAP produce a similar hypsometry for regions above 300 m, though our model underestimates topography in lowland regions compared to PALEOMAP. During the Palaeozoic there is more similarity between both PALEOMAP and our model, except for elevations around sea-level (<100 m). We consider that our reasonably consistent underestimation of elevated land between 1 and 400 m relative to PALEOMAP is because our erosion model doesn't redistribute eroded sediment and the tectonic processes that we use to drive our topography occur in tectonically active regions, rather than passive regions, where processes like isostasy and lithospheric strength are more important.

3.3 Neoproterozoic

There are no extensive palaeotopographic models of the Neoproterozoic with which we can compare our work. Previous climate modelling either used no topographic model (i.e. fixed elevations over the entire globe (Hyde et al., 2000)) or simple, stylistic topography draped over a palaeocontinental model (Donnadieu et al., 2003). Figure 29 shows our map view results from the Neoproterozoic at set time intervals, and Figure 30 shows the hypsometry at the same times. Like the Phanerozoic, our method in the Neoproterozoic also struggles to represent low elevation (<1000 m) areas for the same reasons discussed above. An additional factor, however, for the earlier times are that our starting condition is a mostly flat Earth, with existing topography in the early Tonian being limited to the Grenvillian orogeny, and where active subduction zones are between 1000 and 970 Ma. This is evident in our hypsometry, where, in particular, the Tonian the majority of Earth's surface is modelled to be much lower elevation than what we see at present-day.

4 Preindustrial climate modelling comparison?

To demonstrate the use of our modelled present-day topography, we ran a series of four palaeoclimate simulations to compare it against the present-day ETOPO using two different climate models (PlaSIM-GENIE and HadCM3). PlaSIM-GENIE (Holden et al., 2016, 2018; Leonard et al., 2025) is an intermediate complexity climate model run at a gridcell resolution of 5.625°•5.625°, while HadCM3 (Gordon et al., 2000; Valdes et al., 2017) is a high complexity climate model run at a gridcell resolution of 2.5°•3.75° (latitude by longitude). To demonstrate the variation from a climate model that is driven solely by our estimate of topography, for each respective palaeoclimate model we use the ETOPO land-sea mask, bathymetry and ice-loaded topography as a base (i.e. HadCM3 ETOPO and PlaSIM-GENIE ETOPO). For the comparison runs we then draped our topography over the ETOPO land area. This preserved many present-day features that our model doesn't reproduce properly (e.g. a connected New Guinea with Australia, Zealandia). Model files are provided in the supplementary material, and we summarise the main contributions of all four runs to the chemical weathering cycle in Figure 31. Our discussion here focusses on the performance of the topography modelled through the workflow presented here relative to ETOPO, rather than to the observed Earth.

For the HadCM3 models, both the ETOPO and our modelled topography here produce broadly similar outputs. Global mean temperature is ~13.3–13.4 both runs, and the total silicate weathering flux is 0.42–0.43 Gt. There is more variation in the PLASIM-GENIE runs, with the 'default' ETOPO producing a global mean temperature of 13.8°C compared to 14.1°C in the MER25 topography. Chemical weathering is lower using our topography estimate (0.35 Gt) than ETOPO (0.4 Gt), seemingly because we do not resolve the Amazon drainage network as well as the ETOPO model does. Either way, our modelled topography in HadCM3 reproduces present-day erosion and weathering fluxes to a remarkable consistency with ETOPO. Our modelled topography with PLASIM-GENIE is more conservative than ETOPO, likely a reflection of the reduced complexity if PLASIM-GENIE, particularly in the land surface module. Our results indicate that our method can reproduce first order and correct erosion and weathering fluxes, which helps build some confidence in the use of our topographic estimates for deeper time climate-carbon models.

5. Conclusions

We present a set of full-Earth palaeotopographic and bathymetric maps from 1 Ga to present-day that describe how the evolution of Earth's surface has changed. We use an existing full-plate model that reconstructs the locations of both continents and plate boundaries back through time as our basis. Our analysis predominantly identifies continental arc and continental collision environments through time, though also traces rifts and emplacement of LIPs. It successfully reconstructs both the East African Orogen and the Himalaya as highly elevated plateaus as a consequence of continental collision, as well as major arc systems such as the Andes, Terra Australis, Variscan and Tethyan. Our model is similar to existing Phanerozoic topographic models (e.g. PALEOMAP), though underestimates low lying (> 1 km) topography. We consider that this is likely because our method only accounts for active tectonic uplift and does not consider either uplift from processes such as dynamic topography, nor does our implementation of erosion redistribute sediments. Our model is a forward model, the modelled topography at any one time is directly dependent on the preceding time-step and is directly depending on the underlaying plate tectonic model. In this way we couple a progressive evolution of surface topography to plate tectonic kinematics.

6. References

- Amante, C., and Eakins, B.W., 2009, ETOPO1 arc-minute global relief model: procedures, data sources and analysis:, https://repository.library.noaa.gov/view/noaa/1163.
- Barnhart, K.R., Hutton, E.W., Tucker, G.E., Gasparini, N.M., Istanbulluoglu, E., Hobley, D.E., and Bandaragoda, 2020, Landlab v2. 0: A software package for Earth surface dynamics: Earth Surface Dynamics, v. 8, p. 379–397.

- Besse, J., and Courtillot, V., 2002, Apparent and true polar wander and the geometry of the geomagnetic field over the last 200 Myr: Journal of geophysical research, v. 107, p. EPM 6-1-EPM 6-31.
- Blakey, R.C., 2008, Gondwana paleogeography from assembly to breakup—A 500 m.y. odyssey, *in* Special Paper 441: Resolving the Late Paleozoic Ice Age in Time and Space, Geological Society of America, v. 441, p. 1–28.
- Boschman, L.M., 2021, Andean mountain building since the Late Cretaceous: A paleoelevation reconstruction: Earth-Science Reviews, v. 220, p. 103640.
- Cao, X., Collins, A.S., Pisarevsky, S., Flament, N., Li, S., Hasterok, D., and Müller, R.D., 2024, Earth's tectonic and plate boundary evolution over 1.8 billion years: Geoscience frontiers, v. 15, p. 101922.
- Cao, W., Zahirovic, S., Flament, N., Williams, S., Golonka, J., and Müller, R.D., 2017, Improving global paleogeography since the late Paleozoic using paleobiology: Biogeosciences discussions, p. 1–24.
- Cermeño, P., García-Comas, C., Pohl, A., Williams, S., Benton, M.J., Chaudhary, C., Le Gland, G., Müller, R.D., Ridgwell, A., and Vallina, S.M., 2022, Post-extinction recovery of the Phanerozoic oceans and biodiversity hotspots: Nature, v. 607, p. 507–511.
- Collins, A., Cameron, F., Blades, M., Hasterok, D., Simpson, A., Gilbert, S., Clark, C., and Makin, S., 2022, Size is everything: reconstructing the East African Orogen—a Gondwanan supermountain—as a critical step to modelling the Neoproterozoic earth system, *in* Goldschmidt2022 abstracts, France, European Association of Geochemistry, doi:10.46427/gold2022.9391.
- Collins, A.S., and Pisarevsky, S.A., 2005, Amalgamating eastern Gondwana: The evolution of the Circum-Indian Orogens: Earth-Science Reviews, v. 71, p. 229–270.
- Conrad, C., and Husson, L., 2009, Influence of dynamic topography on sea level and its rate of change: Lithosphere, v. 1, p. 110–120.
- Crosby, A.G., and McKenzie, D., 2009, An analysis of young ocean depth, gravity and global residual topography: Geophysical journal international, v. 178, p. 1198–1219.
- Domeier, M., and Torsvik, T.H., 2017, Full-plate modelling in pre-Jurassic time: Geological magazine, p. 1–20.
- Donnadieu, Y., Fluteau, F., Ramstein, G., Ritz, C., and Besse, J., 2003, Is there a conflict between the Neoproterozoic glacial deposits and the snowball Earth interpretation: an improved understanding with numerical modeling: Earth and planetary science letters, v. 208, p. 101–112.

- England, P., and Molnar, P., 1990, Surface uplift, uplift of rocks, and exhumation of rocks: Geology, v. 18, p. 1173–1177.
- Evans, D.A.D. et al., 2021, Chapter 19 An expanding list of reliable paleomagnetic poles for Precambrian tectonic reconstructions, *in* Pesonen, L.J., Salminen, J., Elming, S.-Å., Evans, D.A.D., and Veikkolainen, T. eds., Ancient Supercontinents and the Paleogeography of Earth, Elsevier, p. 605–639.
- Flament, N., Gurnis, M., and Müller, R., 2013, A review of observations and models of dynamic topography: Lithosphere, v. 5, p. 189–210.
- Fluteau, F., Tardif, D., Sarr, A.-C., Le Hir, G., and Donnadieu, Y., 2023, Orogenesis and Climate: Himalaya: Dynamics of a Giant, Current Activity of the Himalayan Range, v. 3, p. 1.
- Fox, M., 2019, A linear inverse method to reconstruct paleo-topography: Geomorphology (Amsterdam, Netherlands), v. 337, p. 151–164.
- Fritz, H. et al., 2013, Orogen styles in the East African Orogen: A review of the Neoproterozoic to Cambrian tectonic evolution: Journal of African Earth Sciences, v. 86, p. 65–106.
- Goddéris, Y., Donnadieu, Y., Le Hir, G., Lefebvre, V., and Nardin, E., 2014, The role of palaeogeography in the Phanerozoic history of atmospheric CO2 and climate: Earth-Science Reviews, v. 128, p. 122–138.
- Goddéris, Y., Donnadieu, Y., Lefebvre, V., Le Hir, G., and Nardin, E., 2012, Tectonic control of continental weathering, atmospheric CO2, and climate over Phanerozoic times: Comptes rendus: Geoscience, v. 344, p. 652–662.
- Golonka, J., 2007, Phanerozoic paleoenvironment and paleolithofacies maps: late Palezoic: Akademia Gorniczo-Hutnicza im. Stanislawa Staszica. Geologia. Kwartalnik, p. 145–209.
- Golonka, J., Krobicki, M., Pajak, J., Van Giang, N., and Zuchiewicz, W., 2006, Global plate tectonics and paleogeography of Southeast Asia: Faculty of Geology, Geophysics and Environmental Protection, AGH University of Science and Technology, Arkadia, Krakow,

 Poland, https://scholar.google.com.au/citations?user=4T3bSDQAAAAJ&hl=en&oi=sra.
- Gordon, C., Cooper, C., Senior, C.A., Banks, H., Gregory, J.M., Johns, T.C., Mitchell, J.F.B., and Wood, R.A., 2000, The simulation of SST, sea ice extents and ocean heat transports in a version of the Hadley Centre coupled model without flux adjustments: Climate dynamics, v. 16, p. 147–168.
- Gurnis, M., 1990, Bounds on global dynamic topography from Phanerozoic flooding of continental platforms: Nature, v. 344, p. 754–756.

- Gurnis, M., Turner, M., Zahirovic, S., DiCaprio, L., Spasojevic, S., Müller, R.D., Boyden, J., Seton, M., Manea, V.C., and Bower, D.J., 2012, Plate tectonic reconstructions with continuously closing plates: Computers & geosciences, v. 38, p. 35–42.
- Hasterok, D., Halpin, J.A., Collins, A.S., and Hand, M., 2022, New maps of global geological provinces and tectonic plates: Earth-Science Reviews, https://www.sciencedirect.com/science/article/pii/S0012825222001532.
- Holden, P.B. et al., 2018, Climate–carbon cycle uncertainties and the Paris Agreement: Nature climate change, v. 8, p. 609–613.
- Holden, P.B., Edwards, N.R., Fraedrich, K., Kirk, E., Lunkeit, F., and Zhu, X., 2016, PLASIM–GENIE v1. 0: a new intermediate complexity AOGCM: Geoscientific Model Development, v. 9, p. 3347–3361.
- Hyde, W.T., Crowley, T., Baum, S., and Peltier, W., 2000, Neoproterozoic 'snowball Earth' simulations with a coupled climate/ice-sheet model: Nature, v. 405, p. 425–429.
- Karlsen, K.S., Domeier, M., Gaina, C., and Conrad, C.P., 2020, A tracer-based algorithm for automatic generation of seafloor age grids from plate tectonic reconstructions:

 Computers

 & geosciences,

 https://www.sciencedirect.com/science/article/pii/S0098300419308325.
- Kerr, A.C., 2014, Oceanic Plateaus 6: Structure (London, England: 1993), https://www.researchgate.net/profile/Andrew-Kerr-11/publication/257307772_Oceanic_Plateaus/links/0c960524dddd8a2a02000000/Oceanic-Plateaus.pdf.
- Leonard, J., Zahirovic, S., Holden, P.B., Salles, T., Edwards, N.R., and Mallard, C.A., 2025, Polar wander leads to large differences in past climate reconstructions: Communications earth & environment, v. 6, p. 508.
- Li, Z.X. et al., 2008, Assembly, configuration, and break-up history of Rodinia: A synthesis: Precambrian research, v. 160, p. 179–210.
- Liu, L., Spasojevic, S., and Gurnis, M., 2008, Reconstructing Farallon plate subduction beneath North America back to the Late Cretaceous: Science, v. 322, p. 934–938.
- Liu, B., Williams, S., Seton, M., and Zhao, G., 2024, Mapping paleoelevations along active continental margins with igneous geochemistry: A case study from South America: Gondwana research: international geoscience journal, v. 134, p. 285–297.
- Marcilly, C.M., Maffre, P., Le Hir, G., Pohl, A., Fluteau, F., Goddéris, Y., Donnadieu, Y., H. Heimdal, T., and Torsvik, T.H., 2022a, Understanding the early Paleozoic carbon cycle balance and climate change from modelling: Earth and planetary science letters, v. 594, p. 117717.

- Marcilly, C.M., Torsvik, T.H., and Conrad, C.P., 2022b, Global Phanerozoic sea levels from paleogeographic flooding maps: Gondwana Research, doi:10.1016/j.gr.2022.05.011.
- Marcilly, C.M., Torsvik, T.H., Domeier, M., and Royer, D.L., 2021, New paleogeographic and degassing parameters for long-term carbon cycle models: Gondwana Research, v. 97, p. 176–203.
- Markwick, P.J., and Valdes, P.J., 2004, Palaeo-digital elevation models for use as boundary conditions in coupled ocean–atmosphere GCM experiments: a Maastrichtian (late Cretaceous) example: Palaeogeography, palaeoclimatology, palaeoecology, v. 213, p. 37–63.
- Mather, B.R. et al., 2024, Deep time spatio-temporal data analysis using pyGPlates with PlateTectonicTools and GPlately: Geoscience data journal, v. 11, p. 3–10.
- Merdith, A.S. et al., 2017, A full-plate global reconstruction of the Neoproterozoic: Gondwana Research, v. 50, p. 84–134.
- Merdith, A.S. et al., 2021, Extending full-plate tectonic models into deep time: Linking the Neoproterozoic and the Phanerozoic: Earth-Science Reviews, v. 214, p. 103477.
- Merdith, A.S., Atkins, S.E., and Tetley, M.G., 2019, Tectonic Controls on Carbon and Serpentinite Storage in Subducted Upper Oceanic Lithosphere for the Past 320 Ma: Frontiers of Earth Science in China, v. 7, p. 332.
- Mills, B.J.W., Donnadieu, Y., and Goddéris, Y., 2021, Spatial continuous integration of Phanerozoic global biogeochemistry and climate: Gondwana Research, doi:10.1016/j.gr.2021.02.011.
- Mitchell, R.N., Kilian, T.M., and Evans, D.A.D., 2012, Supercontinent cycles and the calculation of absolute palaeolongitude in deep time: Nature, v. 482, p. 208–211.
- Montgomery, D.R., and Brandon, M.T., 2002, Topographic controls on erosion rates in tectonically active mountain ranges: Earth and planetary science letters, v. 201, p. 481–489.
- Moores, E.M., 1991, Southwest U.S.-East Antarctic (SWEAT) connection: A hypothesis: Geology, v. 19, p. 425–428.
- Müller, R.D., Cannon, J., Qin, X., Watson, R.J., Gurnis, M., Williams, S., Pfaffelmoser, T., Seton, M., Russell, S.H.J., and Zahirovic, S., 2018, GPlates: Building a Virtual Earth Through Deep Time: Geochemistry, Geophysics, Geosystems, v. 19, p. 2243–2261.
- Müller, R.D., Cannon, J., Tetley, M., Williams, S.E., Cao, X., Flament, N., Bodur, Ö.F., Zahirovic, S., and Merdith, A., 2022, A tectonic-rules based mantle reference frame since 1 billion years ago--implications for supercontinent cycles and plate-mantle system evolution: Solid Earth Discussions, p. 1–42.

- Müller, R.D., Sdrolias, M., Gaina, C., and Roest, W.R., 2008, Age, spreading rates, and spreading asymmetry of the world's ocean crust: Geochemistry, Geophysics, Geosystems, v. 9, https://onlinelibrary.wiley.com/doi/abs/10.1029/2007GC001743.
- Panagos, P. et al., 2017, Global rainfall erosivity assessment based on high-temporal resolution rainfall records: Scientific reports, v. 7, doi:10.1038/s41598-017-04282-8.
- Park, Y., Swanson-Hysell, N.L., Lisiecki, L.E., and Macdonald, F.A., 2021, Evaluating the relationship between the area and latitude of large igneous provinces and earth's long-term climate state: Large Igneous Provinces, p. 153–168, doi:10.1002/9781119507444.ch7.
- Pehrsson, S.J., Eglington, B.M., Evans, D.A.D., Huston, D., and Reddy, S.M., 2016, Metallogeny and its link to orogenic style during the Nuna supercontinent cycle: Geological Society, London, Special Publications, v. 424, p. 83–94.
- Planavsky, N.J., McGoldrick, P., Scott, C.T., Li, C., Reinhard, C.T., Kelly, A.E., Chu, X., Bekker, A., Love, G.D., and Lyons, T.W., 2011, Widespread iron-rich conditions in the mid-Proterozoic ocean: Nature, v. 477, p. 448–451.
- Poblete, F. et al., 2021, Towards interactive global paleogeographic maps, new reconstructions at 60, 40 and 20 Ma: Earth-science reviews, v. 214, p. 103508.
- Pohl, A., Ridgwell, A., Stockey, R.G., Thomazo, C., Keane, A., Vennin, E., and Scotese, C.R., 2022, Continental configuration controls ocean oxygenation during the Phanerozoic: Nature, v. 608, p. 523–527.
- Puetz, S.J., Spencer, C.J., Condie, K.C., and Roberts, N.M.W., 2024, Enhanced U-Pb detrital zircon, Lu-Hf zircon, δ18O zircon, and Sm-Nd whole rock global databases: Scientific data, v. 11, p. 56.
- Rahmstorf, S., 2002, Ocean circulation and climate during the past 120,000 years: Nature, v. 419, p. 207–214.
- Rowley, D.B., and Currie, B.S., 2006, Palaeo-altimetry of the late Eocene to Miocene Lunpola basin, central Tibet: Nature, v. 439, p. 677–681.
- Salles, T., Husson, L., Rey, P., Mallard, C., Zahirovic, S., Boggiani, B.H., Coltice, N., and Arnould, M., 2023, Hundred million years of landscape dynamics from catchment to global scale: Science, v. 379, p. 918–923.
- Salles, T., Mallard, C., and Zahirovic, S., 2020, gospl: Global Scalable Paleo Landscape Evolution: Journal of open source software, v. 5, p. 2804.
- Saunders, A.D., Jones, S.M., Morgan, L.A., Pierce, K.L., Widdowson, M., and Xu, Y.G., 2007, Regional uplift associated with continental large igneous provinces: The roles of mantle plumes and the lithosphere: Chemical geology, v. 241, p. 282–318.

- Schmitt, R. da S., Fragoso, R. de A., and Collins, A.S., 2018, Suturing Gondwana in the Cambrian: The Orogenic Events of the Final Amalgamation, *in* Siegesmund, S., Basei, M.A.S., Oyhantçabal, P., and Oriolo, S. eds., Geology of Southwest Gondwana, Cham, Springer International Publishing, p. 411–432.
- Scotese, C.R., 2021, An Atlas of Phanerozoic Paleogeographic Maps: The Seas Come In and the Seas Go Out: Annual review of earth and planetary sciences, v. 49, p. 679–728.
- Scotese, C.R., 2001, Atlas of Earth History, vol 1, Paleogeography, Paleomap Project, Arlington, Texas, 52 pp:, https://scholar.google.com/citations?view_op=view_citation&hl=en&user=2Yb1IB0 AAAAJ&citation for view=2Yb1IB0AAAAJ:PVgj2kMGcgYC.
- Scotese, C.R., 2004, Cenozoic and Mesozoic paleogeography: changing terrestrial biogeographic pathways: Frontiers of biogeography: new directions in the geography of nature, p. 9–26.
- Scotese, C.R., Boucot, A.J., and McKerrow, W.S., 1999, Gondwanan palaeogeography and palloclimatology: Journal of African earth sciences (Oxford, England: 1994), v. 28, p. 99–114.
- Scotese, C.R., and McKerrow, W.S., 1990, Revised World maps and introduction: Geological Society London Memoirs, v. 12, p. 1–21.
- Scotese, and Wright, 2018, PALEOMAP paleodigital elevation models (PaleoDEMS) for the Phanerozoic: PALEOMAP Proj, https://www.earthbyte.org/webdav/ftp/Data_Collections/Scotese_Wright_2018_Paleo DEM/Scotese_Wright2018_PALEOMAP_PaleoDEMs.pdf.
- Seton, M., Williams, S.E., Domeier, M., Collins, A.S., and Sigloch, K., 2023, Deconstructing plate tectonic reconstructions: Nature Reviews Earth & Environment, p. 1–20.
- Sijp, W.P., von der Heydt, A.S., Dijkstra, H.A., Flögel, S., Douglas, P.M.J., and Bijl, P.K., 2014, The role of ocean gateways on cooling climate on long time scales: Global and planetary change, v. 119, p. 1–22.
- Stein, C.A., and Stein, S., 1992, A model for the global variation in oceanic depth and heat flow with lithospheric age: Nature, v. 359, p. 123–129.
- Torsvik, T.H. et al., 2012, Phanerozoic polar wander, palaeogeography and dynamics: Earth-Science Reviews, v. 114, p. 325–368.
- Torsvik, T.H., Burke, K., Steinberger, B., Webb, S.J., and Ashwal, L.D., 2010, Diamonds sampled by plumes from the core-mantle boundary: Nature, v. 466, p. 352–355.
- Torsvik, T.H., and Cocks, L.R.M., 2016, Earth History and Palaeogeography: Cambridge University Press, 329 p.

- Torsvik, T.H., Dietmar Muller, R., Van der Voo, R., Steinberger, B., and Gaina, C., 2008, Global Plate Motion Frames: Toward a Unified Model: Reviews of Geophysics, v. 46, doi:10.1029/2007RG000227.
- Uieda, L., Tian, D., Leong, W.J., Toney, L., and Schlitzer, W., 2021, PyGMT: A Python interface for the generic mapping tools:, https://gfzpublic.gfz-potsdam.de/pubman/faces/ViewItemFullPage.jsp?itemId=item_5005928_4.
- Vaes, B. et al., 2023, A global apparent polar wander path for the last 320 Ma calculated from site-level paleomagnetic data: , p. 104547.
- Valdes, P.J. et al., 2017, The BRIDGE HadCM3 family of climate models: HadCM3@Bristol v1.0: Geoscientific Model Development, v. 10, p. 3715–3743.
- Valdes, P.J., Scotese, C.R., and Lunt, D.J., 2021, Deep ocean temperatures through time: Climate of the Past, v. 17, p. 1483–1506.
- Vérard, C., 2021, 888–444 Ma global plate tectonic reconstruction with emphasis on the formation of Gondwana: Frontiers in earth science, v. 9, doi:10.3389/feart.2021.666153.
- Vérard, C., 2019a, Panalesis: towards global synthetic palaeogeographies using integration and coupling of manifold models: Geological magazine, v. 156, p. 320–330.
- Vérard, C., 2019b, Plate tectonic modelling: review and perspectives: Geological magazine, v. 156, p. 208–241.
- Vérard, C., Hochard, C., Baumgartner, P.O., Stampfli, G.M., and Liu, M., 2015, 3D palaeogeographic reconstructions of the Phanerozoic versus sea-level and Sr-ratio variations: Journal of Palaeogeography, v. 4, p. 64–84.
- Walker, J.C.G., Hays, P.B., and Kasting, J.F., 1981, A negative feedback mechanism for the long-term stabilization of Earth's surface temperature: Journal of geophysical research, v. 86, p. 9776.
- Willett, S.D., 1999, Orogeny and orography: The effects of erosion on the structure of mountain belts: Journal of geophysical research, v. 104, p. 28957–28981.
- Williams, S., Wright, N.M., Cannon, J., Flament, N., and Müller, R.D., 2021, Reconstructing seafloor age distributions in lost ocean basins: Geoscience Frontiers, v. 12, p. 769–780.
- Wu, L., Murphy, J., Quesada, C., Li, Z., Waldron, J., Williams, S., Pisarevsky, S., and Collins, W., 2020, The amalgamation of Pangea: Paleomagnetic and geological observations revisited: GSA Bulletin, v. 133, p. 625–646.

- Zahirovic, S., Eleish, A., Doss, S., Pall, J., Cannon, J., Pistone, M., Tetley, M.G., Young, A., and Fox, P., 2022, Subduction and carbonate platform interactions: Geoscience data journal, doi:10.1002/gdj3.146.
- Zhu, Z., Campbell, I.H., Allen, C.M., Brocks, J.J., and Chen, B., 2022, The temporal distribution of Earth's supermountains and their potential link to the rise of atmospheric oxygen and biological evolution: Earth and planetary science letters, v. 580, p. 117391.
- Ziegler, A., Rowley, D., Lottes, A., Sahagian, D., Hulver, M., and Gierlowski, T.C., 1985, Paleogeographic interpretation: With an example from the mid-cretaceous: Annual Review of Earth and Planetary Sciences, v. 13, p. 385–425.
- Ziegler, A.M., Scotese, C.R., McKerrow, W.S., Johnson, M.E., and Bambach, R.K., 1979, Paleozoic paleogeography: Annual review of earth and planetary sciences, v. 7, p. 473–502.

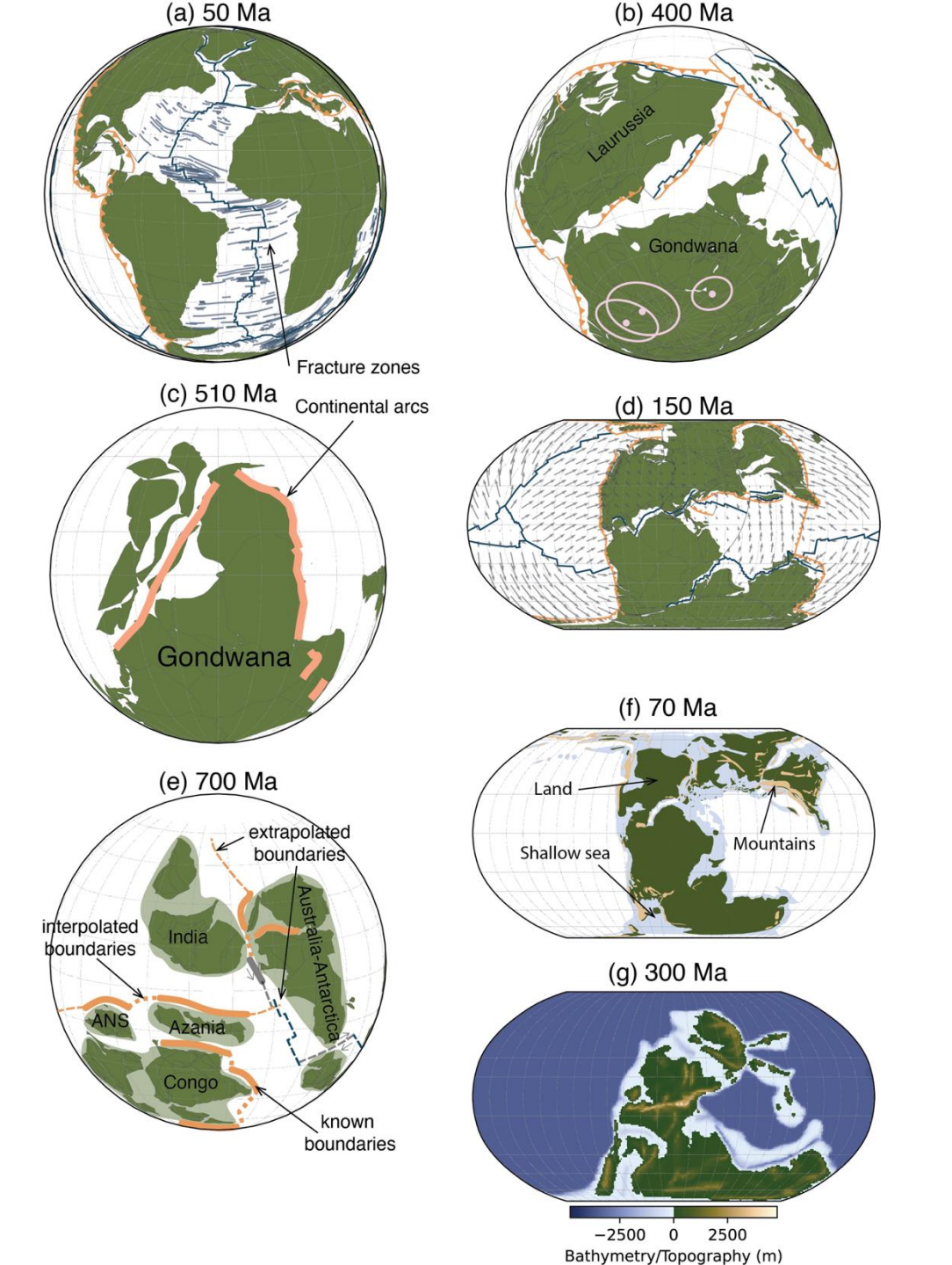


Figure 1: Examples of different types of described reconstructions (a) in text. Palaeocontinental reconstruction during Cenozoic (Müller et al. 2016) using fracture zones (Matthews et al. 2012) and (b) during the (Merdith et al. 2021) Palaeozoic palaeomagnetic data (Torsvik et al. 2012) for earlier times. (c) shows a palaeotectonic reconstruction, where locations of continental arcs plotted onto a palaeocontinental are reconstruction. (d) shows a full plate model, where all plate boundaries and tectonic plates are explicitly modelled (note, (a) and (b) are also fullplate models) (Müller et al. 2016). (e) shows how known plate boundaries can be extrapolated and interpolated into unknown regions (Merdith et al. 2017). (f) depicts a classic palaeogeographic reconstruction, with the Earth's surface broken up into different geographic regions (land, shallow sea and mountains) (Cao et al. 2019). (g) shows the most widely used palaeotopographic model of Scotese and Wright (2018).

(a) Continental Arc

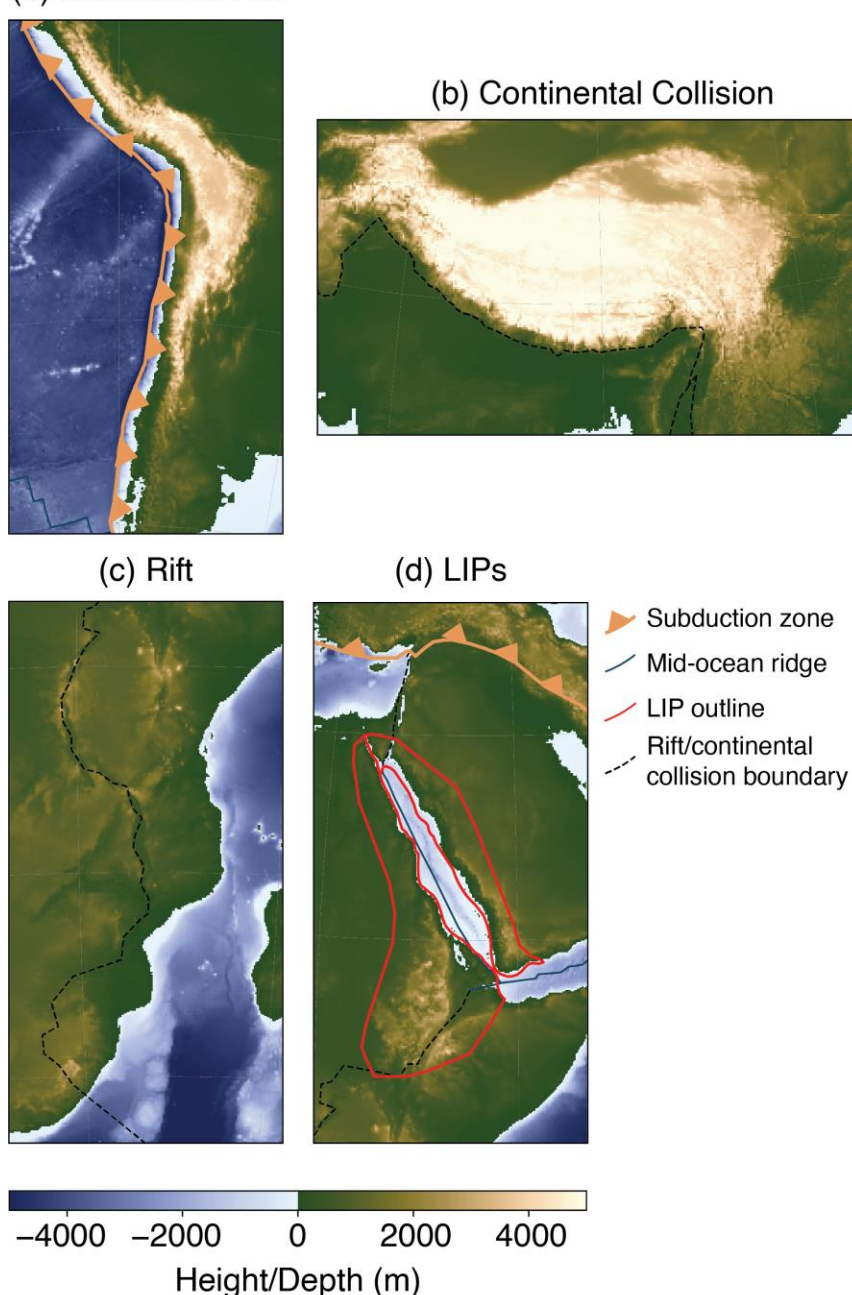


Figure 2: some present-day environments that cause topographic changes in Earth's surface. (a) the Himalaya representing large-scale continental collisions when India collided with Eurasia. (b) accretional margins, where over 100s Ma multiple small terranes and/or volcanic arcs collide and accrete to a continental margin (here the Rocky Mountains of North America). (c) A long-lived continental arc (the Andes of South America). (d) a continental arc that has formed on smaller extents (e) an oceanic arc (Lesser Antilles of the Caribbean). (f) a rift basin (Africa). (g) LIP emplacement (here the Ethiopian-Yemen LIP. (h) global ETOPO map.

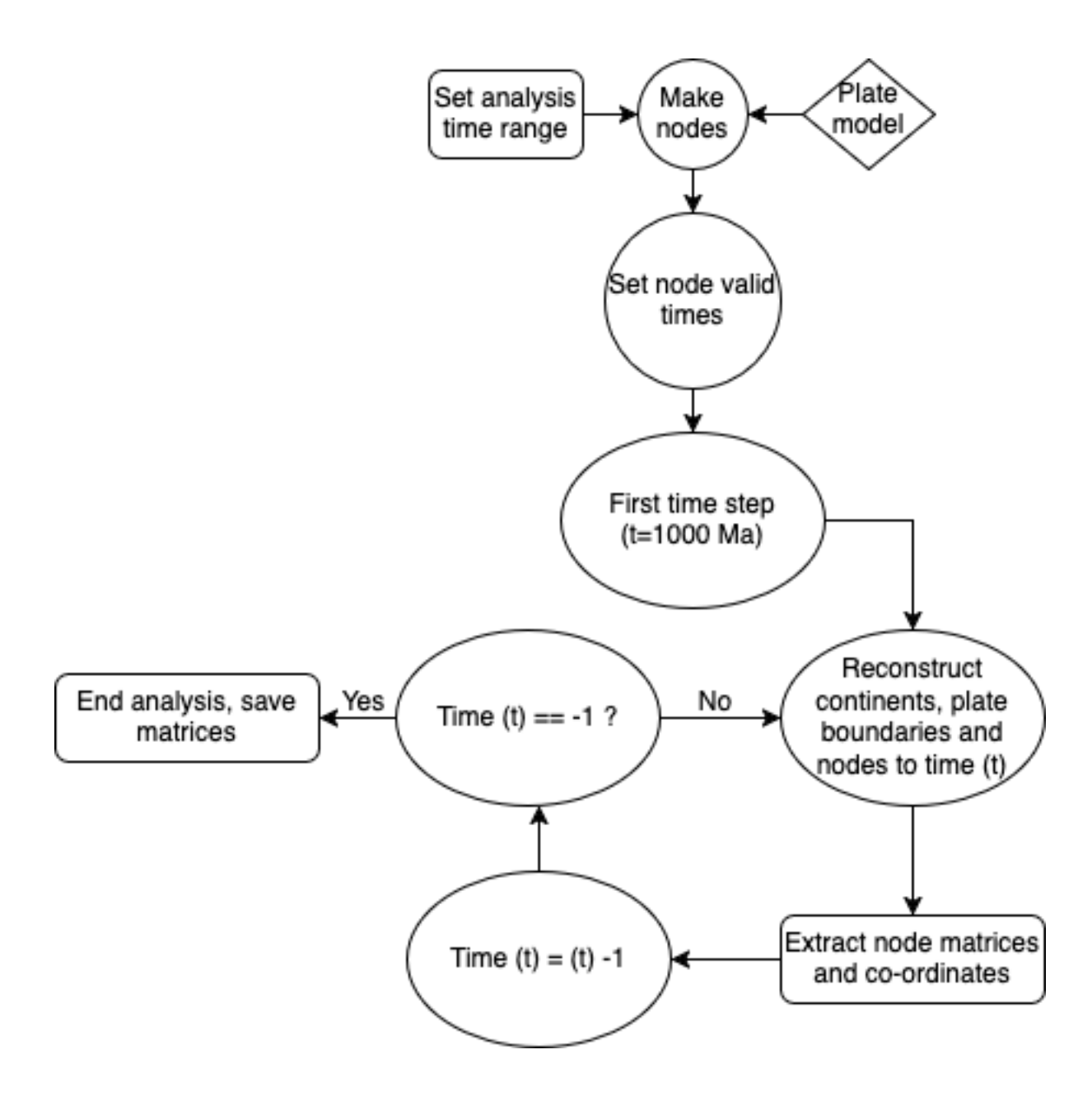
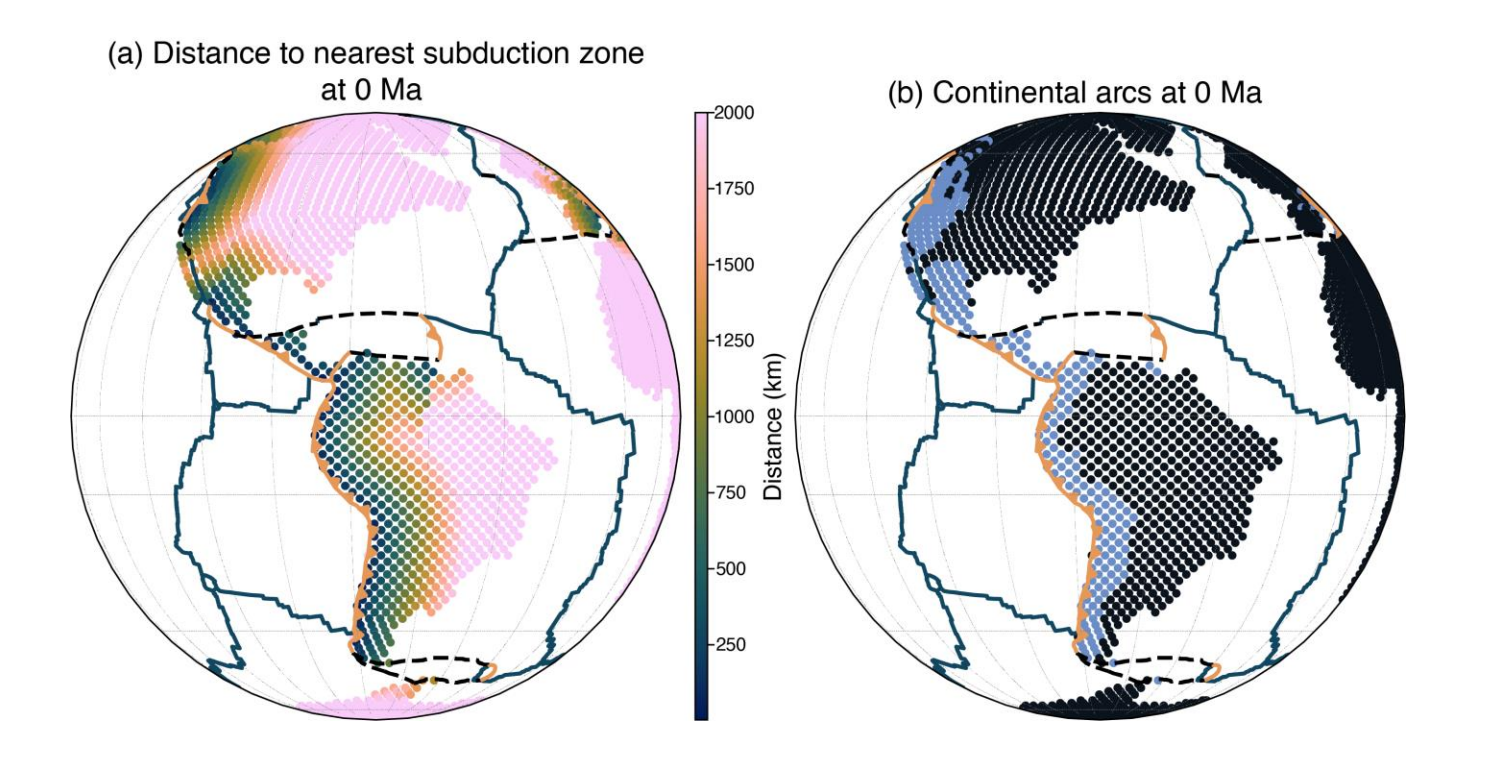


Figure 3: flowchart summarising the first phase of our methodology, extracting data matrices for each parameter at each node from the plate model.

Figure 4: Nodes at present-day, (a) whether they are considered in a continental arc environment (blue) or not (black) and (b) coloured by their distance to the nearest downgoing subduction zone.



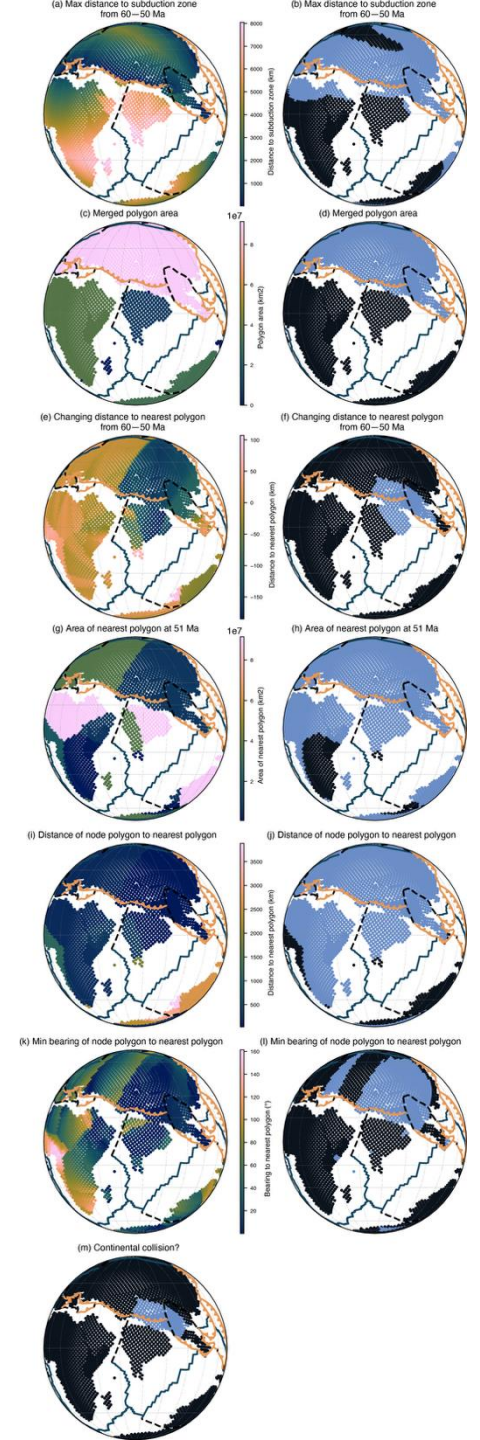


Figure 5: Map view of continental collision tests. The first column shoes the the 'base' criteria, such as area of polygon, distance to a subduction zone etc. The second column shows our implementation of that criterion as a function to isolate continental collision areas. In this second column, blue coloured nodes show where the criterion is met, black nodes show where it fails. Plotting is done at 50 Ma.

Figure 6: Nodes at 120 Ma depicting our equation to determine if an area could be in a rift zone. (a) change in distance between 121 and 120 Ma to the nearest ocean. (b) thresholded to 400 km distance from the incipient ocean basin. (see second option)

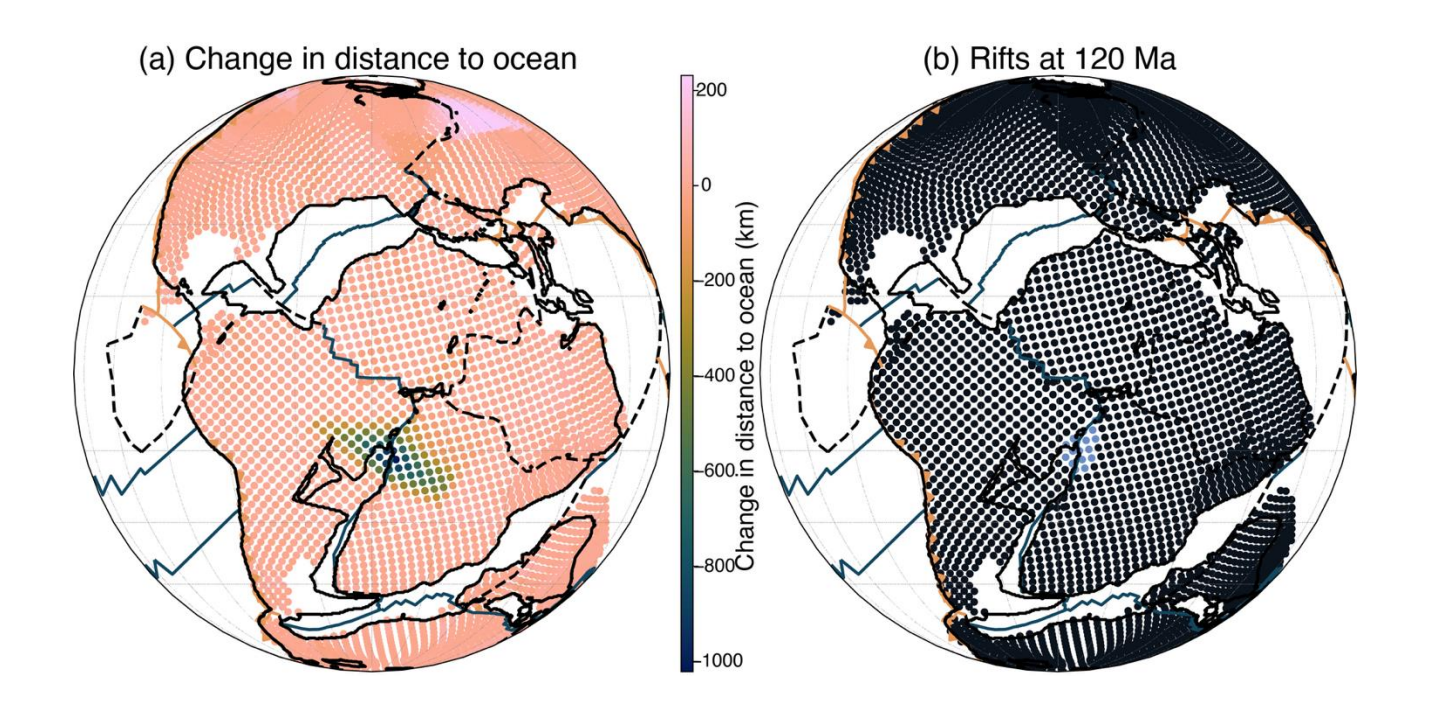
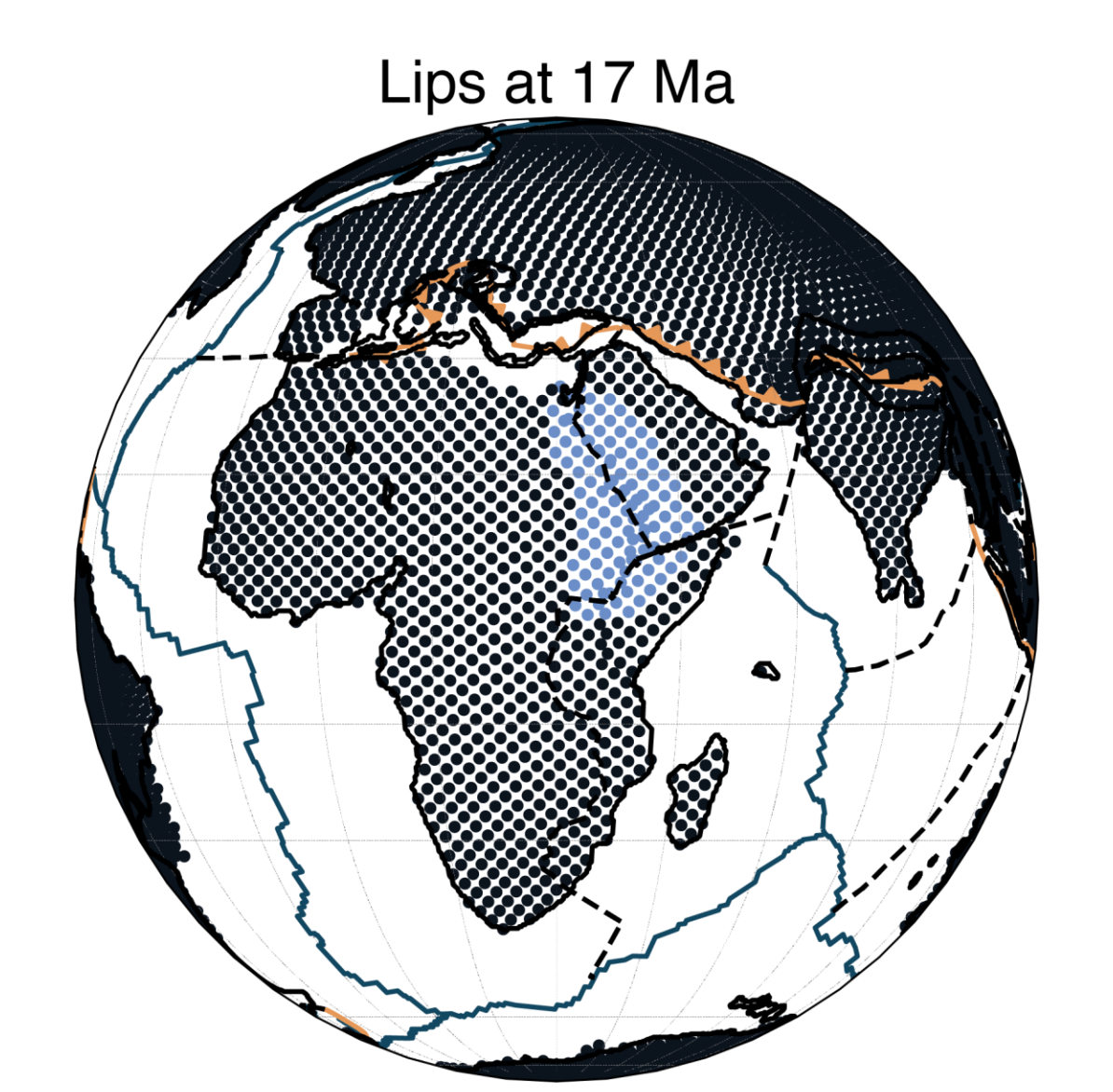


Figure 7: Nodes at 17 Ma depicting our equation to determine if an area is in a LIP. Highlighted in blue is the Afar LIP after Park et al. (2021). (see second option).



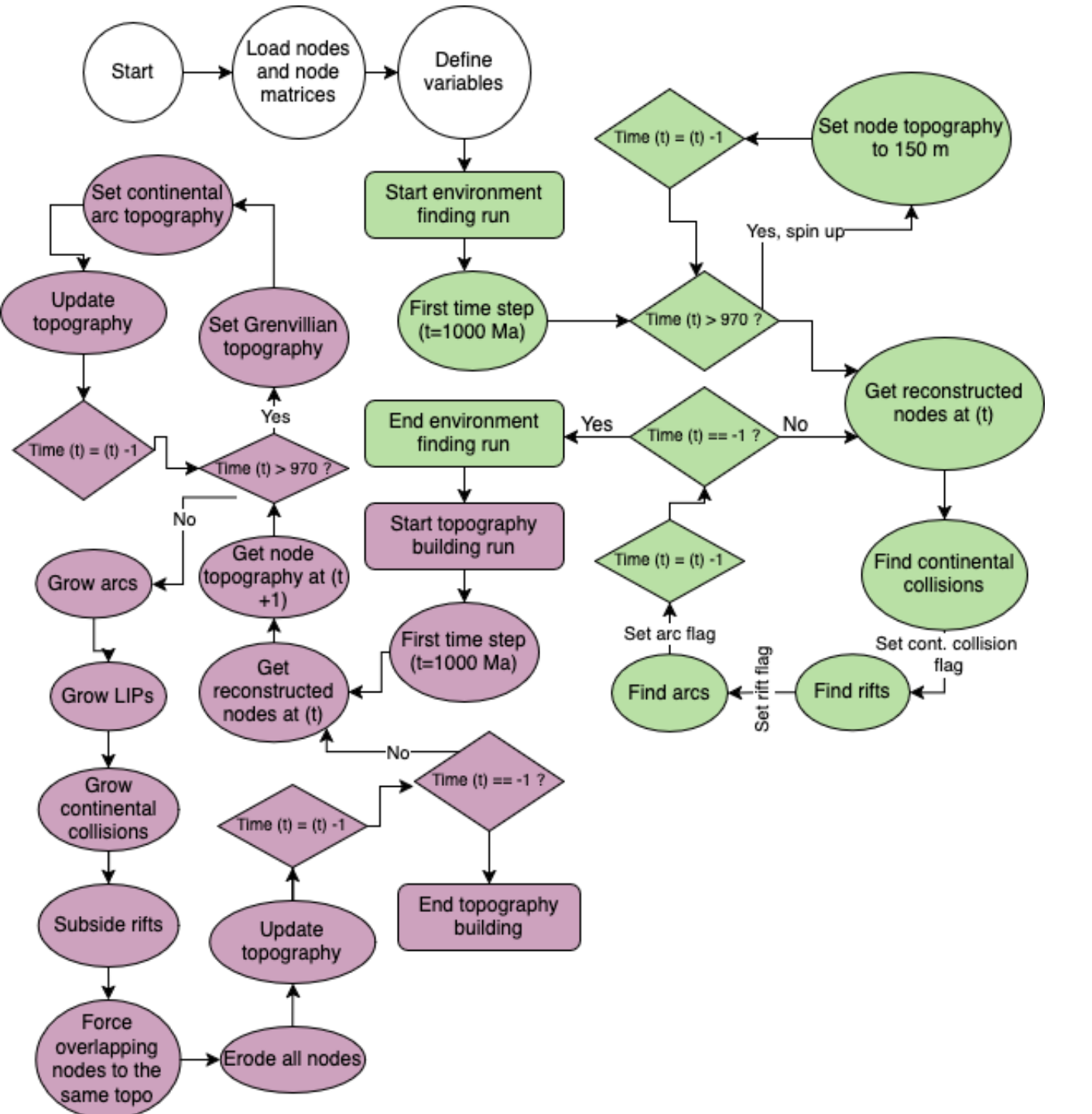


Figure 8: Flowchart depicting the sequence of events for how we build topography. Green shapes represent the first pass, where the different tectonic environments (continental collisions, rifts and arcs) are all identified for each node, and the purple shapes represents the sequence of events for modelling topographic growth and erosion at each time step.

Figure 9: Spin up topography, showing the Grenvillian orogeny (pink nodes on the right side of the map) and active continental arcs.

Spin up topography (at 970 Ma)

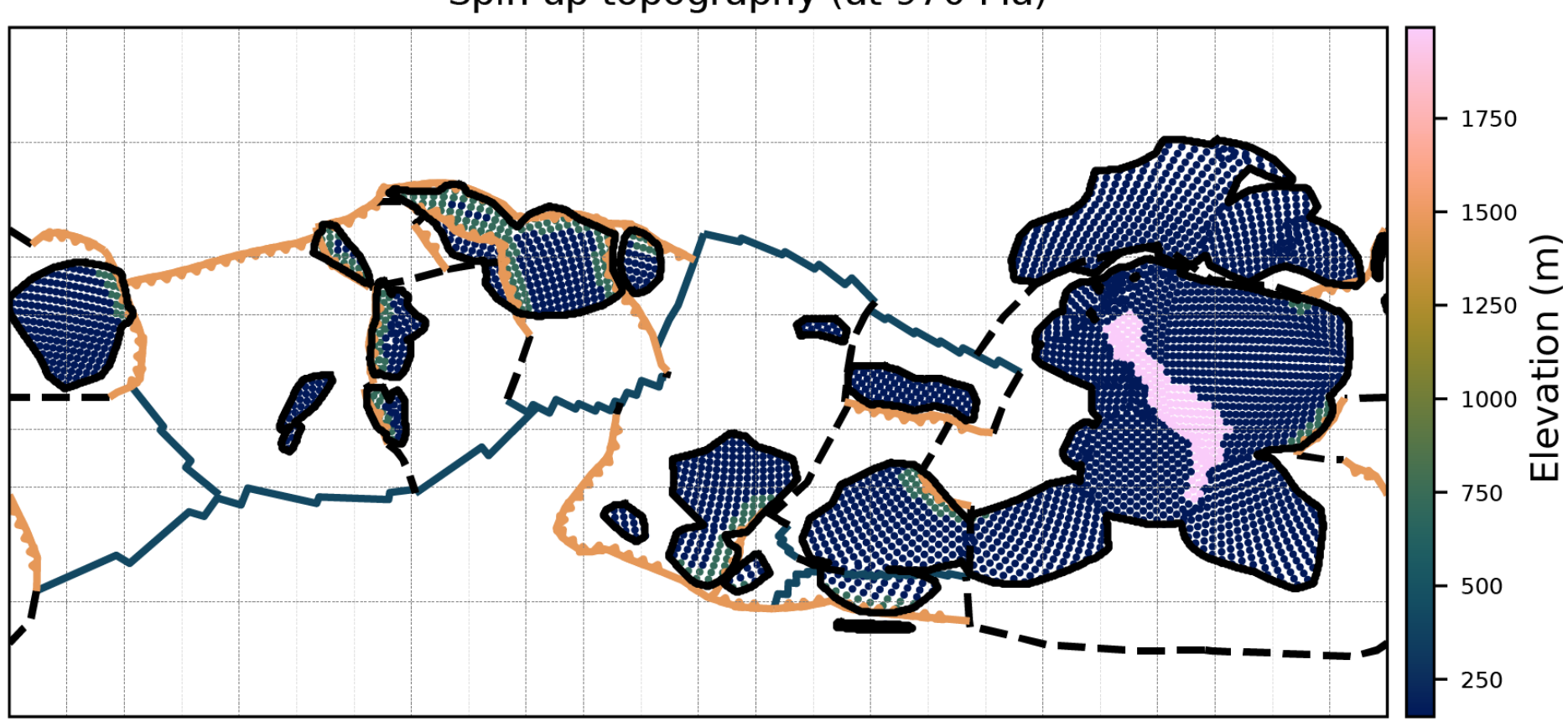
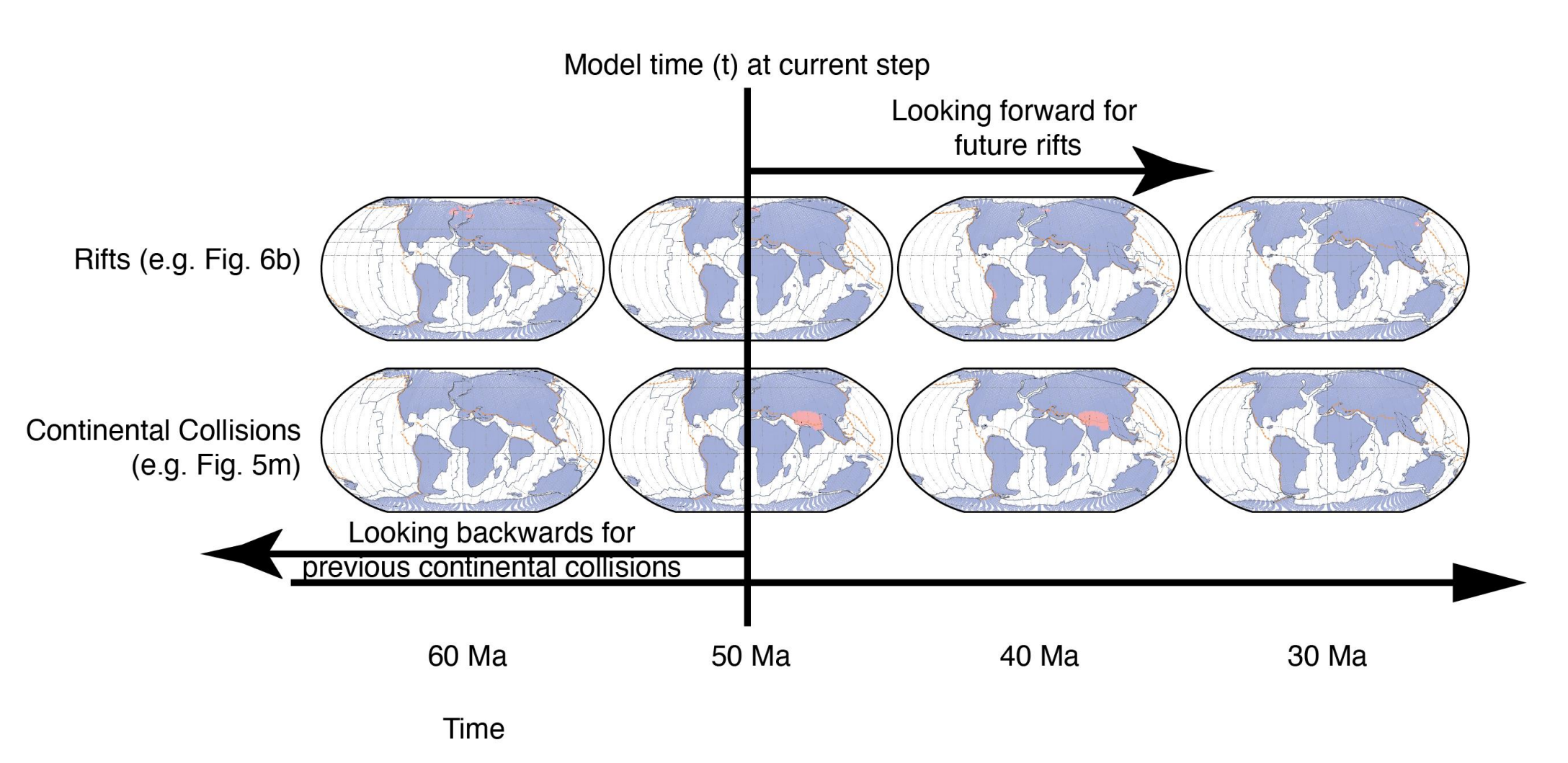


Figure 10: Run 1 creates a set of flags for rifts or continental collisions (i.e. the map views), these are used in run 2 (vertical line representing model time) to figure out if a node is in one of these environments or not.



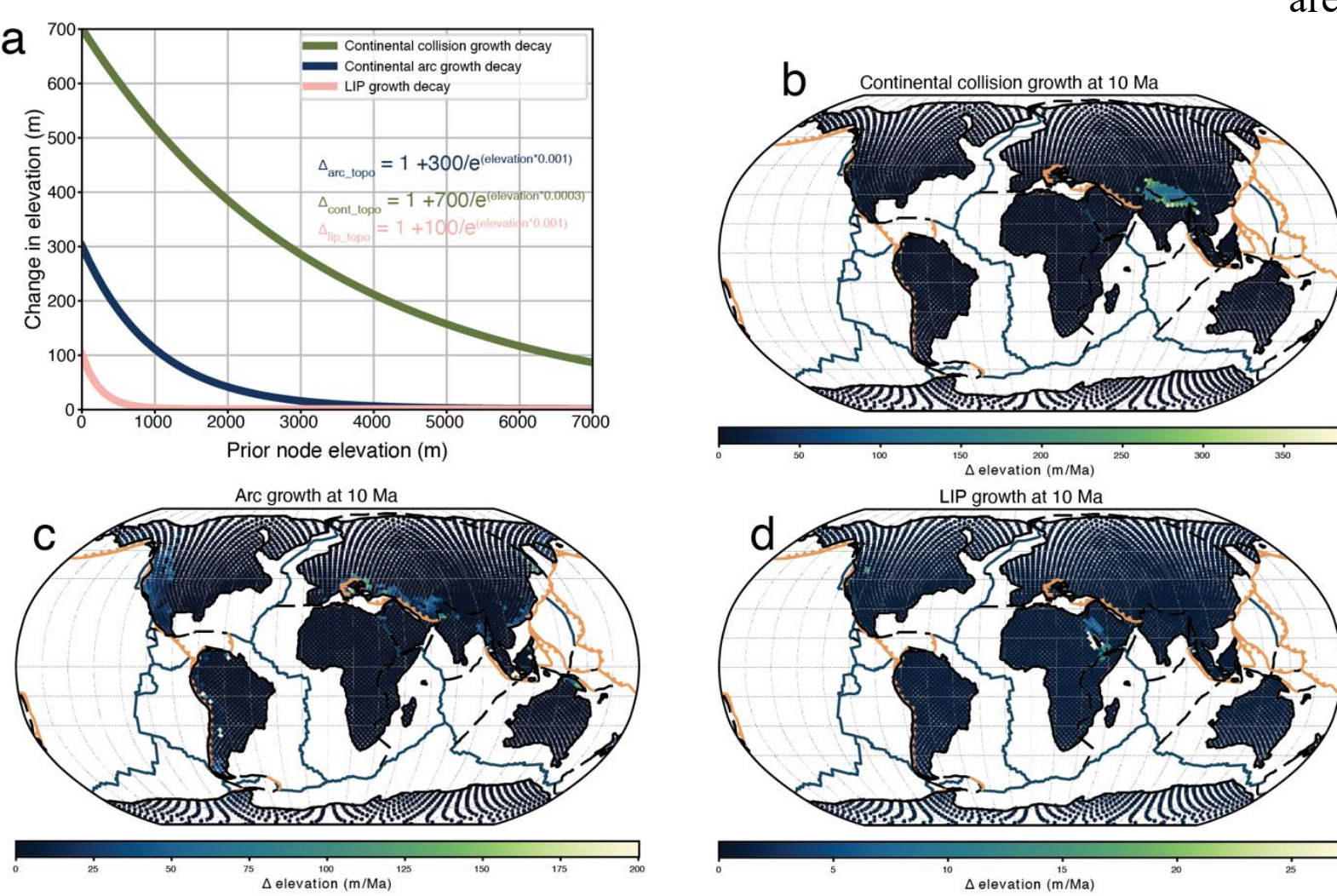


Figure 11. Topography growing parameters. (a) shows the equations we employ to 'grow' nodes that are determined to be within a specific environment. (b–d) each respective equation applied to the model at 10 Ma, showing growth in (b) continental collision areas, (c) continental arcs areas, and (d) LIP areas.

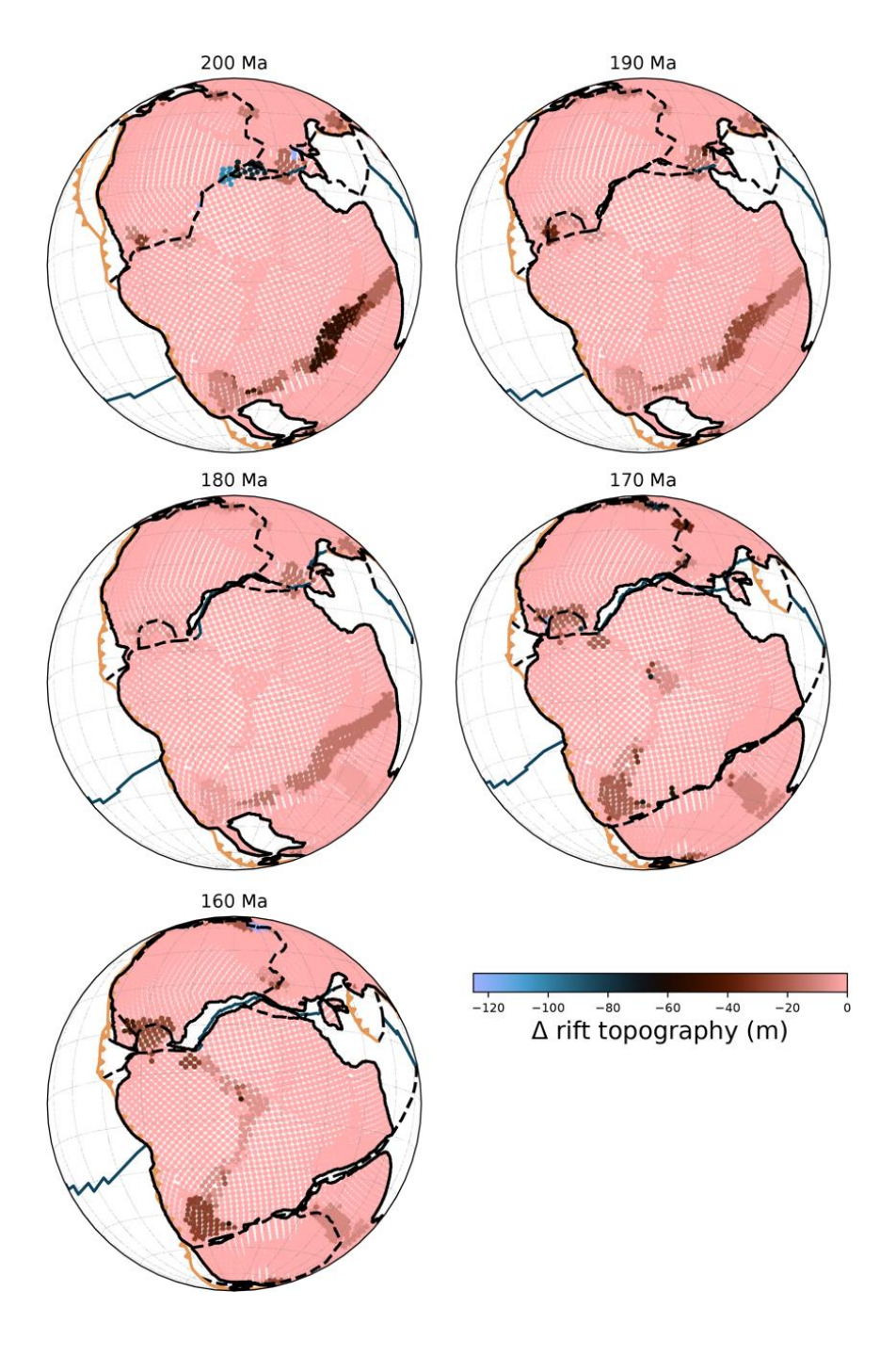
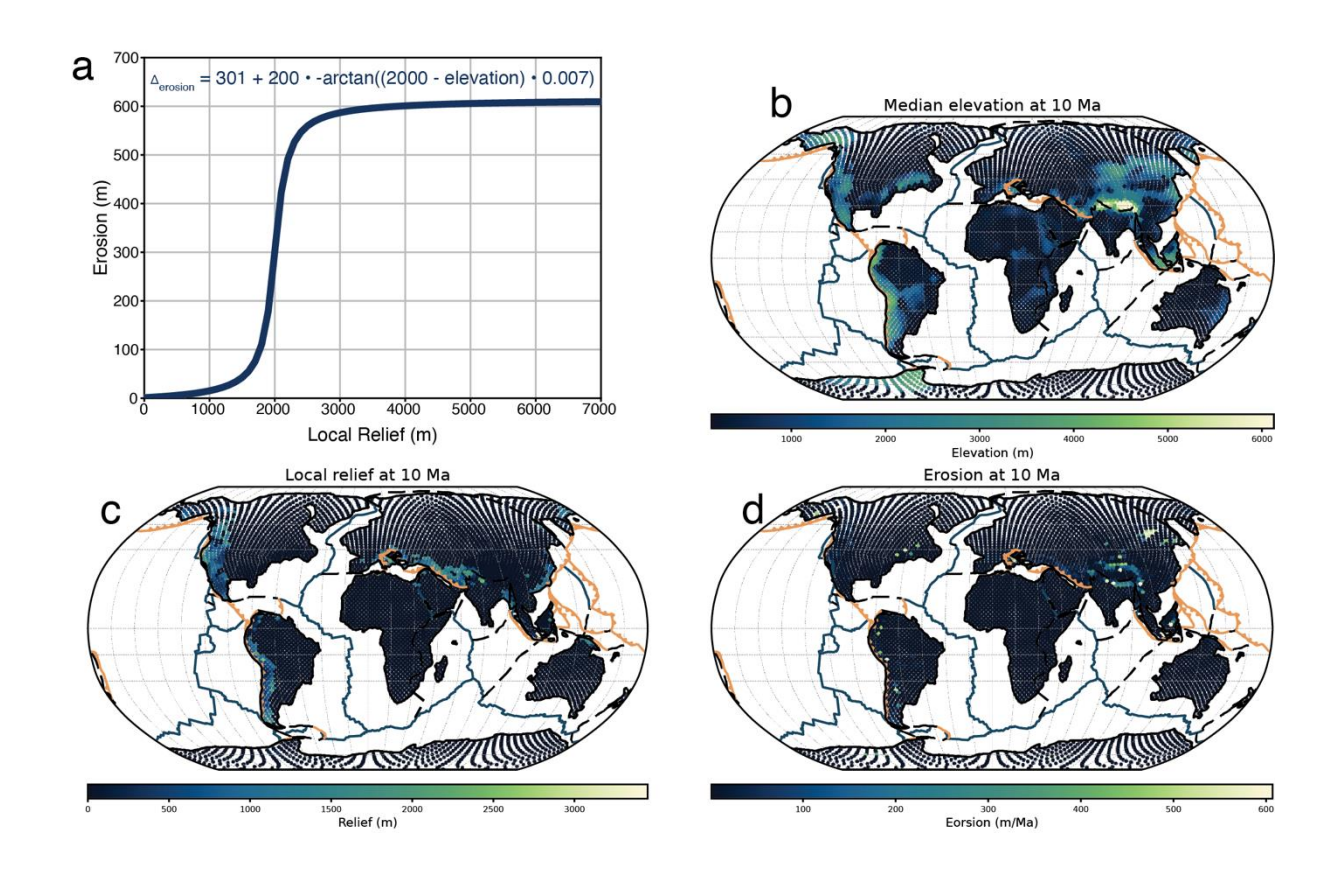


Figure 12. Change in topography due to rifting. There is a linear decrease from the current topography to -200 m (set as the minimum elevation).

Figure 13: Calculating erosion. (a) equation we used (modified from Montgomery and Brandon (2002)). (b) Median elevation at 10 Ma (using 21 nearest nodes). (c) Local relief at each node. (d) calculated erosion (i.e. curve in (a) applied to nodes in (c))



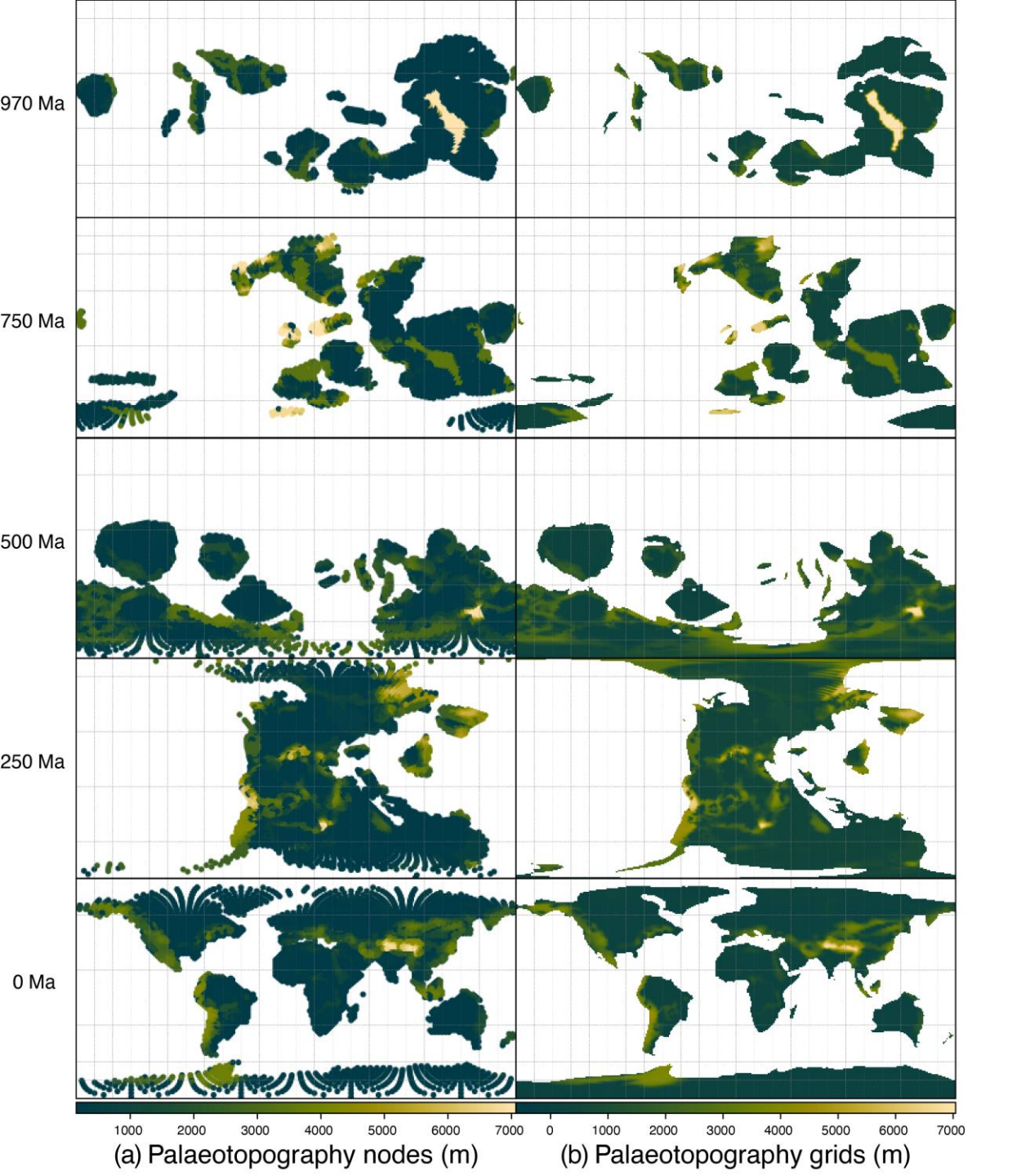


Figure 14: Conversion of (a) palaeotopography nodes (direct output from the model) to (b) palaeotopography grids at select timeslices.

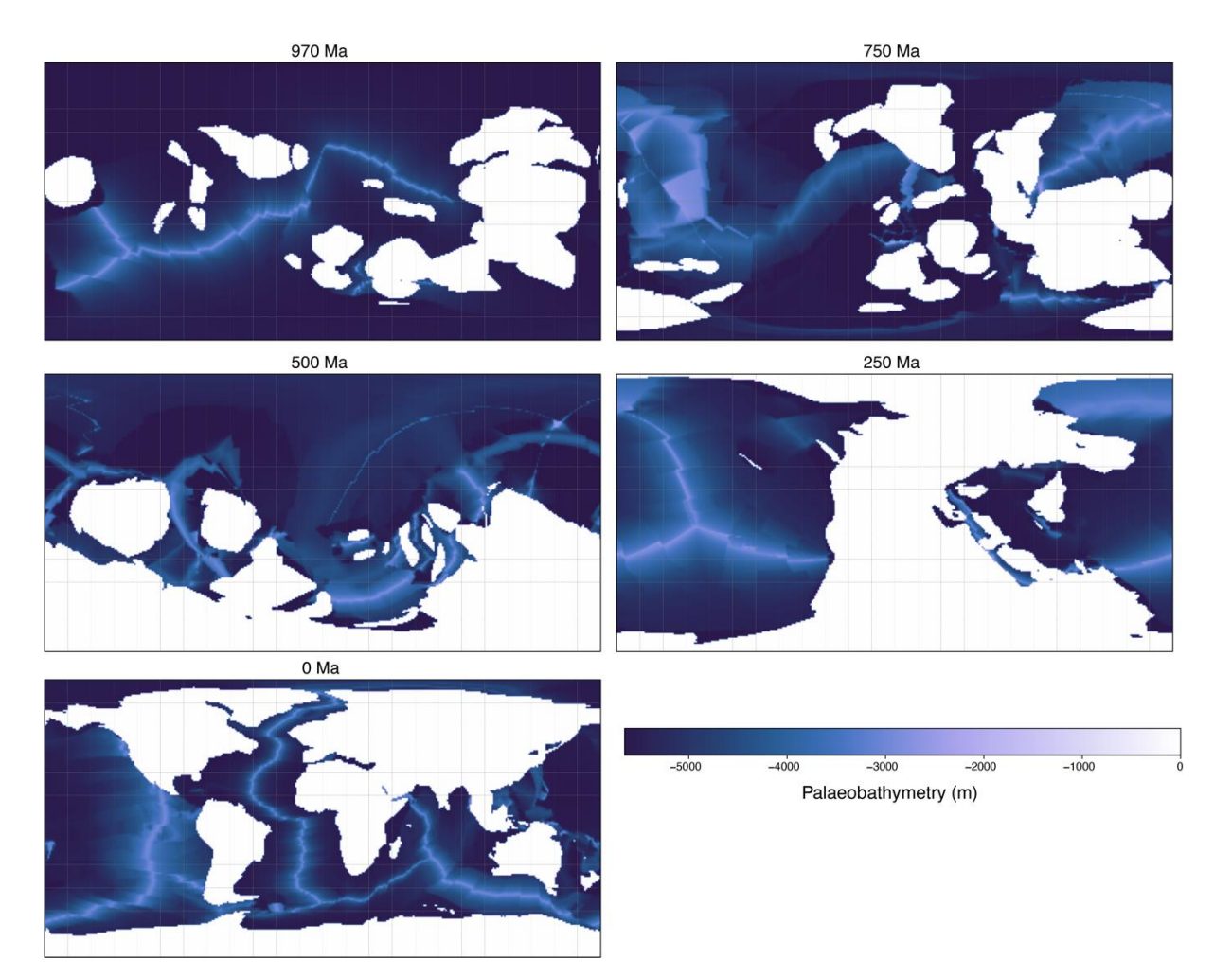


Figure 15: Modelled palaeobathymetry at select timeslices.

Figure 16: Flowchart showing the final phase of our method, combining grids, smoothing and outputting rasters.

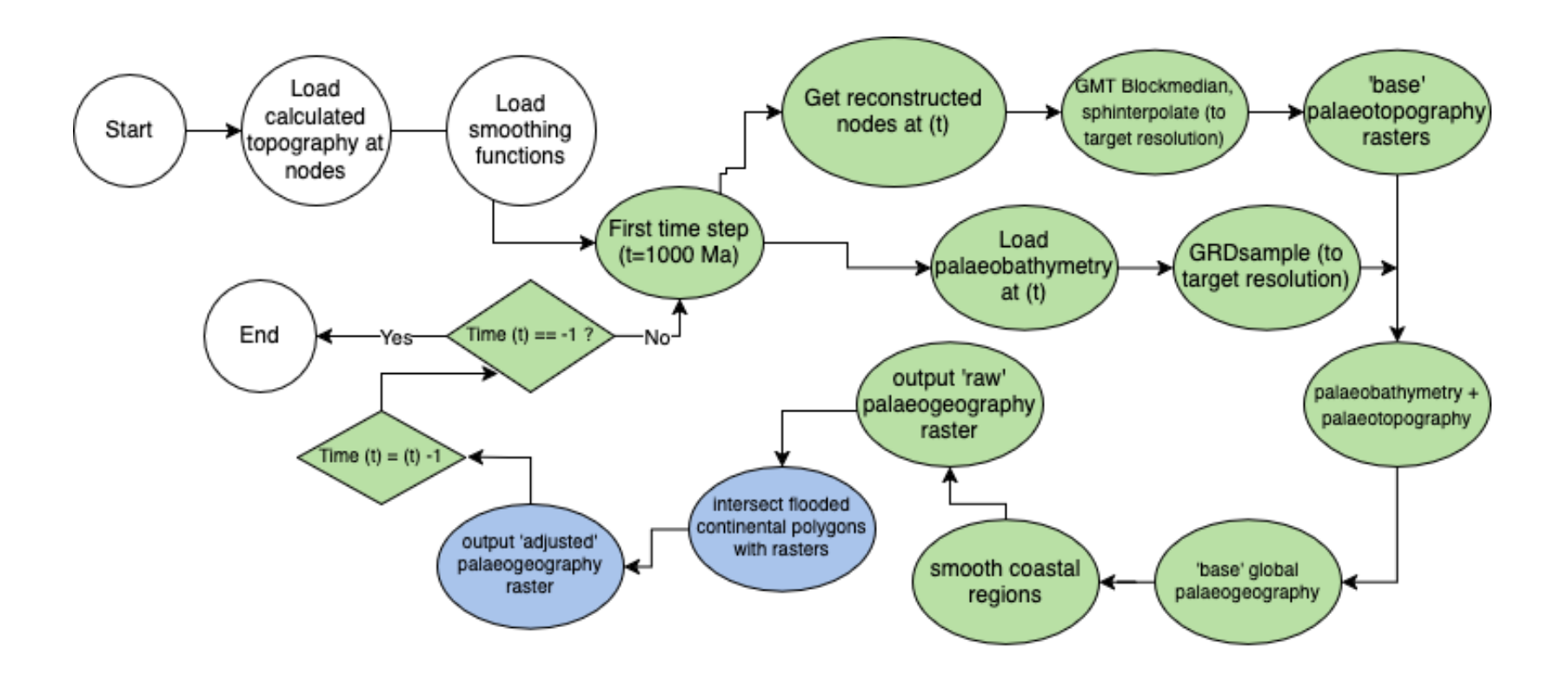
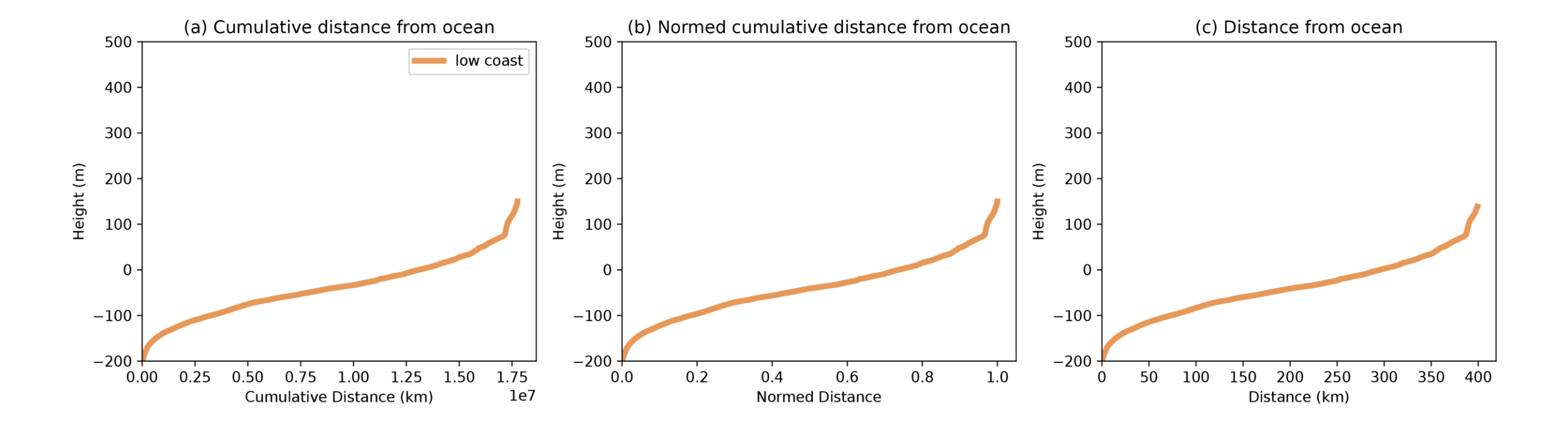
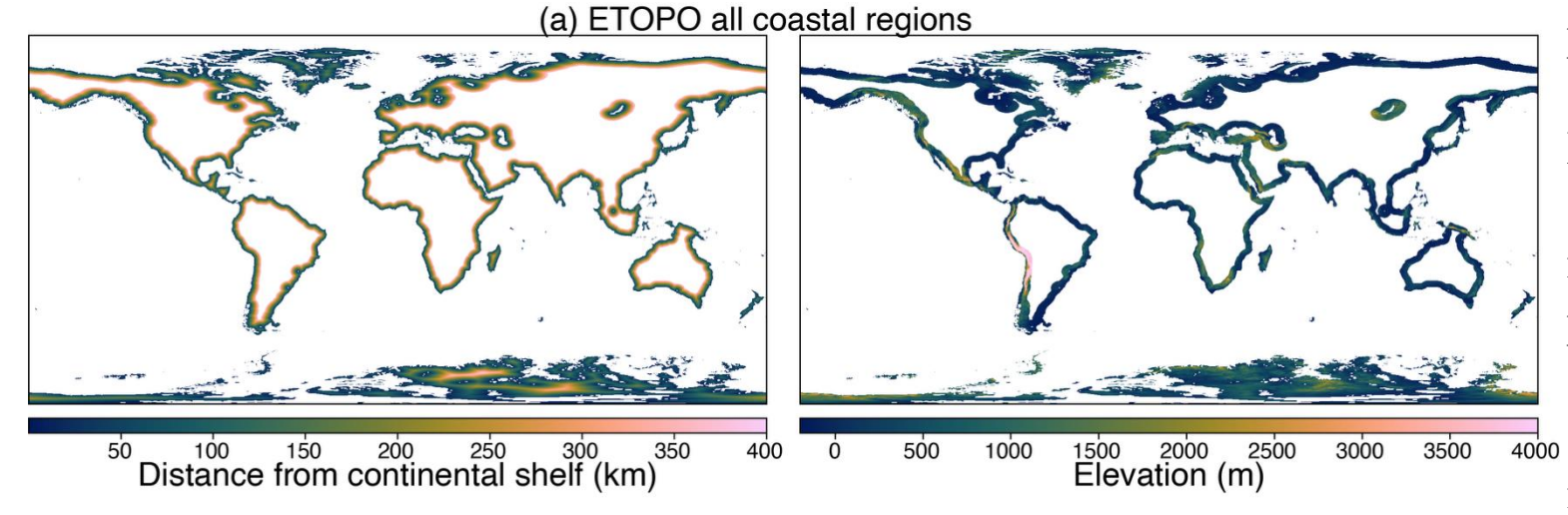
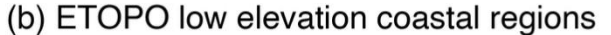


Figure 17: Hypsometric curves used to smooth grids based on distance from the ocean. (a) Elevation verses cumulative distance from the continental shelf. (b) As (a), but with normalised distance. (c) As (b) but extended to 400 km. These elevations from (c) are mapped onto our coastal regions.







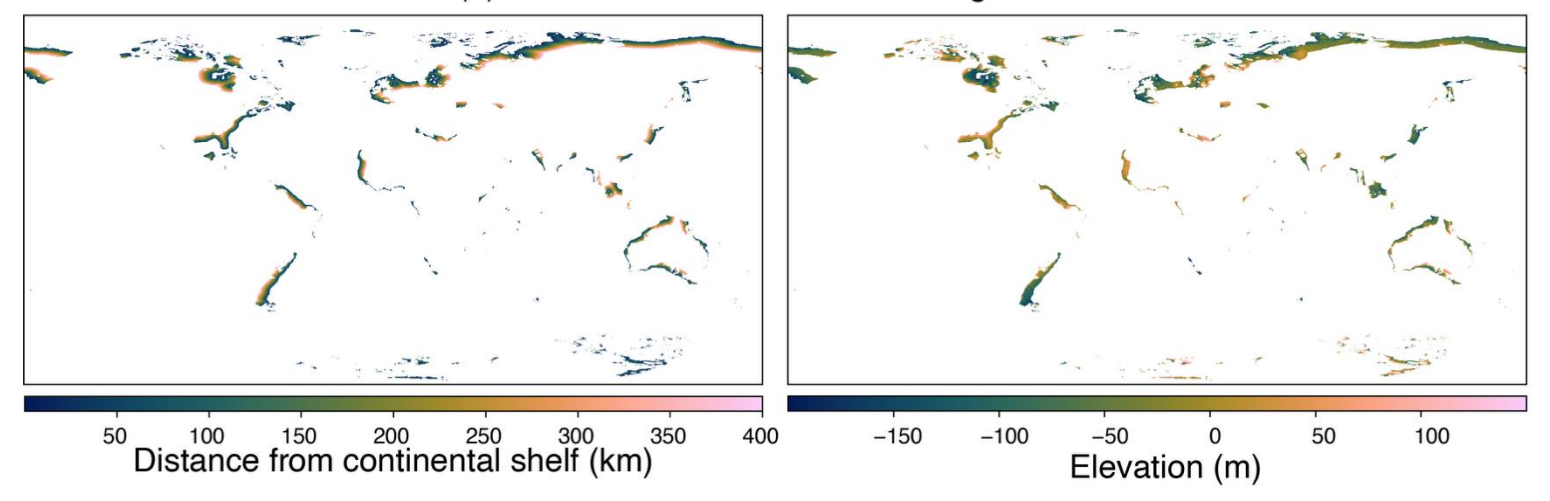


Figure 18: Coastal regions of the world at present-day extracted from ETOPO. First column show distance (to a maximum of 400 km) from continental shelf (defined at -200 m) and second column shows the elevation of those regions. (a) shows all coastal regions. (b) shows passive, low lying coastal regions (regions further than 400 km away than a mountainous area (defined as 2000 m elevation), and to a maximum elevation of 150 m.

Coastal regions in modelled topography at 50 Ma

Total Tegions in modell

Figure 19: Extracted coastal regions for smoothing from modelled topography at 50 Ma.

Figure 20: (a) Smoothing applied (e.g. Fig. 16c) at present-day and (b) at 50 Ma. First column show original topography, second shows smoothed, third shows the residual.

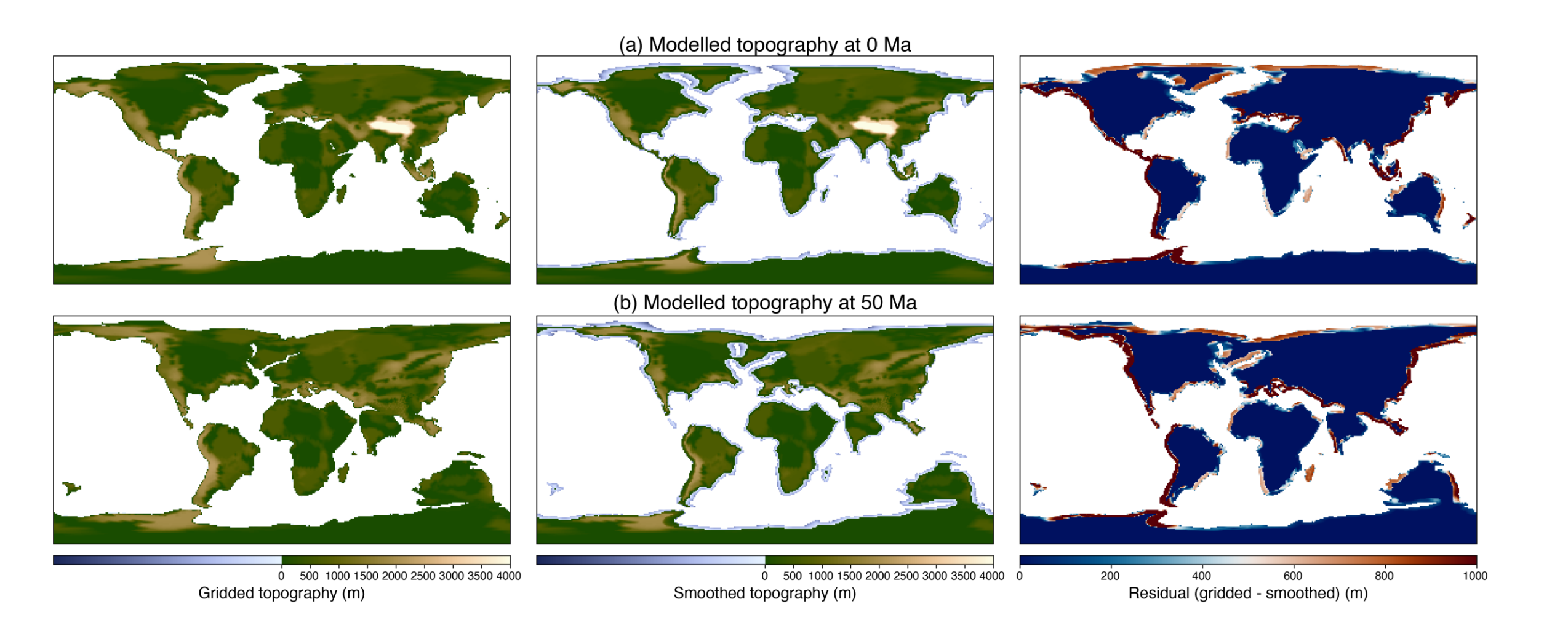


Figure 21. Combining grids to make a palaeogeography. (a) Palaeotopography after smoothing is applied. (b) Palaeobathymetry. (c) The two grids are added together (note both (a) and (b) cover inverse parts of the Earth's surface) to make a combined palaeogeographic map.

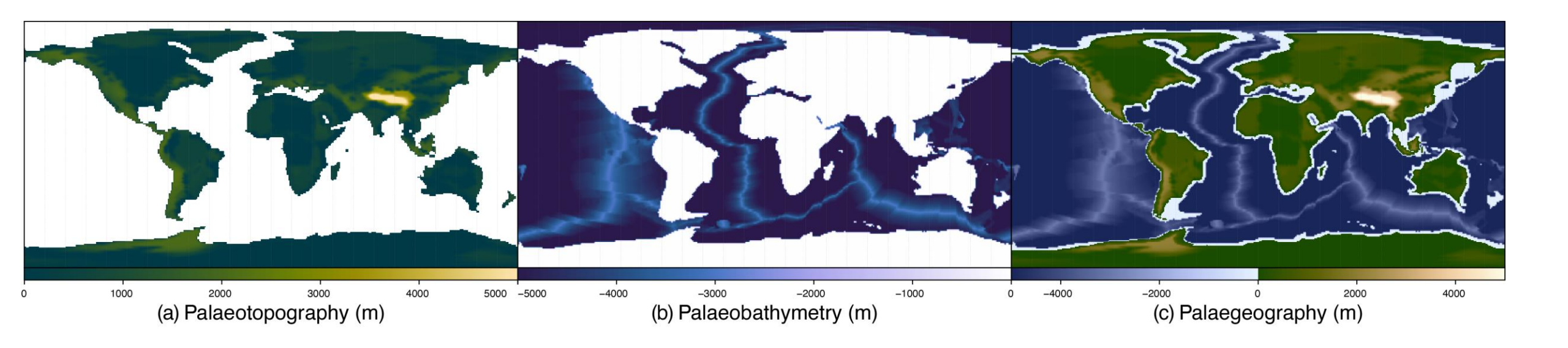


Figure 22. Filtered PBDB data used to constrain flooded continental areas over the Phanerozoic in their present-day location.

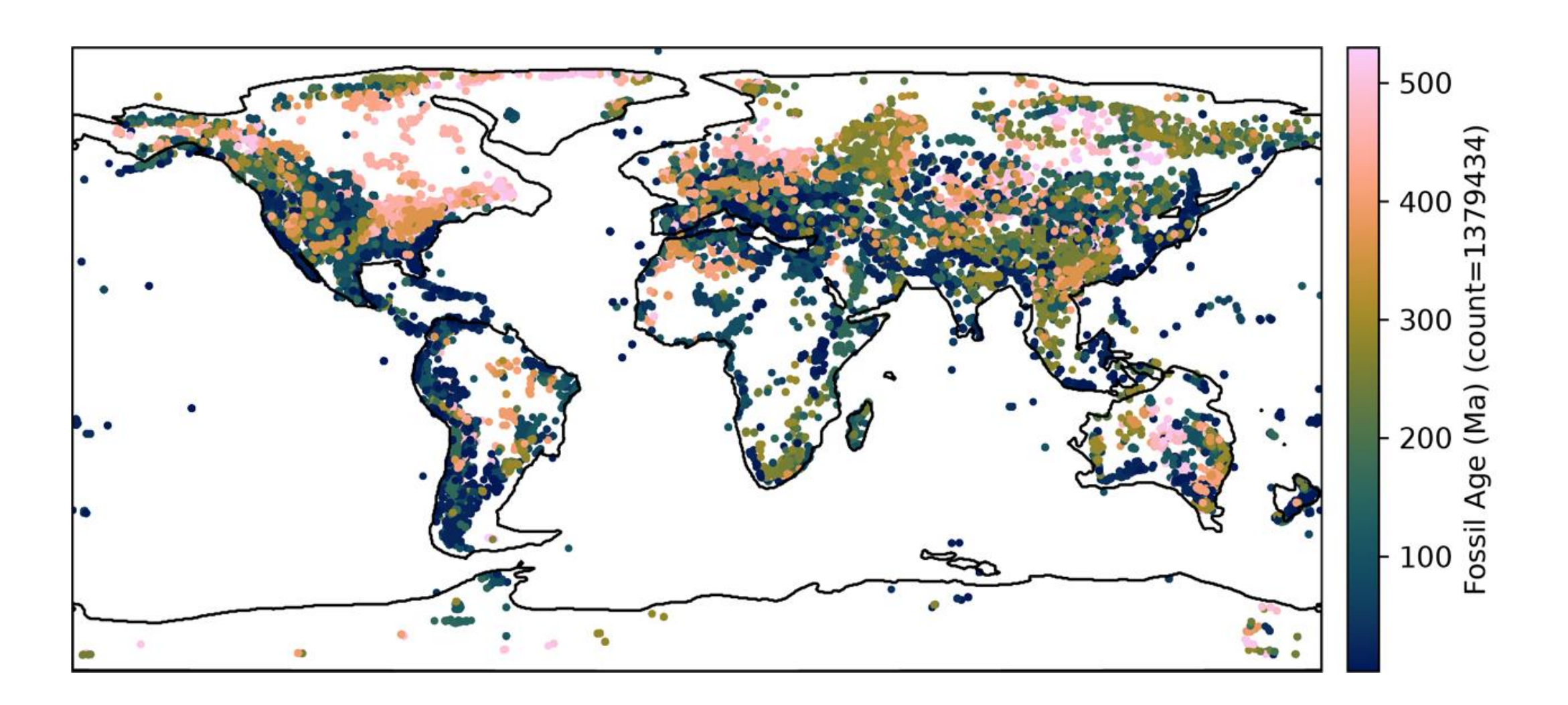
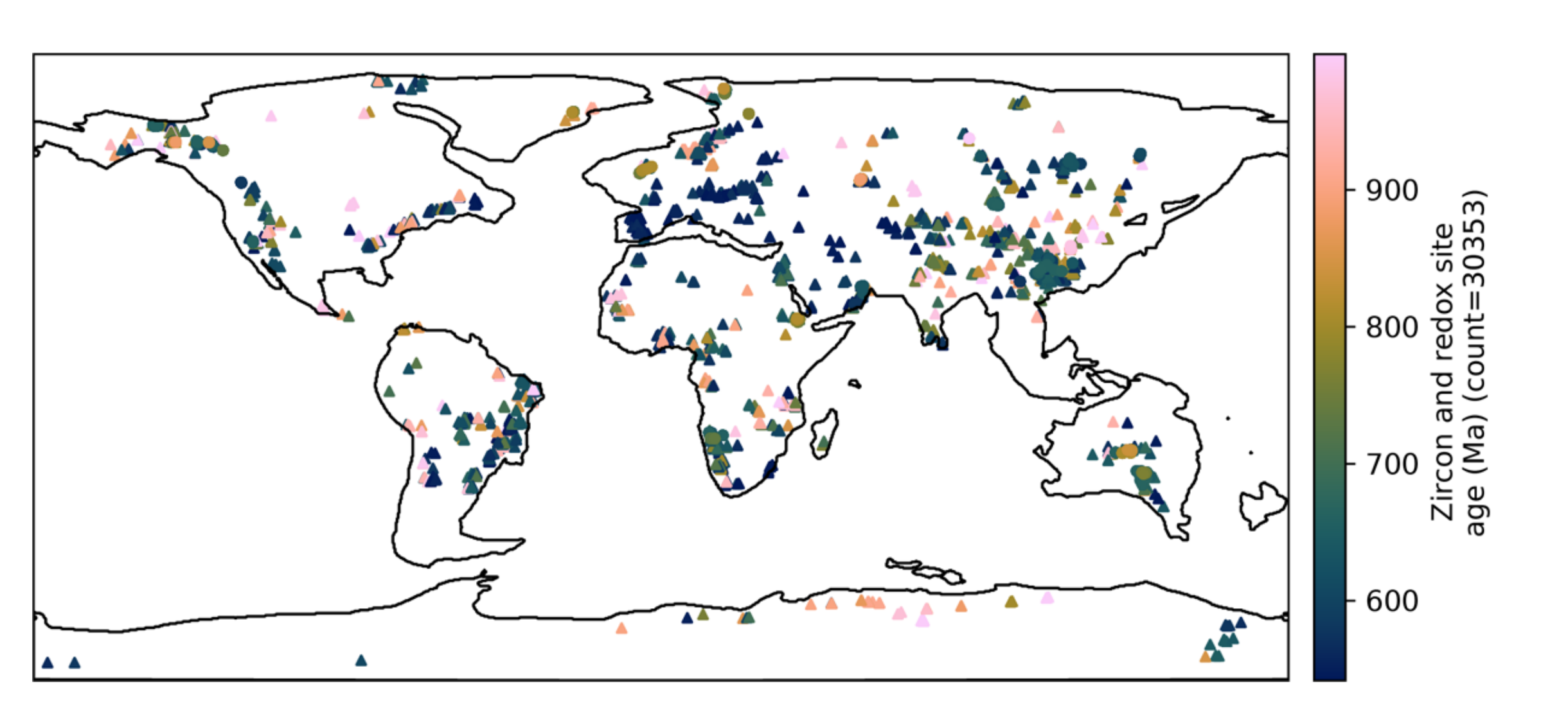


Figure 23. Detrital zircons with depositional ages (triangles) and Sedimentary Geochemistry and Palaeoenvironments Project (circles) datasets, in their present-day position.



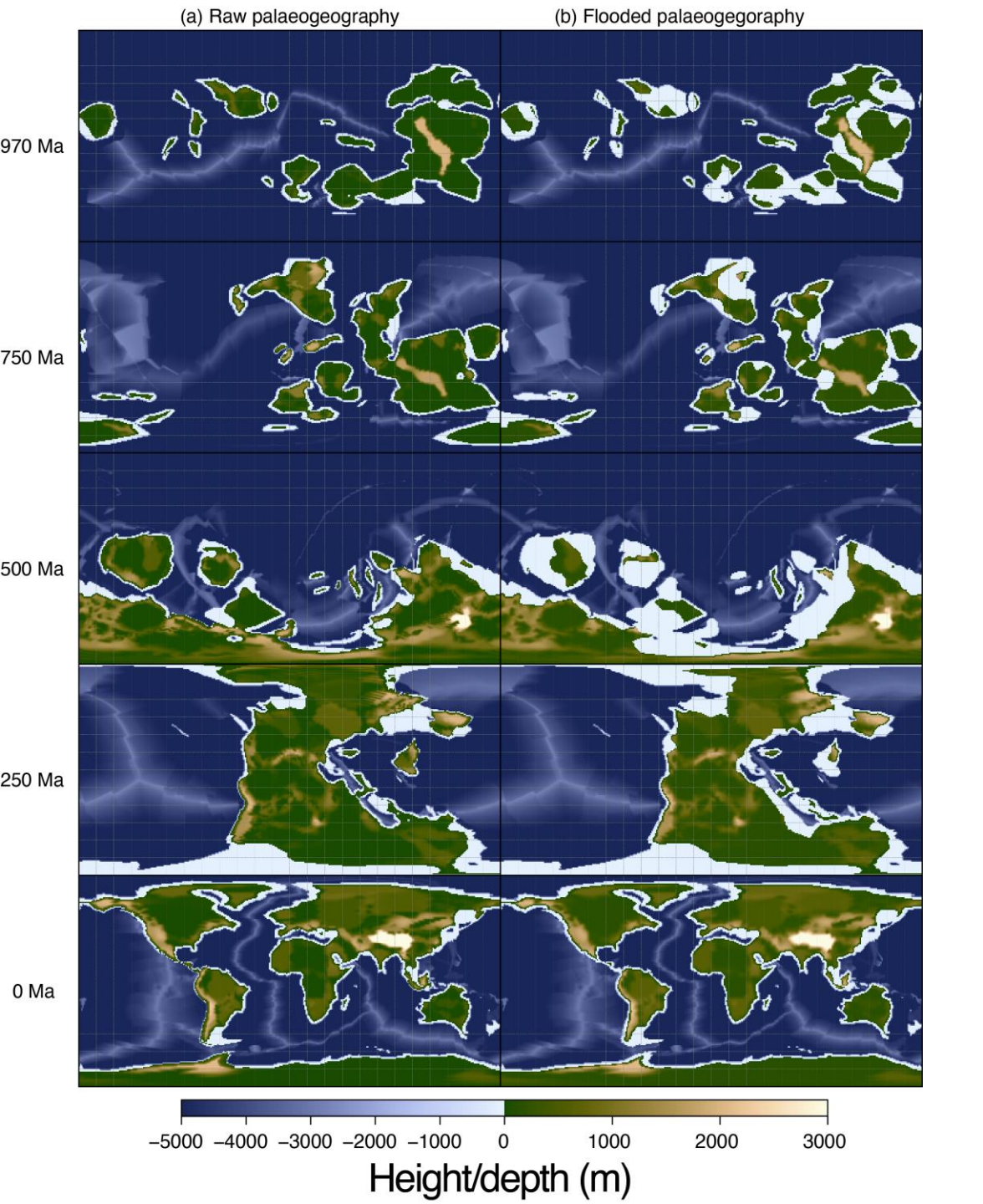
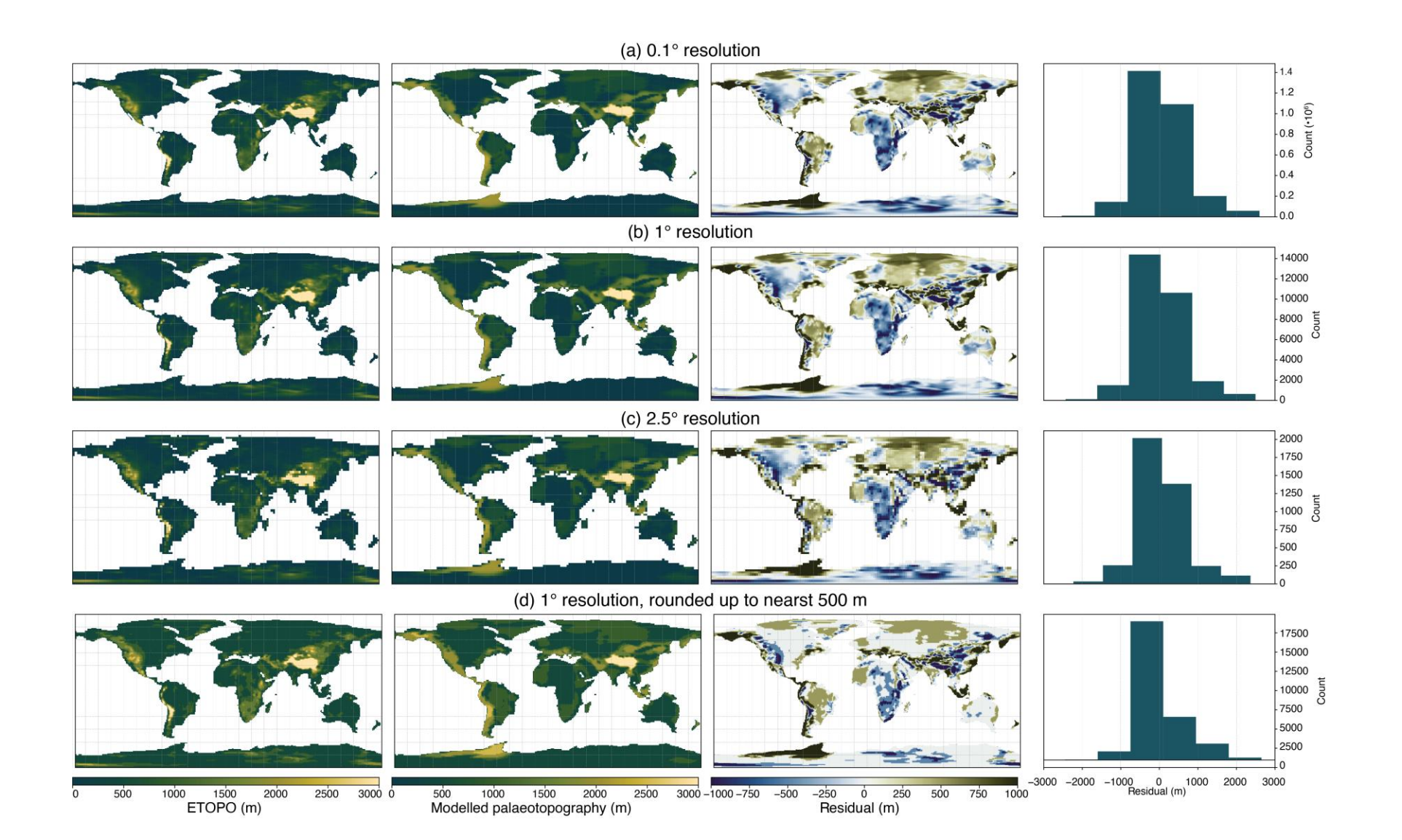


Figure 24. (a) Comparison of raw palaeogeography (i.e. Fig. 21c) to (b) after flooding maps have been applied.

Figure 25. Comparison of final palaeogeography (i.e. Fig. 24b) to ETOPO at different spatial resolutions. (a) a fine resolution with gridcells of 0.1°. (b) a coarser resolution with gridcells of 1° (this is our 'default' option). (c) a resolution roughly equivalent to HadCM3 and other high complexity climate models (2.5°). And (d) a coarse resolution (1° gridcells) where we bin everything into 500 m elevations.



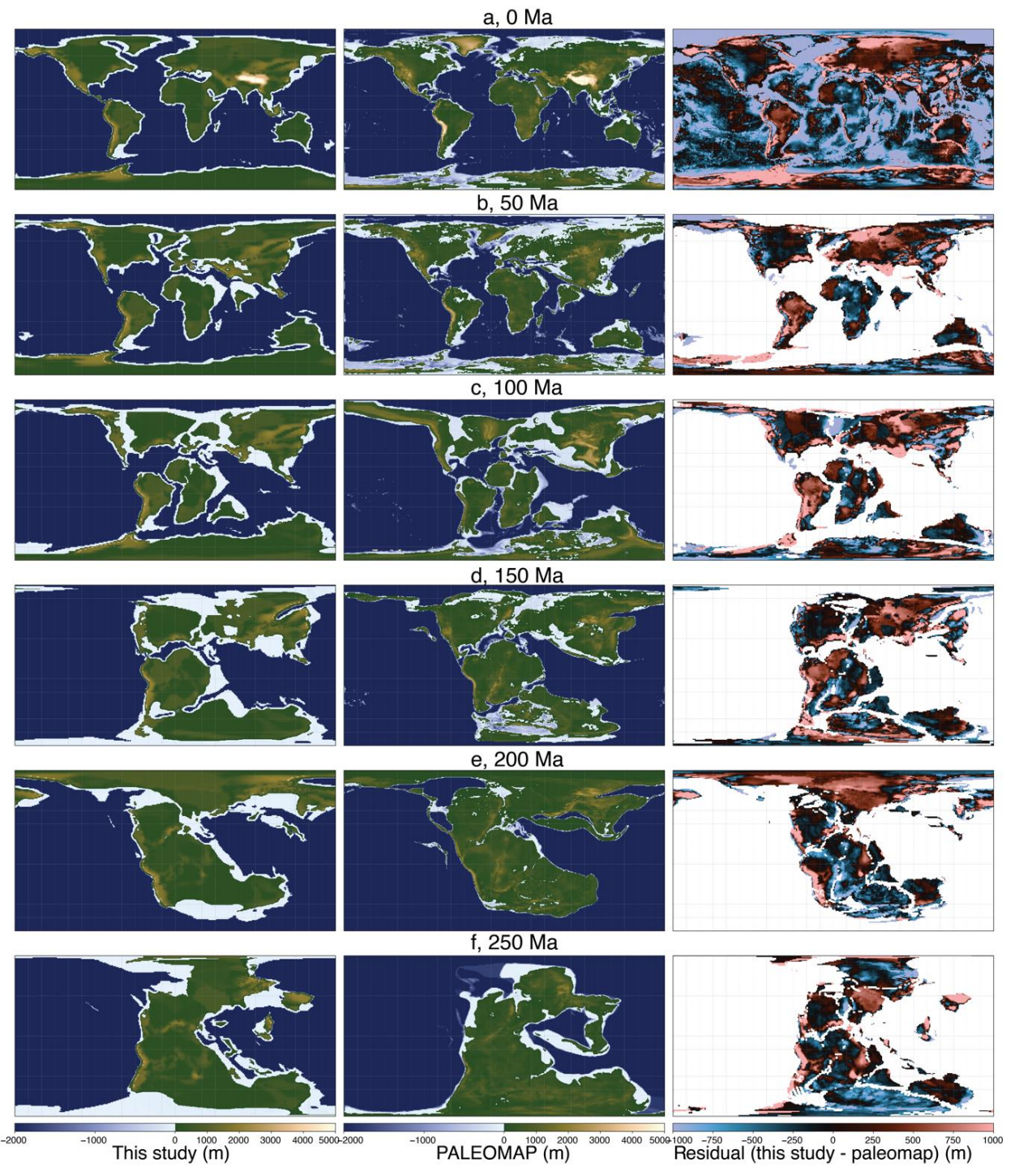


Figure 26: Comparison of results from our study and that of Scotese and Wright (2018),m alongside residual between 250 and 0 Ma. Note the present-day PALEOMAP is the ETOPO map. Note the residual is calculated by reprojecting the PALEOMAP reconstruction into the palaeomagnetic reference frame of Merdith et al. (2021).

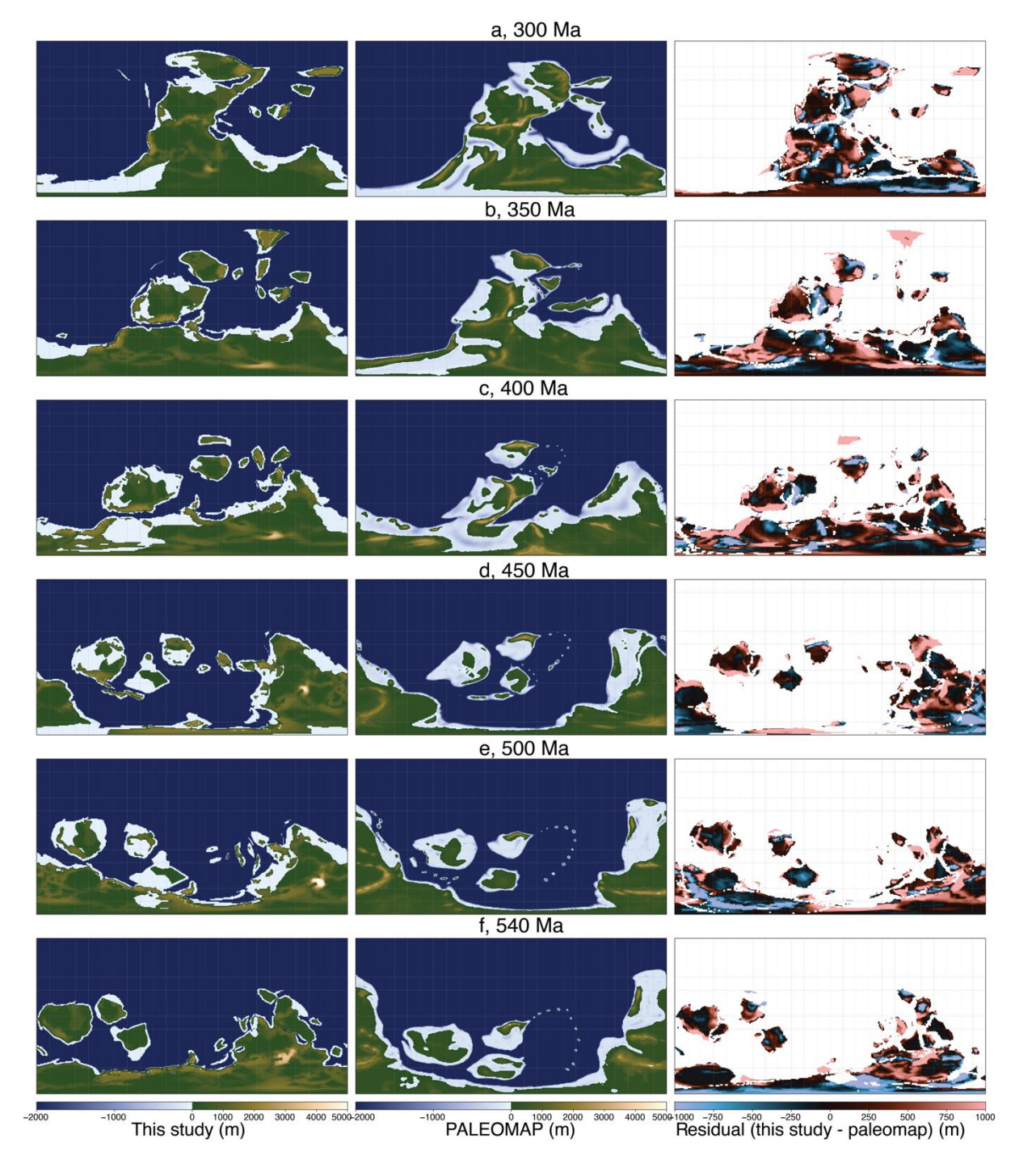


Figure 27: Comparison of results from our study and that of Scotese and Wright (2018), alongside residual between 540 and 300 Ma. Note the residual is calculated by re-projecting the PALEOMAP reconstruction into the palaeomagnetic reference frame of Merdith et al. (2021).

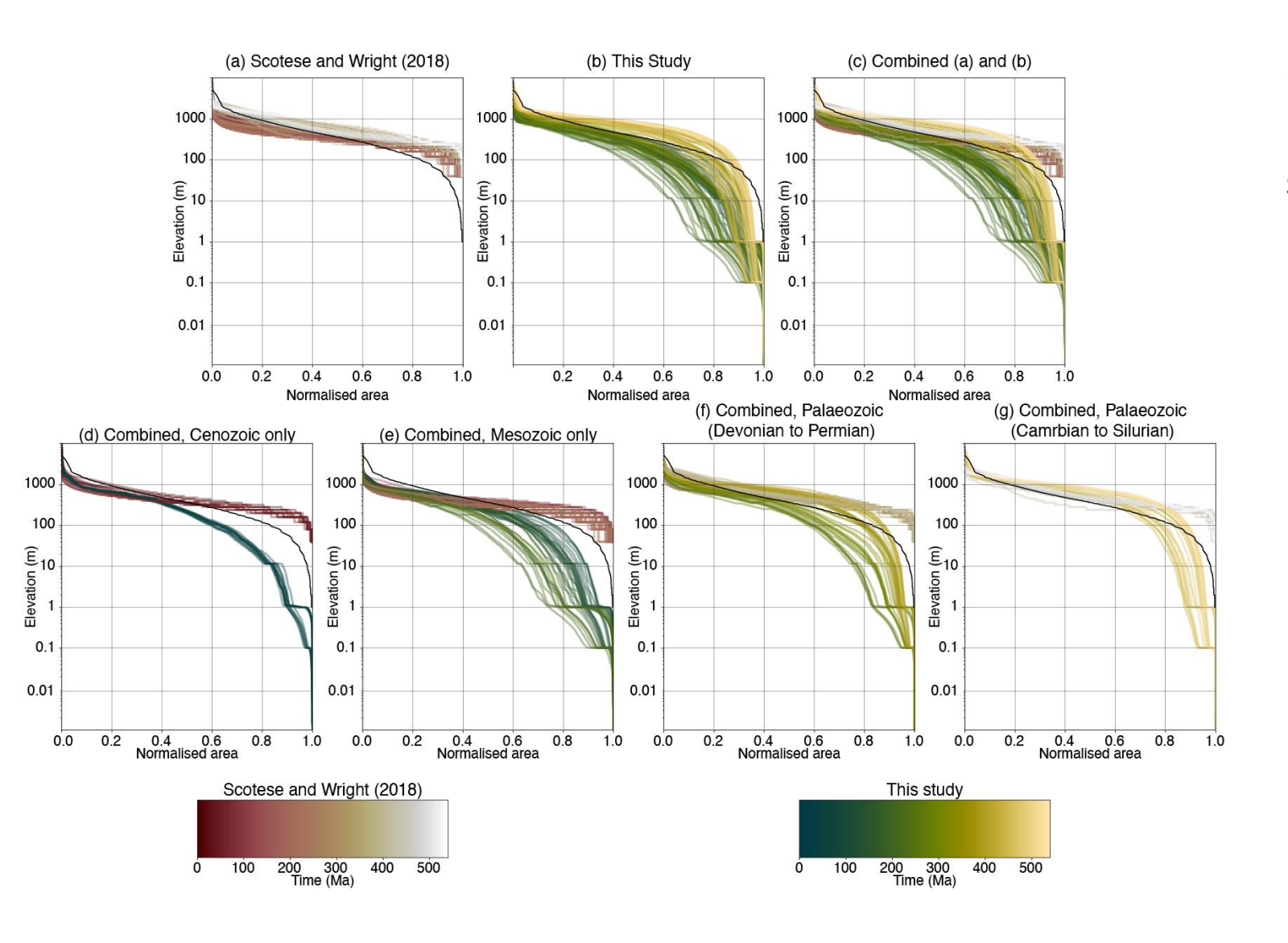
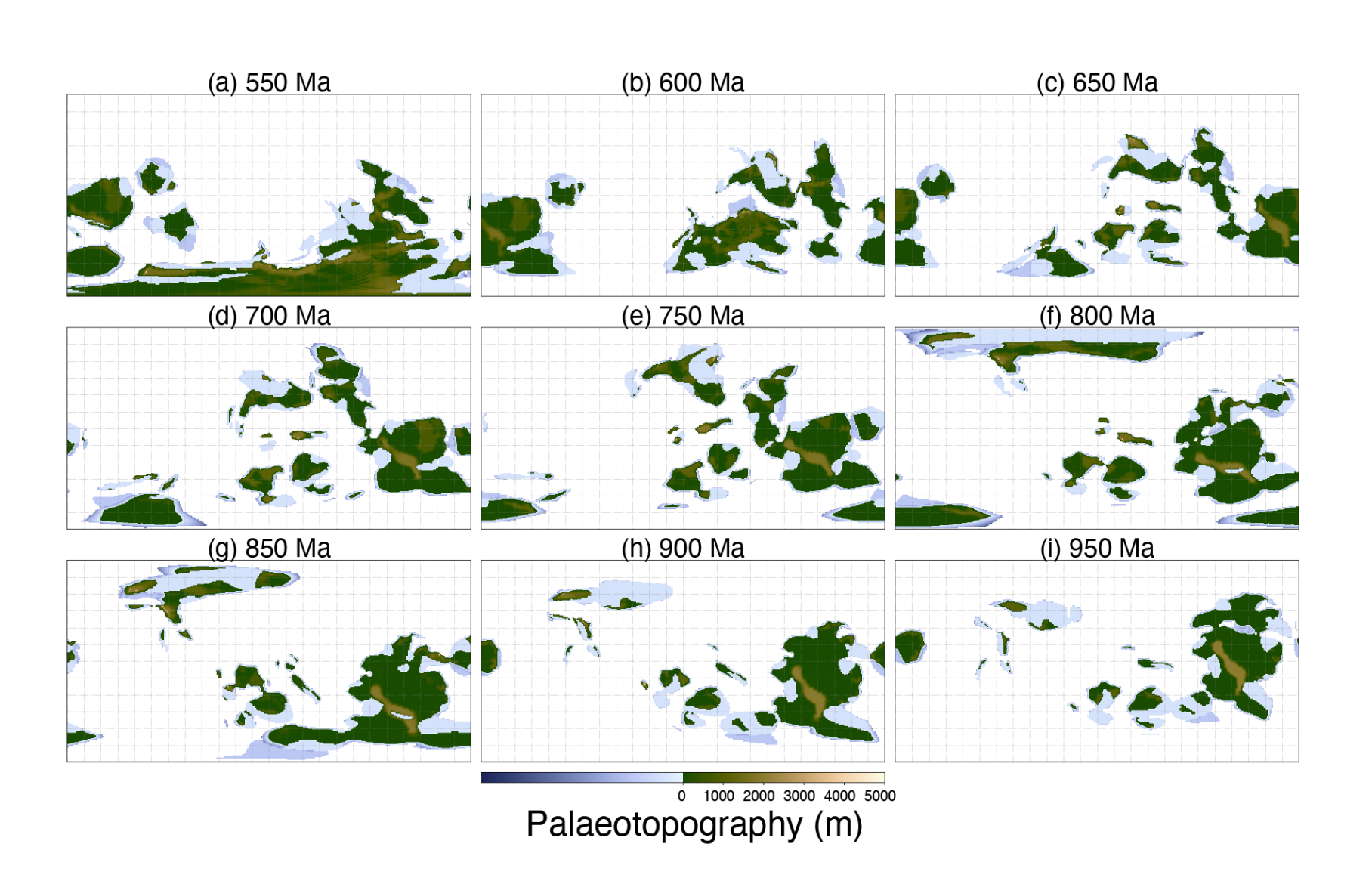


Figure 28. Comparison of hypsometry between (a) PALEOMAP and (b) our model. (c) shows both (a) and (b) plotted together, while (d–g) shows hypsometry broken into relative time intervals. In all plots the black line is the present-day hypsometry from ETOPO. In all models elevations were trimmed at 0.01 m.

Figure 29. Neoproterozoic topographies from this work, plotted every 50 Ma.



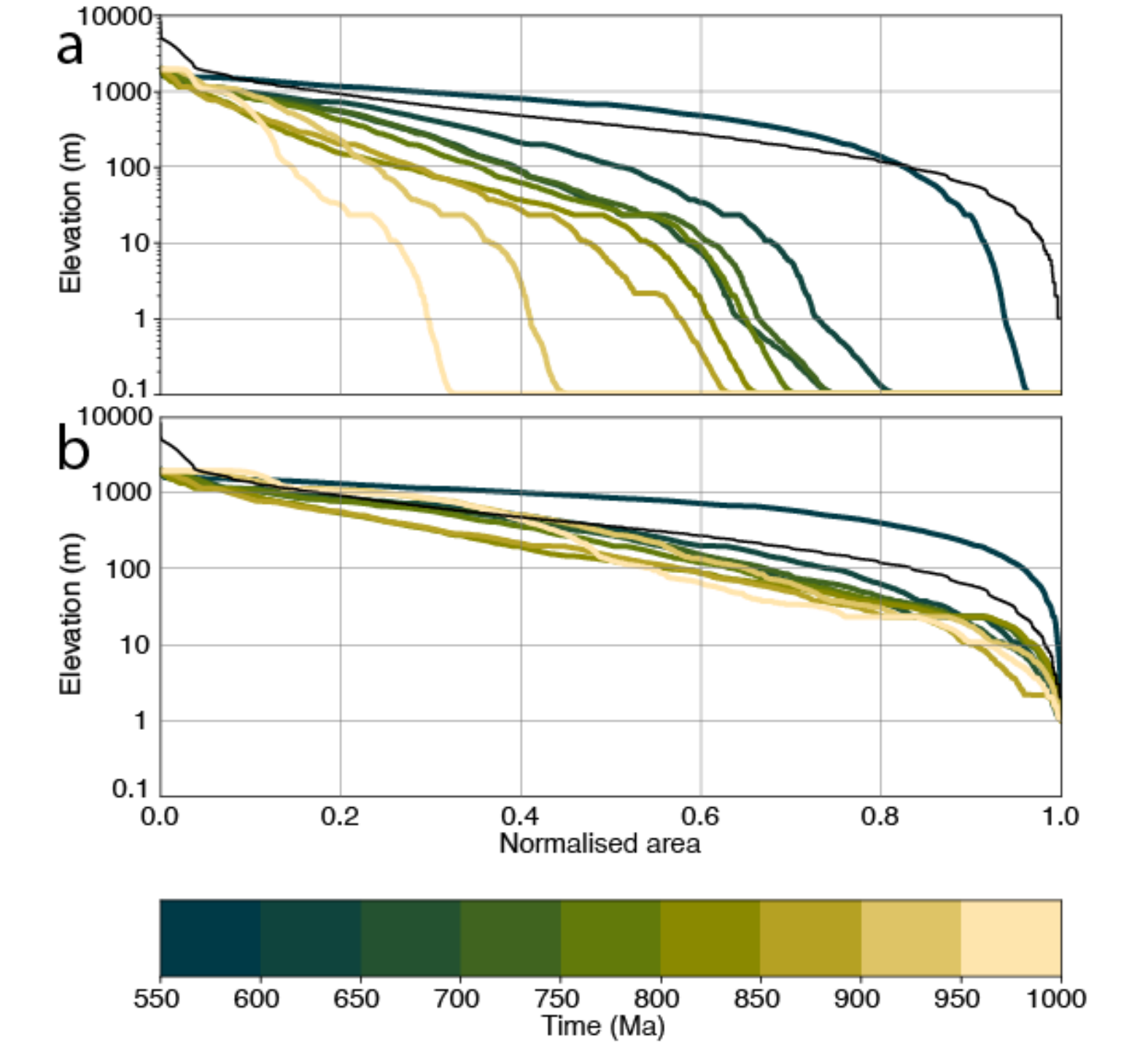


Figure 30. Hypsometry from our modelled topography during the Neoproterozoic. Black line is present-day hypsometry. (a) minimum topography was set to 0.1 m. (b) minimum topography was set to 1 m.

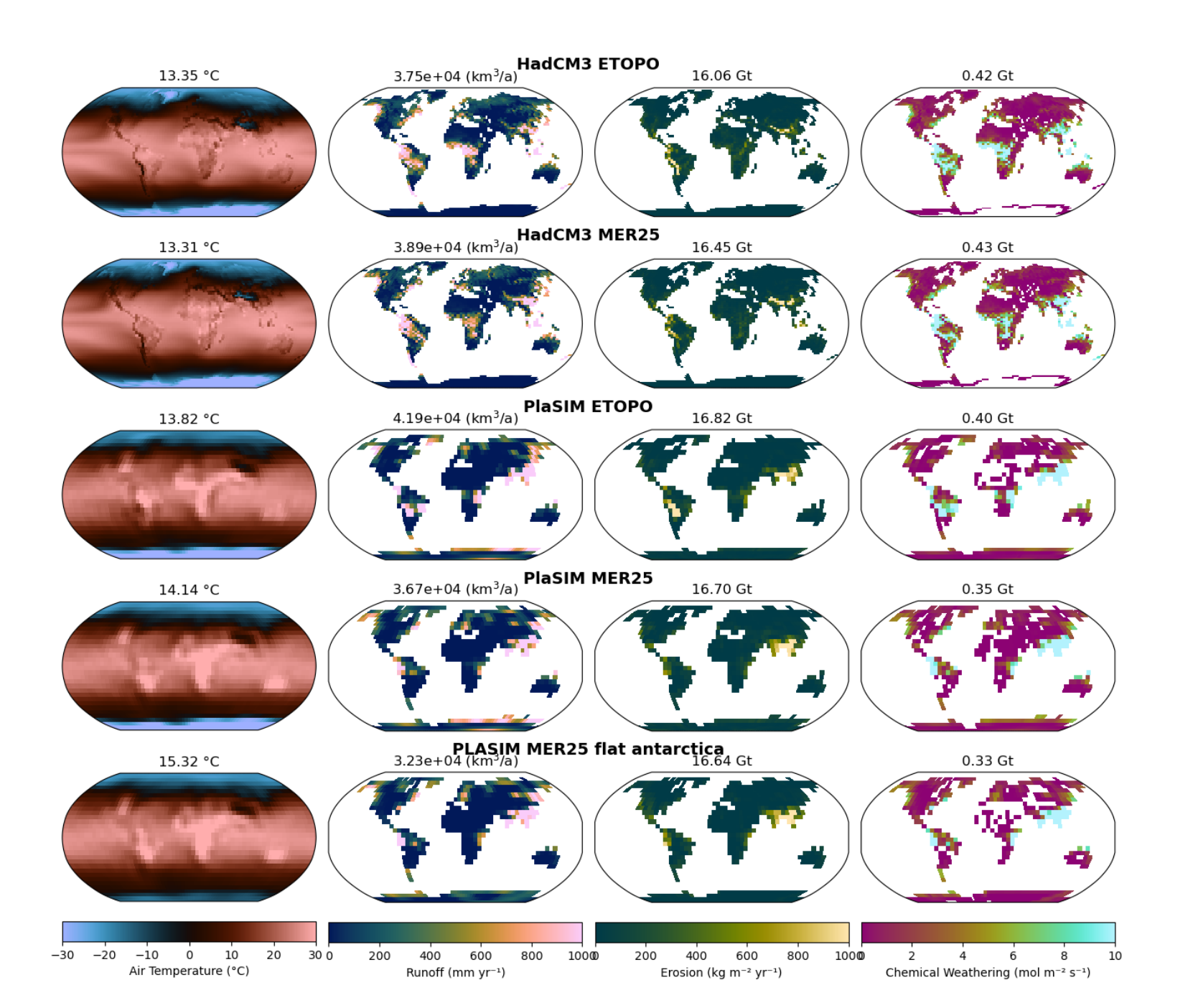
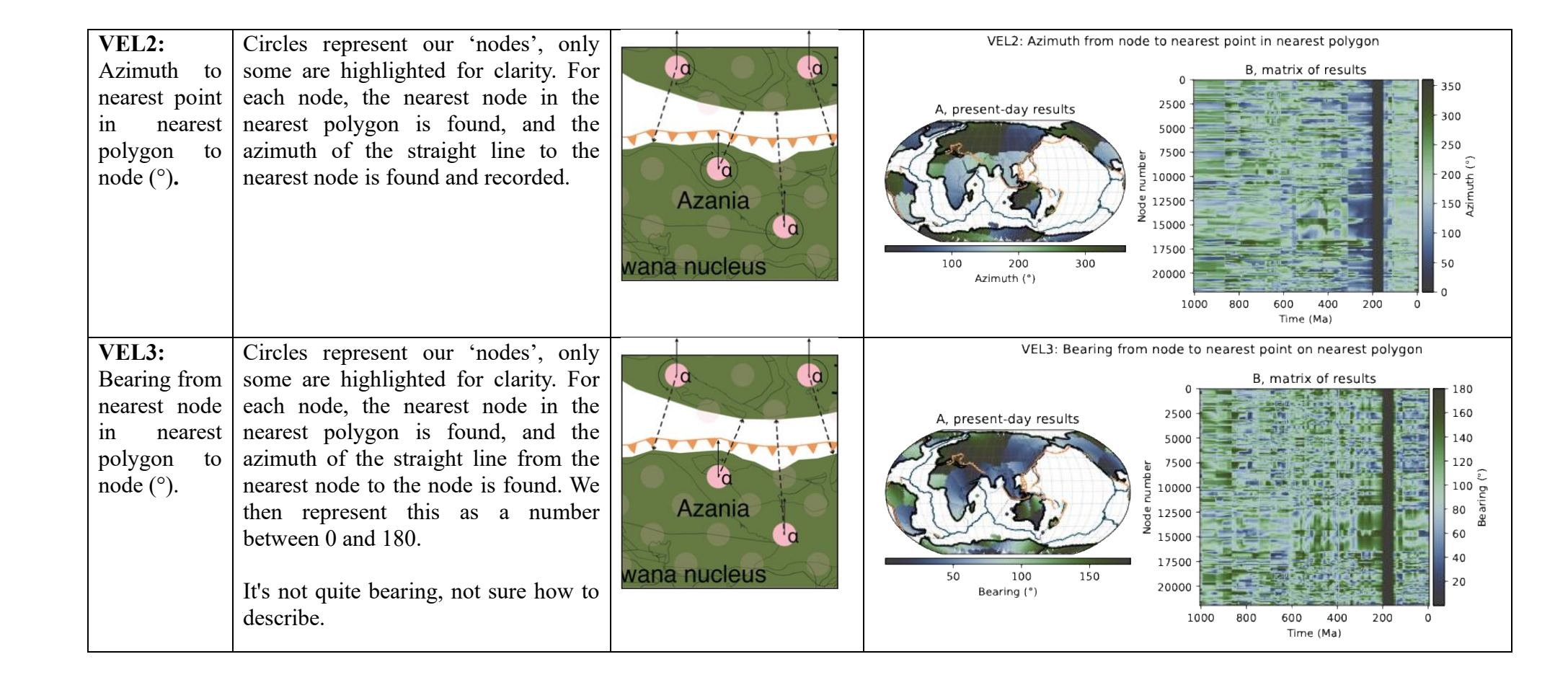


Figure 31. Comparison of pre-industrial climate model runs using HadCM3 and PlaSIM-GENIE, with ETOPO and the presentday topography from this work. Panels are surface air temperature, runoff, chemical erosion and weathering. Air temperature and runoff are taken directly from climate model outputs, erosion and chemical weathering are calculated after Mills et al. (2021); Merdith et. al. (2025), with erosion calculations from West et al. (2012) and Maffre et al. (2017).

Parameter	Figure caption	Example figure	Results
SZ1: Distance from node to nearest subduction zone (km).	Circles represent our 'nodes', only some are highlighted for clarity. Arrowed lines record distance to nearest downgoing subduction zone.	India Azania Gondwana nucleus	SZ1: Distance to nearest subduction zone B, matrix of results A, present-day results 2500 5000 7500 12500 15000 17500 15000 17500 20000 17500 20000 1000 1000 1000 1000 1000 1000
VEL1: Velocity azimuth of nearest point on nearest polygon to node (°).	Circles represent our 'nodes' and arrows represent the velocity magnitude vectors (showing direction of movement, and relative magnitude by size), only some are highlighted for clarity. For each node, the nearest node in the nearest polygon is found, and the azimuth of the velocity vector of that node is recorded.	Azania wana nucleus	VEL1: Velocity azimuth of nearest point on nearest polygon B, matrix of results 350 300 2500 7500 1000 12500 12500 17500 20000 17500 20000 17500 20000 1000 800 600 400 200 0 Time (Ma)



POLY1: Area of polygon containing node	Circles represent our 'nodes'. The area of the polygon containing the node is calculated and recorded.	P ₁ , a ₁	POLY1: Area of polygon containing node 8, matrix of results 2500 7500 1.75 1.50 1.25 (***) 1.00 (***) 1.75 1.50 1.75 1.50 1.75 1.50 1.75 1.50 1.00 1.75 1.50 1.00 1.75 1.50 1.00 1.75 1.00
POLY2: Area of nearest polygon from polygon containing node	Circles represent our 'nodes', only some are highlighted for clarity. The closet polygon to each node is identified and the area of this polygon is recorded.		POLY2: Area of nearest polygon to node 8, matrix of results 100 1000

POLY3:	Circles represent our 'nodes', only	POLY3: Distance to nearest polygon
Distance from node to nearest polygon	some are highlighted for clarity. The closet polygon to each node is identified and the minimum distance from the node to this polygon is recorded.	A, present-day results 10000 A, present-day results 10000 100
POLY4: Distance of node to nearest 'ocean'	Circles represent our 'nodes', only some are highlighted for clarity. We assume that 'ocean' is represented by polygonal boundaries (which represent a theoretical continent-ocean boundary. The minimum distance from each node to the polygon edge is recorded.	POLY4: Distance to nearest ocean B, matrix of results A, present-day results 1000 1000 1500 1000

POLY5: Distance from node containing polygon to nearest polygon	Circles represent our 'nodes', coloured by polygon they are on. Here we find the nearest polygon to the node and calculate the distance between the that polygon and the node polygon. Edge colours of circles represent the closest polygon to that containing polygon.		POLY5: Distance from node containing polygon to nearest polygon B, matrix of results 3000 2500 7500 7500 1000 1500 2000 2500 17500 2000 2000 2000 2000 2000 2000 2000
LIP1: Node in LIP polygon	Circles represent our 'nodes', only some are highlighted for clarity. An example (made-up) LIP polygon is showing in grey with dashed outline. Nodes within the LIP polygon are identified and recorded.	India LIP outilne Azania Gondwana nucleus	LIP1: Is node in recently erupted LIP? B, matrix of results 1.0 2500 5000 7500 10000 17500 17500 17500 17500 10000 1

Parameter	Description	Units/details	Value and Reference?	Equations relevant to?
t	Time	Ма		
n	node			
$active_n(t)$	Is node active?	1/0 (yes or no)		1
t_n^{start}	Start time of node	Ма		1
$t_n^{\it end}$	End time of node	Ма		1
$n_{arc}(t)$	Is node in a continental arc margin	1/0 (yes or no)		2
$d_{SZ1}(t)$	Matrix of distance to nearest downgoing subduction zone at time (t)	km		2, 3
$d_{arc\;threshold}$	Threshold cutoff	km	450 (Zahirovic et al. 2022)	2
$n_{previous\ arc}(t)$	Was a node previously close to an arc?	1/0 (yes or no)	,	3, 10
$d_{overriding}$ cc $$ threshold	Maximum distance inboard of subduction zone that might be affected by a continental collision	Km	2800	3, 10
$n_{poly\ area}(t)$	Area of node containing polygon	km²		4, 10
$a_{ccthreshold}$	Minimum area of a polygon for continental collisions	km²	4•10 ⁷ km ²	4, 10
$d_{POLY1}(t)$	Matrix of polygon-containing- node area	km²		4, 10

$n_{\Delta dist\ to\ nearest\ poly}(t)$	Changing distance to nearest	1/0 (yes or no)		5, 10
	polygon from node			
d_{POLY3}	Matrix of distances to nearest	km		5, 10
	polygon of node			
$n_{area\ of\ nearest\ poly}(t)$	Area of nearest polygon to	km²		6, 10
,	node			
a_{POLY2}	Matrix of the area of nearest	km²		6, 10
	polygon to each node			
$a_{downgoing\ cc\ threshold}$	Minimum area of downgoing	km²	7•10 ⁶ km ²	6, 10
	polygon			
$n_{ m dist}$ ance of node poly to nearest poly	distance from polygon-	1/0 (yes or no)		7, 10
,	containing-node to nearest			
	polygon test			
d_{POLY5}	Matrix of the distance from			7, 10
. 02.0	polygon-containing-node to			
	nearest polygon			
$d_{poly\ proximity\ threshold}$	Distance between polygon-	km	500	7, 10
	containing-node and nearest			
	polygon			
n_{VEL1}	Matrix of			8
n_{VEL2}				8
n_{VEL3}	Matrix of convergence	0		8, 9
	direction between node and			
	its nearest node on the			
	nearest polygon			
$n_{bearing\ to\ nearest\ poly}$	Convergence direction test	1/0 (yes or no)		9, 10
$ heta_{bearing\ sensitivity}$	Maximum angle from orthogonal collision	0	30°	9, 10

n_{ccenv}	Is node in a continental	1/0 (yes or no)		10, 16
	collision environment?			
$n_{rift\;env}$	Is a node in a rift	1/0 (yes or no)		10
•	environment?			
d_{POLY4}	Matrix of distance between	km		10
	node and nearest polygon			
	edge (i.e. ocean)			
$d_{maxriftdistance}$	Maximum distance inland	km	400 km	10
,	from an incipient ocean			
	rifting occurred			
$n_{LIP\ environment}$	Is a node in a LIP?	1/0 (yes or no)		11
$LIP_{polygon}$	Separate LIP database		Park et al.	12
polygon			(2011)	
$n_{ctopo} == n_{topo}(t)$	Current topography of nodes	m		13, 14, 17, 18
$\mathit{Grenville}_{polygon}$	Polygon of the extent of the		Pehrsson et	14
polygon	Grenville Orogen		al. (2016);	
			Hasterok et	
			al. (2022)	
n_{cctopo}	Is a node within our temporal	1/0 (yes or no)		15
2000	threshold of a continental			
	collision environment?			
$n_{rift\ topo}$	Is a node within our temporal	1/0 (yes or no)		16
1.0,0000	threshold of a rift			
	environment?			
$topo_{\min grow}$	Minimum amount of	М	1	17
	elevation change			
$topo_k$	y-intercept of decay equation		300, 700, 100	17
			(arc, cc, LIP)	

strength of the decay curve		0.001, 0.0003, 0.001 (arc, cc, lip)	17
Change in rift topography	m		18
Min elevation of a rift at cessation	m	-200 m	18
Duration from model time until incipient ocean basin forms (i.e. lifespan of the rift remaining)	Ма		18
Local relief of each node	m		20
Median topography of each node using nearest 21 neighbouring nodes	m		20
Erosion at each node	m		21
Constant to ensure that min erosion is above 1	m	301	21
Stretching factor for distance between two horizontal asymptotes		200	21
x-value of vertical asymptote	m	2000	21
Strength of arctan curves at asymptotes		0.007	21
	Change in rift topography Min elevation of a rift at cessation Duration from model time until incipient ocean basin forms (i.e. lifespan of the rift remaining) Local relief of each node Median topography of each node using nearest 21 neighbouring nodes Erosion at each node Constant to ensure that min erosion is above 1 Stretching factor for distance between two horizontal asymptotes x-value of vertical asymptote Strength of arctan curves at	Change in rift topography m Min elevation of a rift at cessation Duration from model time until incipient ocean basin forms (i.e. lifespan of the rift remaining) Local relief of each node m Median topography of each node using nearest 21 neighbouring nodes Erosion at each node m Constant to ensure that min erosion is above 1 Stretching factor for distance between two horizontal asymptotes x-value of vertical asymptote m Strength of arctan curves at	Change in rift topography m Min elevation of a rift at cessation Duration from model time until incipient ocean basin forms (i.e. lifespan of the rift remaining) Local relief of each node m Median topography of each node using nearest 21 neighbouring nodes Erosion at each node m Constant to ensure that min erosion is above 1 Stretching factor for distance between two horizontal asymptotes x-value of vertical asymptote m O.001 (arc, cc, lip) Ma -200 m -200 m 301 301 200 200 Strength of arctan curves at O.007

Equations file

(1) Node active or not

$$n_{active}(t) = \begin{cases} 1, & \text{if } t_n^{start} \le t \le t_n^{start} \\ 0, & \text{otherwise} \end{cases}$$
 (1)

(2) Find continental arcs

$$n_{arc}(t) = d_{SZ1}(t) < d_{arc\ threshold\ deformed}$$
 (2)

(3) Arc deformation multiplier

$$deform_{arc} = 1 + \frac{2}{e^{0.05*duration_{last orogen}}}$$
 (3)

(4) Apply deformation distance to arcs

$$d_{arc\ threshold\ deformed} = d_{arc\ threshold} \times deform_{arc} \tag{4}$$

(5) Continental collisions proceed from the presence of a continental arc

$$n_{previous\ arc}(t) = \begin{cases} \frac{1\ if\ \sum_{t=1}^{t+10} \sum_{n \in N} \left(d_{SZ1} < d_{overriding\ cc\ threshold} \right)}{0, otherwise} \end{cases} \tag{5}$$

(6) overriding plate polygon is large enough to support extensive thickening

$$n_{poly\ area}(t) = \begin{cases} \frac{1\ if\ d_{POLY1}(t) > a_{cc\ threshold}}{0, otherwise} \end{cases} \tag{6}$$

(7) nearest polygon is getting closer test

$$n_{\Delta dist \ to \ nearest \ poly}(t) = \left(\left(d_{POLY3}(t+10) - d_{POLY3}(t+9) \dots d_{POLY3}(t) \right) < 0 \right) (\&)$$

$$\left(\left(d_{POLY3}(t-1) - d_{POLY3}(t) \right) > 3000 \right) (\&)$$

$$\left(d_{POLY3}(t-1) < 2000 \right)$$
(7)

(8) downgoing polygon is big enough to cause underplating

$$n_{area\ of\ nearest\ poly}(t) = a_{POLY2}(t+1) > a_{downgoing\ cc\ threshold}$$
 (8)

(9) distance from polygon-containing-node to nearest polygon

$$n_{distance\ of\ node\ poly\ to\ nearest\ poly}(t) = d_{POLY5}(t+1) < d_{poly\ proximity\ threshold}$$
 (9)

(10) bearing of node to nearest node on nearest polygon

$$n_{VEL3} = 180 - abs(abs(n_{VEL1} - n_{VEL2}) - 180)$$
 (10)

(11) node convergence test

$$n_{bearing \ to \ nearest \ poly}(t) = \begin{cases} \frac{1 \ if \ \sum_{t=0}^{t+10} \sum_{n \in N} \left(n_{VEL3}(t) < \theta_{bearing \ sensitivity} \right) > 0}{0 \ if \ \sum_{t=0}^{t+10} \sum_{n \in N} \left(n_{VEL3}(t) < \theta_{bearing \ sensitivity} \right) = 0} \end{cases}$$
(11)

(12) is node in a continental collision environment?

$$n_{cc\;env}(t) = n_{bearing\;to\;nearest\;poly}(t) \times n_{distance\;of\;node\;poly\;to\;nearest\;poly}(t) \times n_{area\;of\;nearest\;poly}(t) \times n_{\Delta dist\;to\;nearest\;poly}(t) \times n_{poly\;area}(t) \times n_{previous\;arc}(t)$$
 (12)

(13) is node in a rift environment

$$n_{rift\ env}(t) = \left(\left(d_{POLY4}(t) - d_{POLY4}(t-1) \right) & \left(d_{POLY4}(t-1) < d_{\max rift\ distance} \right) \right)$$
(13)

(14) is node in lip environment

$$n_{LIP\ environment}(t) = n(t) \in LIP_{polygon}$$
 (14)

(15) starting condition

$$n_{topo}(t) = \begin{cases} 2000, & if \ n(t) \in Grenville_{polygon} \\ 750, & if \ n(t) \in n_{arc}(t) \\ 150, otherwise \end{cases}$$
(15)

(16) update current topography from past topography $n_{ctopo} = n_{topo}(t+1) \tag{16}$

(17) is a node within our temporal threshold of a continental collision environment

$$n_{cctopo}(t) = \begin{cases} 0, if \sum_{t}^{t+40} n_{cc\,env} = 0\\ 1, Otherwise \end{cases}$$
 (17)

(18) is a node within our temporal threshold of a rifting environment

$$n_{rift\ topo}(t) = \begin{cases} 0, if \sum_{t}^{t-40} n_{rift\ env} = 0\\ 1, 0 therwise \end{cases}$$
 (18)

(19) update topography

$$n_{ctopo} = n_{ctopo} + \left(topo_{\min grow} + \frac{topo_k}{e^{node_{ctopo} \times topo_{\lambda}}}\right)$$
 (19)

(20) change in rift topography

$$n_{\Delta rift\ topo}(t) = \frac{n_{ctopo} - min_{rift\ topo}}{node_{time\ until\ rift\ flag}} \tag{20}$$

(21) update topography with change in rift topo

$$n_{ctopo} = n_{ctopo} - n_{\Delta rift\ topo}(t) \tag{21}$$

(22)

$$n_{local\ relief} = \left| n_{ctopo} - n_{median\ topo} \right| \tag{22}$$

(23) Erosion calculation

$$n_{erosion} = \varepsilon_{min} + \varepsilon_k \times \arctan\left(\left(\varepsilon_{offset} - n_{local\ relief}\right) \times \varepsilon_{\lambda}\right)$$
 (23)

(24) Update current topography with erosion

$$n_{ctopo} = n_{ctopo} - n_{\varepsilon} \tag{24}$$

(25) Update topography at time slice

$$n_{tono}(t) = n_{ctono} (25)$$